High-pressure X-ray photoelectron spectroscopy applied to vanadium phosphorus oxide catalysts under reaction conditions

von Master of Science in Physics

Evgueni Kleimenov

aus St. Petersburg (Russland)

Fakultät II - Mathematik und Naturwissenschaften

der Technischen Universität Berlin

zur Erlangung des akademischen Grades

Doktor der Naturwissenschaften

(Dr. rer. nat.)

genehmigte Dissertation

Promotionsausschuss:

Vorsitzender: Prof. Dr. rer. nat. T. Möller

Berichter: Prof. Dr. rer. nat. M. Dähne

Prof. Dr. rer. nat. R. Schlögl

Tag der wissenschaftlichen Aussprache: 13.05.2005

Berlin 2005

D 83

Evgueni Kleimenov
kleimen@fhi-berlin.mpg.de

Fritz-Haber-Institut der Max-Planck-Gesellschaft
Department of Inorganic Chemistry
(Prof. Dr. R. Schlögl)
Faradayweg 4-6
D-14195 Berlin, Germany

Abstract

This thesis is devoted to improvement of the high-pressure X-ray photoelectron spectroscopy (XPS) technique and to investigation by means of this technique of the industrially important vanadium phosphorus oxide (VPO) catalyst for oxidation of *n*-butane to maleic anhydride (MA).

The design of a new instrument for high-pressure XPS is presented. Introduction into the design of a differential pumping system, combined with electrostatic lenses for collection of photoelectrons, makes possible the recording of XPS spectra of a gas or solid sample in a gas atmosphere at a pressure in the sample cell of up to 5 mbar. Calculation of the dimensions of the differential pumping system was performed using the molecular and viscous gas flow models. The electrostatic lenses were designed by numerical modeling. Details of the calculations are reported.

High-pressure XPS on VPO catalysts was performed under reaction conditions with simultaneous monitoring of the catalytic activity by mass-spectrometry (i.e. *in situ*). Two differently prepared VPO samples were investigated in the reaction gas mixture at a pressure of 2 mbar at various temperatures. Both samples produced MA at the reaction temperature (400°C) and had during the experiment a similar catalytic activity towards MA normalized to the surface area. XPS spectra with the photon energies corresponding to the information depths of 1.0 and 1.8 nm were recorded. One sample showed no changes in the vanadium oxidation state with conditions and had a homogeneous distribution of oxidation state with depth. Another sample showed dramatic changes in the oxidation state. This sample was inhomogeneous both at low temperature and at 400°C. The oxidation state of the surface was determined to be of the same value (4.0±0.1) for both samples at the reaction temperature (400°C). The thickness of the topmost layer, in which changes in the oxidation state for the inhomogeneous sample occurred, was determined to be (3.5 ± 2.0) nm. Similar catalytic properties of the samples together with the same oxidation state of the surface lead one to the conclusion that this value is the upper estimation of the thickness of the catalytically active layer and the structure of the catalytically active layer does not necessarily match the structure of the bulk.

Additionally, experiments in *n*-butane/He gas mixture at the pressure of 1.6 mbar and a temperature of 400°C were performed. The homogeneous sample showed slower changes in the vanadium oxidation state of the surface during stay in the gas mixture compared with the inhomogeneous sample. This correlates with a slower drop in MA yield for the homogeneous sample.

A P/V atomic ratio for the homogeneous sample was determined using some reference compounds. The ratio had not changed during the experiments greater than the experimental error.

The results prove *in situ* XPS to be a suitable and useful technique for investigation of a real catalyst.

Kurzzusammenfassung

Diese Arbeit hat die Verbesserung der Hochdruck-Röntgen-Photoelektronen Spektroskopie (Hochdruck-XPS) und ihre Anwendung zur Untersuchung des industriell wichtigen Vanadium Phosphor Oxid (VPO) -Katalysators zur Oxidation von n-Butan zu Maleinsäureanhydrid (MA) zum Inhalt.

Die Konzeption eines neues Instruments für die Hochdruck-XPS wird vorgestellt. Der Einsatz eines differentiellen Pumpsystems kombiniert mit elektrostatischen Linsen zur Fokussierung von Photoelektronen ermöglichte die Aufnahme von XP-Spektren von gasförmigen oder festen Proben in einer Gasatmosphäre mit einem Druck von bis zu 5 mbar in der Probenzelle. Die Auslegung des differentiellen Pumpsystems basierte auf Berechnungen die für moleluare und für viskose Gasströmungen durchgeführt wurden. Die elektrostatischen Linsen wurden mit Hilfe von numerischen Modellen dimensioniert. Details der Berechnungen werden vorgestellt.

Hochdruck-XPS Messungen wurden an VPO-Katalysatoren unter Reaktionsbedingungen, bei gleichzeitiger Messung der katalytischen Aktivität mittels Massenspektrometrie (d.h. *in situ*) durchgeführt. Zwei unterschiedlich hergestellte VPO-Proben wurden in einer Reaktionsgasmischung bei einem Druck von 2 mbar und verschiedenen Temperaturen untersucht. Beide Proben produzierten MA bei einer Reaktionstemperatur von 400°C und hatten während des Experimentes eine vergleichbare katalytische Aktivität normalisiert auf die Oberfläche. XP-Spektren, mit den Photonen-Energien entsprechend einer Eindringtiefe von 1.0 und 1.8 nm, wurden gemessen. Eine Probe zeigte keine Veränderungen in der Oxidationsstufe des Vanadiums als Funktion der Reaktionbedingungen und die Oxidationsstufe war homogen mit Tiefe. Die andere Probe zeigte ausgeprägte Veränderungen der Oxidationsstufe. Diese Probe war inhomogen sowohl bei niedriger Temperatur als auch bei einer Temperatur von 400°C. Die Oxidationsstufe des Vanadiums auf der Oberfläche war bei der Reaktionstemperatur von 400°C für beide Proben die gleiche (4.0 ± 0.1). Die Dicke der obersten Schicht, in welcher Veränderungen der Oxidationsstufe bei der inhomogenen Probe auftraten wurde mit (3.5 ± 2.0) nm bestimmt. Ähnliche katalytische Eigenschaften der Proben zusammen mit der gleichen Oxidationsstufe der Oberfläche führten zu der Schlussfolgerung, dass dieser Wert die obere Grenze für eine Abschätzung der Dicke der katalytisch aktiven Schicht darstellt und dass die Struktur der katalytisch aktiven Schicht nicht notwendigerweise der Struktur der Bulk entspricht.

Zusätzlich wurden Experimente unter reduzierenden Bedingungen in einer n-Butan/He-Gasmischung bei einem Druck von 1.6 mbar und einer Temperatur von 400°C durchgeführt. In der Gasmischung zeigte die homogene Probe langsamere Veränderungen der Vanadiumoxidationsstufe in der Oberfläche, verglichen mit der inhomogenen Probe. Diese korreliert mit einem langsameren Verlust der Maleinsäureanhydrid-Ausbeute für die homogene Probe.

Das P/V-Atomverhältnis wurde für die homogene Probe mittels Referenzverbindungen bestimmt. Das Verhältnis veränderte sich während des Experimentes nur innerhalb des experimentellen Fehlers.

Die Ergebnisse zeigen, dass *in situ* XPS eine geeignete und nützliche Methode für die Untersuchung von realen Katalysatoren ist.

Евгений Юрьевич Клейменов, "Рентгеновская фотоэлектронная спектроскопия высокого давления примененная к ванадиево фосфорно оксидным катализаторам в условиях реакции", диссертация на соискание степени кандидата физико-математических наук

Автореферат

Диссертация посвящена усовершенствованию метода рентгеновской фотоэлектронной спектроскопии (РЭС) и исследованию этим методом промышленно-важного ванадиево фосфорно оксидного (VPO) катализатора для окисления *н*-бутана до малеинового ангидрида (МА).

Описана конструкция нового спектрометра для РЭС высокого давления. Включение в конструкцию спектрометра системы дифференциальной откачки, объединенной с электростатическими линзами для сбора фотоэлектронов, позволило получать фотоэлектронные спектры газа либо твердого тела в газе при давлениях в камере образца до 5 мбар. Вычисления размеров системы дифференциальной откачки производились с использованием моделей молекулярного и вязкого газовых потоков. Электростатические линзы были рассчитаны численно. Приведены детали рассчетов.

Катализаторы VPO были исследованы методом РЭС высокого давления в условиях реакции с одновременной регистрацией каталитической активности посредством масс-спектрометрии (т.е. *in situ*). Два различно приготовленных образца катализатора VPO были исследованы в газовой смеси реагентов при давлении 2 мбар при различных температурах. Оба образца производили МА при температуре реакции (400°C) и в течении эксперимента имели близкие значения каталитической активности по отношению к МА на единицу площади поверхности. Спектры РЭС были зарегистрированы с энергиями возбуждения соответствующими глубинам информации 1.0 и 1.8 нм. Для одного образца окислительное состояние ванадия оставалось постоянным при изменении условий и было однородным по глубине. Окислительное состояние ванадия для другого образца изменялось значительно. Этот образец был неоднородным и при низких температурах и при 400°C. Окислительное состояние на поверхности обоих образцов при температуре реакции (400°C) было (4.0±0.1). Толщина верхнего слоя, где окислительное состояние в неоднородном образце изменялось с глубиной, была (3.5±2.0) нм. Близкие каталитические свойства и одинаковое окислительное состояние ванадия на поверхности обоих образцов позволяют заключить, что эта величина- оценка сверху для толщины каталитически активного поверхностного слоя, и что структура этого слоя не обязательно одинакова со структурой объема.

Кроме того, были проделаны эксперименты в газовой смеси *н*-бутана и гелия при давлении 1.6 мбар и температуре 400°C. Окислительное состояние для поверхности образца, который был однороден в условиях реакции, изменялось медленнее, чем для другого образца. Этот факт коррелирует с более медленным падением выхода МА для однородного образца.

Атомное отношение P/V для однородного образца было определено с использованием эталонных материалов. Изменения этого отношения в течении экспериментов было меньше, чем погрешность измерения.

Результаты исследования доказывают пригодность и полезность *in situ* РЭС для исследования реальных (не только модельных) катализаторов.

Terms, acronyms and conventional letters

Intrinsic activity	Activity divided by surface area
Reaction mixture	(1.5% of *n*-butane in He) and O_2 / 4:1 vol., 2 mbar
Redox property	Ability of an atom to change its oxidation state
AES	Auger electron spectroscopy
BET	Brunauer-Emmett-Teller method for measuring the surface area
ESCA	Electron spectroscopy for chemical analysis
FE	Fermi edge
FWHM	Full width at half-maximum
HREM	High-resolution electron microscopy
IR	Infra-red (spectroscopy)
LEED	Low-energy electron diffraction
MA	Maleic anhydride
MS	Mass-spectrometry, mass-spectrometer
NEXAFS	Near-edge X-ray absorption fine structure (spectroscopy)
(XANES)	(X-ray absorption near-edge structure (spectroscopy))
NMR	Nuclear magnetic resonance (spectroscopy)
PTRMS	Proton-transfer-reaction MS
TEM	Transmission electron microscopy
UHV, HV	Ultra-high vacuum, high vacuum
UPS	Ultra-violet photoelectron spectroscopy
UV-VIS	Ultra-violet / visible (spectroscopy)
VB	Valence band
VPO	Vanadium phosphorus oxide(s)
WF	Work-function
XAS	X-ray absorption spectroscopy
XP, XPS	X-ray photoelectron, XP spectroscopy
XRD	X-ray diffraction
a.u.	arbitrary units
n.u.	normalized units
λ	Mean free path of electrons in gas or solid
σ	Photoionization cross-section or electron scattering cross-section
$h\nu$	Photon energy
BE, E_B	Binding energy
E_F	Fermi energy
E_p	Pass energy of the electron energy analyzer
KE, E_K	Kinetic energy
n	Concentration
p	Pressure
S	Signal or volumetric gas flow or sensitivity factor
T	Temperature

Contents

List of figures

List of tables

1 Introduction

Over the last hundred years catalysis took a firm stand in world economics. A major part of the modern chemical industry employs to a greater or lesser extent various catalytic processes, most of those are heterogeneous catalytic processes. Recently heterogeneous catalysis became also an important phenomenon for environmental protection, i.e. for catalytic neutralization of toxic emissions. It is not a secret that a major part of catalyst development and improvement follows the trial-and-error approach rather than being really knowledge-based. The striking example is the combinatorial chemistry. Numerous physical methods were developed in order to obtain knowledge about the catalytically active species and the detailed reaction mechanism of a catalytic process. Most of these methods have nevertheless, one or both of two drawbacks, those make it difficult to correlate obtained information with properties of the catalytically active material.

Firstly, many of these methods cannot be applied under reaction conditions (*in situ*). According to the general conception of catalysis [1] the function of all catalysts arises from their ability to change their geometric and electronic structures dynamically in the presence of educt and product molecules. The attempts to correlate the structure that a catalyst possesses at conditions that are not relevant to the catalytic conditions were visually compared by M. Banares [2] with trying to make a puzzle with pieces from two different boxes. Even if one will succeed to connect the pieces, the general picture will not make sense.

The *second* drawback is lack of surface sensitivity. Most of the methods are bulk sensitive, while only several atomic layers are directly participating in the catalytic process and deeper material acts as a substrate only. The structure of the topmost layers is not necessarily the same as the structure of the bulk and correlation of obtained information with properties of the active surface is problematic if possible at all.

In view of that mentioned above, development of surface sensitive *in situ* methods for catalysis can be noted as extremely important. One of the most surface sensitive methods which are widely used in catalyst investigations is X-ray photoelectron spectroscopy. Conventionally this technique operates at ultra-high vacuum conditions, but introducing in the instrument a differential pumping system can increase operation pressure of up to several mbar. Although more than 35 years have passed since the first high-pressure XPS experiments were performed, still only several papers were published about investigations by this technique of catalysts under reaction conditions.

Present work is devoted to the design of an improved high-pressure XPS instrument and application of the technique to investigation of the industrially important vanadium phosphorus oxide catalyst for oxidation of *n*-butane to maleic anhydride. This catalyst has been used in industry for more than 30 years and many publications are devoted to its investigation in order to understand the catalytic mechanism, the nature of the active species and to improve the performance of the catalyst. In spite of a great number of publications on this subject still no agreement exists about the nature of the catalytically active species. Some authors suggest crystalline $(VO)_2P_2O_7$, where V atoms are in 4+ oxidation state, as the only active phase. Others, to the contrary, state the importance of the presence of $VOPO_4$, which is V^{5+} phase or of V^{4+}/V^{5+} couples dispersed on the surface. Such a disagreement is obviously caused by lack of surface sensitivity of applied methods while many observations show that no general correlation can be drawn between the structure of the catalyst bulk and the structure of the catalytically active surface. Application under reaction conditions of XPS, which is a surface sensitive technique, makes it possible to draw conclusions about the oxidation state of vanadium atoms on the active surface.

The thesis consists of three main parts. In the first part *in situ* methods in catalysis are discussed in sense of their surface sensitivity and pressure limit in order to find out the value of *in situ* XPS among other existing methods. The second part is about *in situ* XPS. Principles and history of the technique will be reviewed. Physical basics and details of the instrument design are also presented in that part. The third part is devoted to the investigation of a VPO catalyst. An introduction about the use of a VPO catalyst in industry and about ideas existing in literature concerning the catalytically active sites will be given. XPS data will be presented and discussed from the viewpoints of understanding the nature of the catalytically active species and of the strategy for further improvement of the catalyst.

2 *In situ* methods in heterogeneous catalysis

Many physical techniques [2] were applied to investigation of a heterogeneous catalyst *in situ* (Lat. "on site"), i.e. under reaction conditions with possibility to register the reaction products[*]. Below the type of information which can be achieved from the measurements and limitations of the techniques, i.e. information depth and pressure will be reviewed briefly.

Infra-red spectroscopy is performed in the transmission, diffusion reflection or attenuated total reflection modes. The spectra give information about molecular vibrations, from which information about chemical bonding can be derived. The studies are possible at atmospheric pressure or at even higher pressures. The method can be described as not surface sensitive at all because the transition mode averages information over the whole volume and in the reflection mode the signal is registered from the layer of a thickness of about wavelength, which is several μm. The exception as for all other methods, is an investigation of adsorbates or of a thin supported layer, for which the information depth is determined by the layer thickness.

Raman spectroscopy also gives information about molecule vibrations but different selection rules make this technique complementary to infra-red spectroscopy. Raman spectroscopy can be applied under virtually any conditions. The technique is also bulk sensitive except the cases when adsorbates or a supported layer are investigated.

Sum frequency generation is another kind of vibration spectroscopy which can be operated at atmospheric pressure. This technique can be applied for investigation of only high-ordered optically flat surfaces or interfaces such as a single crystal surface. Therefore, no real catalyst can be investigated by this method. In catalysis this technique is usually applied for investigation of adsorbates and in this sense it can be referred as a surface sensitive technique.

Ultraviolet-visible spectroscopy of heterogeneous catalysts is usually performed in the diffusive reflectance mode. The technique provides information about the electronic structure of outer atomic and molecular shells, i.e. about the oxidation state and the coordination environment of atoms. An information depth value is of about wave length, which is 200-

[*] Term "*operando*" had recently appeared in the literature for such kind of techniques in order to distinguish them from the measurements in the same environment where the sample had been pretreated, but at low temperature, which sometimes also called *in situ*.

1100 nm. Therefore, the technique should be considered as bulk sensitive. The experiments are usually performed at atmospheric pressure.

Near edge X-ray absorption fine structure spectroscopy and ***extended X-ray absorption fine structure spectroscopy*** are kinds of X-ray absorption spectroscopy. NEXAFS gives information about empty electronic states of an atom and consequently, about the electronic structure. EXAFS is able to provide a detailed picture of the local geometric structure of an element studied. These techniques are suitable for investigation of amorphous as well as crystalline material. They can be applied in the transmission, electron yield or fluorescence modes. The information depth for the experiments in the transmission mode is analogous to that in transmission IR spectroscopy, i.e. the techniques are bulk sensitive except the cases of adsorbates and a supported layer. In the electron yield mode the information depth depends on the kinetic energy of electrons. The dependence can be estimated from the "universal curve" of electron inelastic mean free path in a solid [3]. For kinetic energies from 100 to 1000 eV the inelastic mean free path rises from 2 to 6 monolayers. At 3000 eV it starts to increase almost linearly from 11 monolayers and reaches 17 monolayers at 7000 eV. Thus, for the electron kinetic energies of up to 1000 eV XAS in the electron yield mode can be considered as quite surface sensitive, and for the energies starting from 3000 eV as bulk sensitive. The information depth in the fluorescent mode is equal to the X-ray attenuation length, which is usually higher than 30 nm for the photon energies used in NEXAF and EXAFS, i.e. XAS in this mode is bulk sensitive. Measurements in the transmission and fluorescence modes can be easily done at atmospheric pressure with photon energy starting from 3000 eV. In the excitation energy range of 1000-3500 eV the fluorescence and electron yield modes are usually used. XAS experiments in this range can be performed at atmospheric pressure. In the soft X-ray region (250-1000 eV) gas phase significantly absorbs photons. NEXAFS in this excitation energy region is run in the electron yield mode at pressures of up to 10 mbar.

Nuclear magnetic resonance and electron paramagnetic resonance are bulk sensitive techniques, which give information about structural and electronic properties of investigated atoms. The techniques can be applied at atmospheric pressure.

Mössbauer spectroscopy gives very precise information about the energy of a nucleus and consequently, about chemical state of the atom. Nevertheless, this technique is applicable only to a very limited number of elements which exhibit the Mössbauer effect. The technique employs a photon energy of 10-100 KeV and therefore, can be easily applied at atmospheric pressure and being a bulk sensitive technique.

Positron emission tomography is a well-established diagnostic technique in medicine, providing 3D images of a space distribution of radio isotopes such as ^{11}C, ^{13}N and ^{15}O within living human organs. In catalysis a positron emission process along with ***PET*** is also used for 1D profiling of an isotope distribution along the reactor tube (***PEP***) and for particles tracking (***PEPT***). The spatial resolution of the methods is basically limited by the positron travel distance before annihilation, which for solids is in mm range. Practically no gas pressure limit exists for these techniques because penetration ability of γ-quanta is very high.

Transmission electron microscopy was performed at pressures of up to 50 mbar [4, 5]. ***Environmental scanning electron microscopy*** is another kind of microscopy which was designed for measurements in gas atmosphere at pressure higher than 5 mbar [6]. These techniques are bulk sensitive.

Scanning tunneling microscopy was performed in a wide range of pressures (from UHV to 1 bar) and temperatures (300 to 675 K) [7]. This method gives an image of the surface with atomic resolution.

X-ray diffraction and scattering give information about the long-range crystal structure and crystallite size. The measurements can be performed at pressures of up to tenths of atmospheres. Usually these techniques operate in the transmission mode and consequently, are bulk sensitive. For optically flat surfaces a glancing incidence angle can be used, which makes the XRD technique surface sensitive. This is nevertheless, not the case for a real catalyst, which is usually powder or solid with rough surface.

From the above mentioned methods only NEXAFS in the soft X-ray energy region can be referred to as a technique which is surface sensitive enough for investigation of the surface layer of a real-catalyst material (not only a single crystal and a model supported catalyst) at catalytically-relevant pressure and temperature. On this account, ***X-ray photoelectron spectroscopy***, which is known to have the information depth of several nm or even less than one nm, should be named a very useful technique for obtaining information about the catalytically active surface layer.

3 *In situ* XPS (high-pressure XPS for catalytic studies)

In this chapter principles and brief history of XPS (part 3.1) and in particular of high-pressure XPS (part 3.2) will be reviewed. Part 3.3 contains a discussion of the physical basics of high-pressure XPS instrument designing including calculation of a differential pumping system (part 3.3.2) and an electrostatic lens system (part 3.3.3). Peculiarities of experimental data analysis in high-pressure XPS will be briefly reviewed in part 3.4. Part 3.5 is devoted to the experimental methods which are suitable for registration of reaction products in *in situ* XPS.

3.1 X-ray photoelectron spectroscopy

History of XPS [8] can be considered to begin in 1887 with discovery of the photoelectric effect by H. Herz [9]. Already in 1907 P.D. Innes [10] described a kinetic-energy spectrum of photoelectrons excited by radiation of an X-ray tube with platinum anode and registered by a spectrometer consisting of a magnetic analyzer and photographic detection. After development by Kai Siegbahn with colleagues of a high-resolution spectrometer, which allowed to measure accurately binding energy of photoelectron peaks [11], the goal of using XPS for electronic structure investigation had been realized. Subsequently the same group observed the chemical shift effect for binding energy of core-level electrons [12, 13], which led to development of the whole field of electron spectroscopy named ESCA (electron spectroscopy for chemical analysis) [14, 15]. The work of K. Siegbahn was awarded by Nobel prize in 1981 "for his contribution to the development of high-resolution electron spectroscopy". In 1969-70 commercial XPS instruments began to appear thanks to developing routine methods of obtaining UHV conditions. Starting from that time XPS can be considered as a widely used method for investigation of the surface of a solid sample. The possibility of estimation of chemical composition and of chemical state of elements together with a small information depth makes XPS an important method for microelectronics, metallurgy, heterogeneous catalysis, polymer technology and corrosion science [16].

The basic elements of an XPS instrument are a light source, an electron energy analyzer and an electron detector as it is drawn on Figure 3-1.

Figure 3-1 Basic elements of XPS experiment
according [**17**].

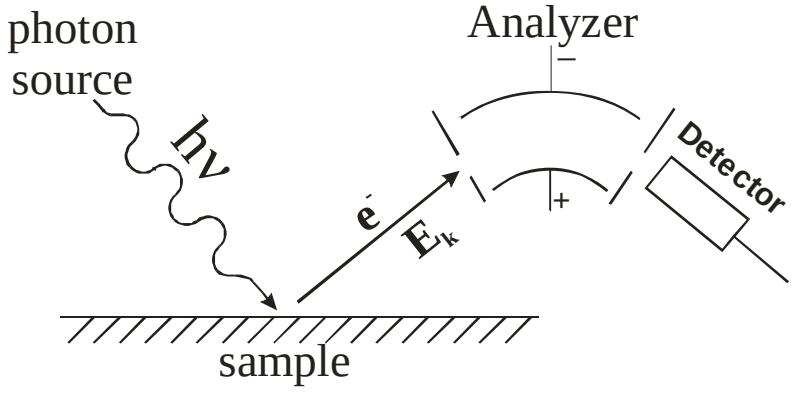

In a laboratory XPS system an X-ray tube (usually with Al or Mg cathode) and a He gas-discharge lamp are used. Spectroscopic measurements with a He lamp are usually called Ultraviolet Photoelectron Spectroscopy (UPS). Development of synchrotrons made available the whole range of excitation energies between X-ray tubes and He lamps and made a difference between XPS and UPS somewhat arbitrary. Furthermore, use of synchrotron light has several advantages comparing common laboratory X-ray sources. Besides higher photon flux and the possibility of focusing of an X-ray beam into a small spot, synchrotron light has the property of excitation energy tuneability, which allows changing the information depth and the photoelectron cross section.

Magnetic electron energy analyzers were used on early stages of XPS development. Later they were completely replaced by electrostatic analyzers because of easier construction and handling. From different types of electrostatic analyzers including the retarding field analyzer, the cylindrical mirror or deflection analyzers and the hemispherical analyzer only the last one is widely used nowadays for XPS because of better resolution characteristics. Retarding-field analyzers are employed in LEED and cylindrical-mirror analyzers are usually the part of a laboratory AES system, where the signal-to-noise ratio is more important than the resolution. A schematic diagram of a hemispherical electrostatic electron energies analyzer is shown on Figure 3-2.

Figure 3-2 Hemispherical electron energy analyzer.

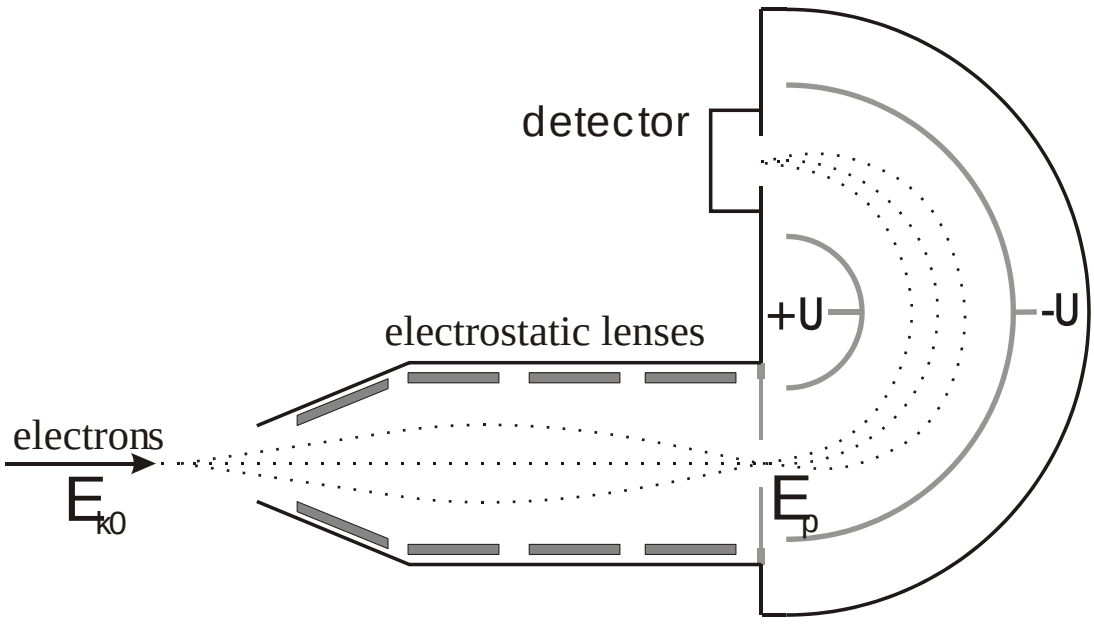

Electrons of the initial kinetic energy E_{k0}, which are supposed to be registered, are decelerating or accelerating by the electrostatic lenses to the analyzer pass energy E_p and focusing on the inlet slit. The difference in voltages on the hemispherical electrodes corresponds to a selection of electrons of the kinetic energy E_p. Thus, the photoelectrons are registered in a small kinetic energy range, those width determines the analyzer resolution. A spectrum is obtained by sweeping voltages of the electrostatic lenses and the hemispherical electrodes. Electrons are usually detected by an electron multiplier of the channeltron type and electronics in the pulse counting mode. Sometimes channeltrons are replaced by a microchannel plate or a video camera of CCD type with a fluorescent screen or other detectors for space-resolved spectroscopic measurements.

The volume of the analyzer should be kept at high vacuum conditions because the photoelectron signal would be significantly decreased by scattering of photoelectrons in the gas phase if the vacuum is not high enough. For example, the mean free path of photoelectrons of kinetic energy 100 eV in gas phase at the pressure of 1 mbar is about 1 mm. To have the mean free path bigger than the distance that electrons should travel in the spectrometer, which is usually about 1 meter or more, a vacuum better than 10^{-3} mbar is required. A sample in ordinary XPS should be also kept in high vacuum because the surface should be kept clean. Gas molecules with a sticking coefficient of unity will form a monolayer on the surface in about one second at the background pressure of 10^{-6} mbar. Therefore, the pressure in the 10^{-10} mbar range is required to keep the surface clean for a reasonable time.

Physical principles of photoemission process are demonstrated by Figure 3-3.

Figure 3-3. Schematic diagram of a core-level-photoelectron emission process.

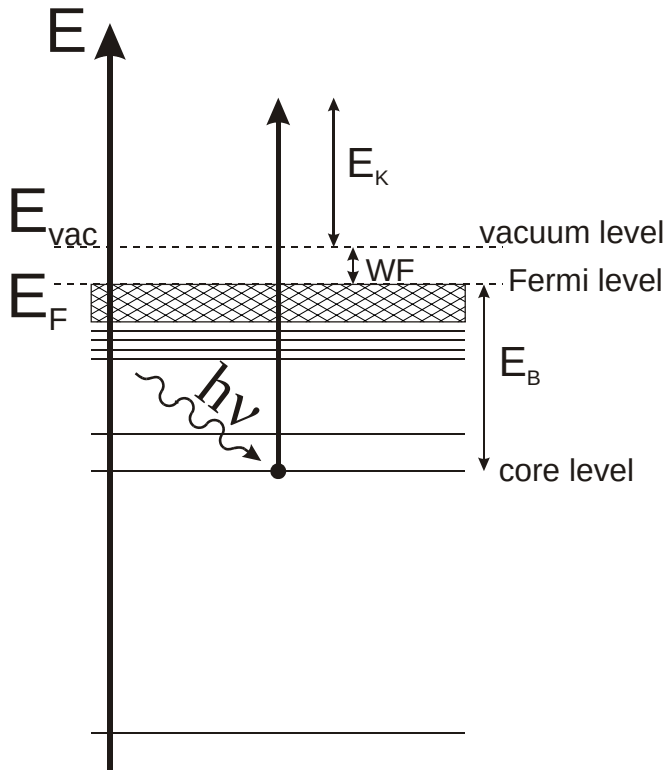

If no surface charging is present, the kinetic energy E_K of a photoelectron can be obtained from the Einstein equation:

$$E_K = hv - E_B - WF \qquad (3\text{-}1)$$

where *hv* is the energy of the X-ray quantum, E_B is the binding energy of the core level and WF is the work function of the sample. In the case of charging the potential energy of the electron in electromagnetic field should be subtracted from the right side of the equation. One should note that presented in the formula E_B is a difference of the initial and final atomic energies, which in general includes the relaxation component and which is always lower than the energy of the orbital from which the photoelectron was emitted. Nevertheless, the value E_B is suitable for element analysis and chemical state identification.

As far as every chemical element has a characteristic XPS spectrum, the chemical composition of a sample can be identified. A binding energy of a core-level electron depends also on surroundings of atoms. Non-equivalence of binding energies for an element in different chemical compounds can arise from various reasons: difference in a formal oxidation state, different molecular environment, different lattice parameters and so on. Binding energy shift due to environment effects, which is usually named chemical shift, can be described by the simple equation [18]

$$E_B - E_B(0) = IA + EA \qquad (3\text{-}2)$$

where $E_B(0)$ is the binding energy of the core-level electron in the isolated atom. The intraatomic part ***IA*** can be described in terms of the effective charge ***q*** of the atom in a molecule or crystal as IA=kq, where ***k*** is a constant for the chemical element. The extraatomic part ***EA*** is the potential energy produced by the surroundings. This part is often referred as Madelung potential. The parts IA and EA acting opposite each other and dependence of EA on type of solid sometimes makes problematic the identification of the chemical state of an atom by its chemical shift.

After escape from an atom, a photoelectron travels some distance inside the solid before escape to vacuum or relax. On the way it collides elastically or inelastically with lattice atoms. Elastic collisions do not change electron kinetic energy while inelastic lead to a decrease in energy. Inelastically scattered electrons will form a spectrum background or will not escape from solid and thus, these electrons can be counted as lost for XPS analysis. Assuming a constant from depth probability of an inelastic scattering event per length unit, the probability for photoelectrons to escape from the depth L without loss of energy can be written as Const*exp(-L/λ), where the parameter λ is usually named inelastic mean free path and represents the first momentum of a probability distribution. Dependence of this parameter on electron kinetic energy was determined experimentally for a number of elements (Figure 3-4).

Figure 3-4. Mean free path of photoelectrons in solid
according [3].

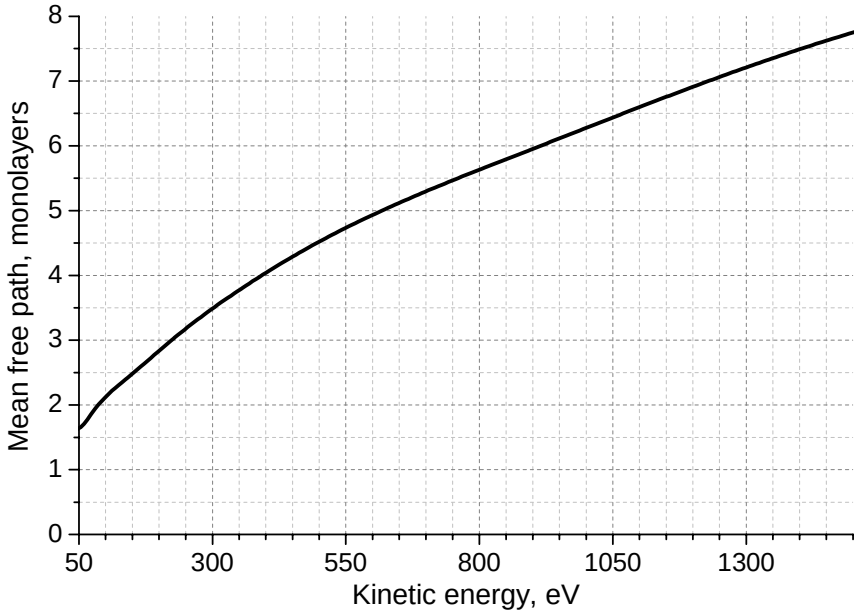

This dependence makes it possible to perform a non-destructive information depth profiling by changing kinetic energy of photoelectrons by tuning excitation photon energy, which is possible at the synchrotron. Another possibility to obtain dependence of information on depth is the angular resolved photoelectron spectroscopy (ARPES). The basics of this method are tuning of the angle φ between the perpendicular to the sample surface and the direction of photoelectron detection. Information depth depends on the angle φ as cos(φ). No excitation energy turning is necessary for this method and therefore, it can be performed with ordinary X-ray tube. Disadvantages of the method are firstly, dependence of the data quality on surface roughness, which makes it hardly applicable for powders and secondly, presence of angular-dependent effects for valence band of ordered surfaces (mainly of single crystals), which often makes impossible depth profiling on valence band by this method. Depth profiling by ARPES is mainly applied for measurement of a thickness of deposed thin films.

One should keep in mind that the information depth λ in these two depth-profiling techniques represents the electron mean free path in solid, but not the sole depth from which information is obtained. Photoelectrons are registered from the whole range of depth $z \in (0,\infty)$ with the variable probability $(1/\lambda)\cdot e^{-z/\lambda}$. For example the registered depth profile of a relative concentration C(λ) of some element referred to another element with a homogeneous concentration distribution will be the convolution of the concentration function c(z) with the probability $(1/\lambda)\cdot e^{-z/\lambda}$:

$$C(\lambda) = \frac{1}{\lambda} \cdot \int_0^\infty c(z) \cdot e^{-z/\lambda} dz \qquad (3\text{-}3)$$

Some examples of such a convolution are shown on Figure 3-5.

Figure 3-5. Convolution of some concentration depth-distributions with the probability function of photoelectron escape.

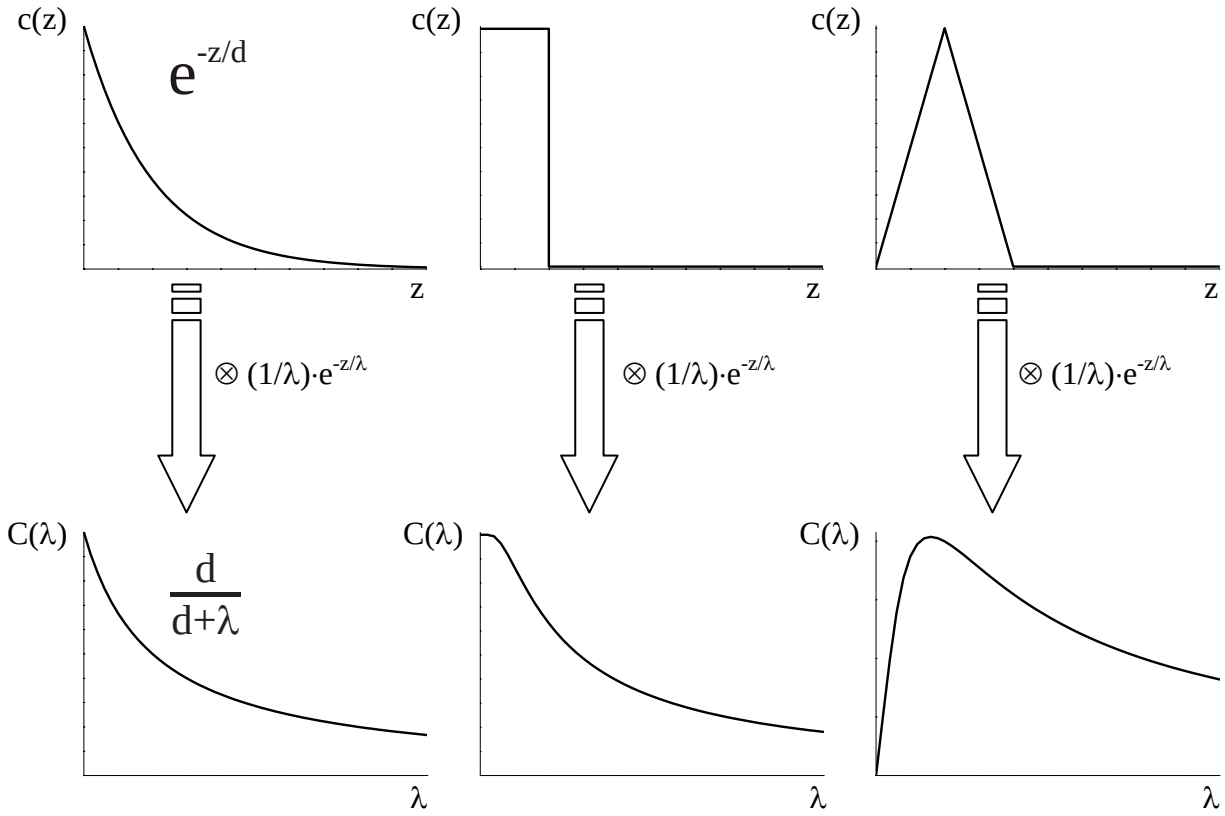

Sputtering is another depth profiling technique, which however, is destructive. This method allows variation of an information depth in a wide range. Nerveless, sputtering is known to change the surface stoichiometry and structure[*] and should be treated with caution. Additionally, it can not be applied for high-pressure XPS experiments because the technique is not suitable for pressures in mbar range.

The typical structure of an XPS spectrum is shown on Figure 3-6. The spectrum consists of relatively narrow core-level photoelectron peaks, broad Auger transition peaks and a valence band structure. The spectrum background is formed by inelastically scattered electrons. In the case of non-monochromatic radiation of a laboratory X-ray source (X-ray tube) the spectra would be complicated by peak satellites and ghosts.

[*] So-called preferential sputtering effect.

Figure 3-6. Photoelectron spectrum of V_2O_5. *hν*=730 eV.

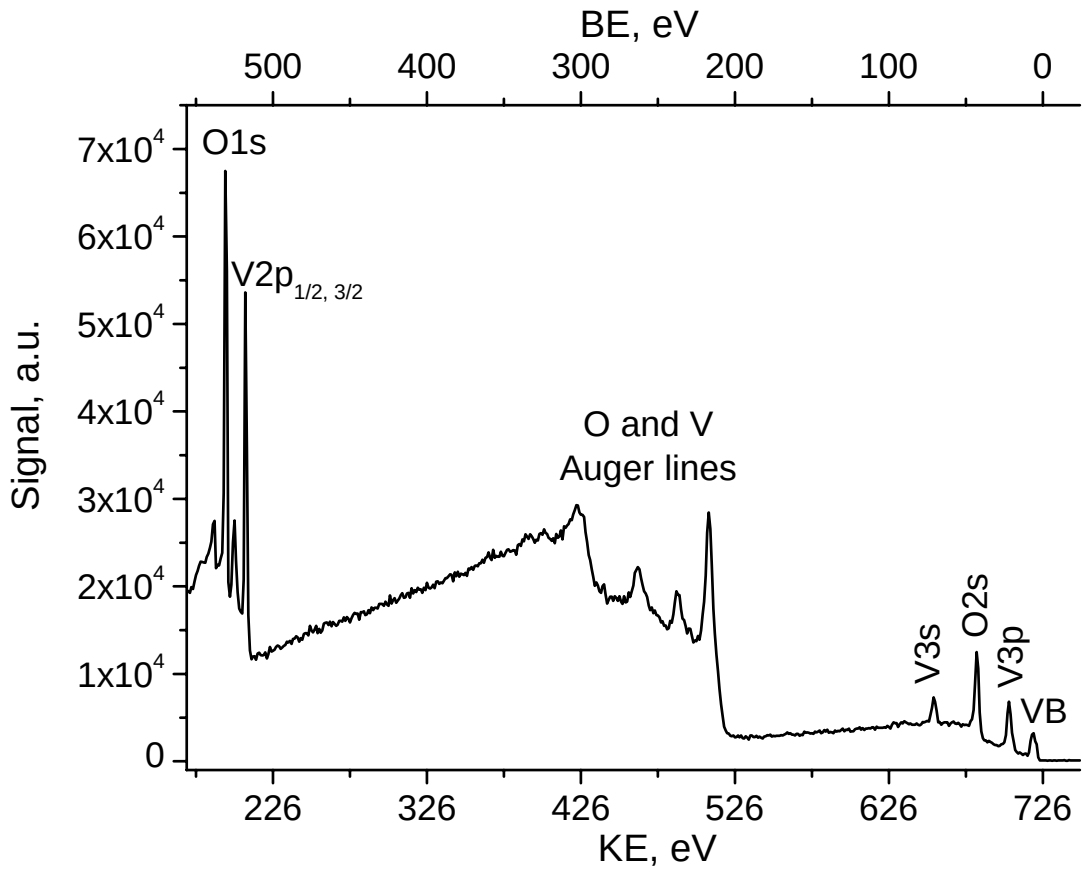

Transformation of photoelectron kinetic energy into binding energy by the Einstein equation ((3-1), page 10) implies knowledge of the analyzer work function. Moreover, if no special charge compensation techniques were applied, a charging potential for an insulator or semiconductor sample should be taken into account. As far as this knowledge is not every time available, binding energy references are used. For metallic compounds the Fermi edge is a suitable binding energy reference. A submonolayer gold film is often deposited on a sample in order to use the Au4f peak as a binding energy reference. C1s is also often employed for binding energy calibration. Other suitable reference peaks can be used as well.

The width ΔE of an XPS peak is defined as a full width at half-maximum (FWHM) of the peak after background subtraction. The width is a combination of several contributions:

$$\Delta E=(\Delta E(n)^2+\Delta E(p)^2+\Delta E(a)^2)^{1/2} \qquad (3\text{-}4)$$

where ΔE(n) is the natural width of a core level, ΔE(p) is the spectral width of photon source radiation, ΔE(a) is the analyzer resolution. Additionally, the peak can be broadened by sample inhomogeneity or by differential charging. The natural broadening and the analyzer

broadening are described by the Lorenz and Gauss profiles respectively. Synchrotron X-ray radiation has the Gauss spectral shape because of the instrumental broadening introduced by a monochromator.

The shape of a core-level photoelectron peak depends on a peak type as well as on the insulator or metallic nature of the sample. In addition, several overlapping components can be present in the peak due to the coexistence of different chemical states of the same element. The shape of a peak corresponding to a single chemical component should be determined separately for every chemical compound. Practically in most cases (except high-resolution measurements) the peak shape can be well-described by the Gauss-Lorentz (Voight) profile for semiconductors and insulators and by the Doniach-Sunjic profile for metals.

An X-ray photoelectron spectrum of a solid-state sample always contains a background, which is formed by inelasticaly scattered photoelectrons. To estimate the peak shape and the stoichiometry from an experimental spectrum first the background should be subtracted. Different models of background shape are in use. A simple linear-type background can be used for fast spectra analysis, while for more accurate line shape and stoichiometry analysis more complicated background types should be used. D.A. Shirley suggested the background shape on the assumptions of a constant energy spectrum of scattered photoelectrons and a constant scattering probability in the peak region [19]. The shape has been shown to have a significant error in the case of a metallic sample [20], but otherwise, it gives realistic results. Relative ease in use makes this background type widely used. In the case of metals, a Tougaard-type background [21] gives better results.

The stoichiometry of the sample surface can be estimated from the area ratio of XPS peaks. The general formula for the XPS peak area [22] is

$$I = nf\sigma\theta y\lambda AT \qquad (3\text{-}5)$$

where n is the atomic concentration of the element, f is the X-ray flux, σ is the photoelectronic cross-section for the atomic orbital of interest, θ is the angular efficiency factor for the instrumental arrangement, y is the efficiency in the photoelectronic process for formation of photoelectrons of the normal photoelectron energy, λ is the mean free path of the photoelectrons in the sample, A is the area of the sample from which photoelectrons are detected, T is the detection efficiency for electrons emitted from the sample.

In the case of a laboratory X-ray tube the stoichiometric ratio of two elements A and B could be determined from the peak areas:

$$\frac{n_A}{n_B} = \frac{I_A/\sigma_A y_A \lambda_A T_A}{I_B/\sigma_B y_B \lambda_B T_B} = \frac{I_A/S_A}{I_B/S_B} \qquad (3\text{-}6)$$

where S_A and S_B are the sensitivity factors for the elements, which are tabulated and listed in literature (for example [22]).

Figure 3-7. Example of use different *hv* to achieve the same KE of different peaks.

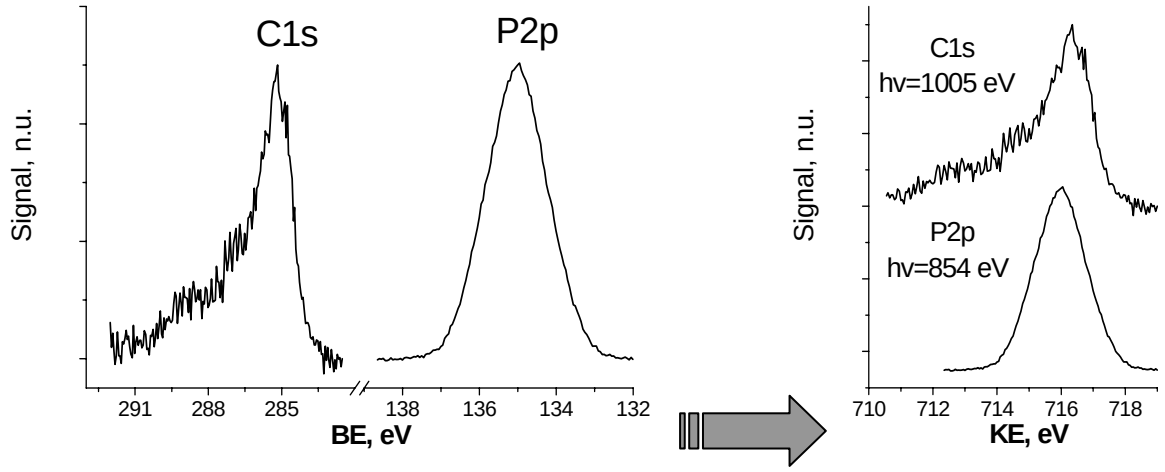

If the X-ray source is a synchrotron, it is possible to set kinetic energies of photoelectrons from certain core levels of two different elements to the same value by use of two different excitation energies (Figure 3-7). The same information depth and the same analyzer transmission are achieved in this case and the formula for the stoichiometric ratio has the form:

$$\frac{n_A}{n_B} = \frac{I_A}{I_B}\frac{f_B}{f_A}\frac{\sigma_B}{\sigma_A} \qquad (3\text{-}7)$$

The cross-sections were calculated theoretically in [23]. An analytical formula for the photon-energy dependence was obtained on base of this data in [24]. It should be noted that some disagreements were found for selected compounds between theoretical cross-section values and experimental data [25]. As far as no other extended theoretical or experimental cross-section database is available, stoichiometric ratio estimations are desired to be proven by measurement of reference compounds.

3.2 Principles and history of high-pressure XPS

The base elements of a high-pressure XPS setup are shown on Figure 3-8.

Figure 3-8 Principle scheme of a high-pressure XPS experiment.

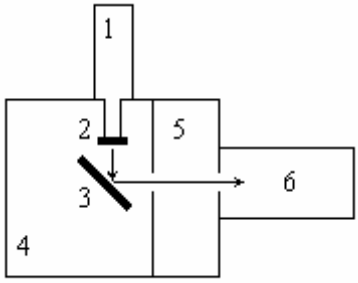

1. X-ray source
2. X-ray window
3. sample
4. experimental cell
5. differential pumping stage(s)
6. electron energy analyzer

The X-ray source ***(1)*** can be a conventional X-ray tube or a synchrotron. The thin X-ray window ***(2)*** separates volume of the X-ray source from the experimental cell ***(4)***. X-rays from the source pass the X-ray window, hit the sample ***(3)*** and extract photoelectrons. After traveling in the sample cell a part of photoelectrons reaches the entrance aperture of the differential pumping stage(s) ***(5)*** and passes through it to the electron energy analyzer ***(6)***. Therefore, application of the differential pumping allows minimization of a travel path of photoelectrons in gas phase. Gas atmosphere can be introduced into the sample cell instead of UHV conditions, which are obligatory for conventional XPS. The pressure of gas in the sample cell is limited by scattering of photoelectrons by gas-phase molecules, which leads to a decrease of a photoelectron signal. A maximum pressure depends on several factors like the distance between the sample and the first aperture, the intensity of the X-ray source, photoelectron collection and detection efficiencies, the kinetic energy of photoelectrons and the type of the gas. Electrostatic lenses introduced into the differential pumping stage (or stages) could increase significantly collection of photoelectrons as demonstrated by Figure 3-9.

Figure 3-9 Collection of photoelectrons without (a) and with (b) electrostatic lenses.
Electron trajectories are shown.

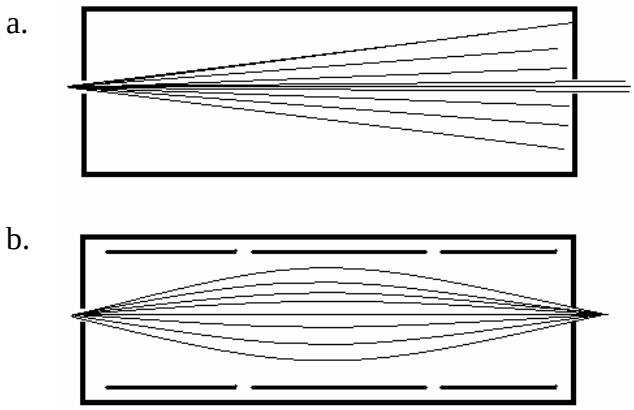

The concept of differential pumping for high-pressure XPS was first applied by K. Siegbahn with colleagues [18] in 1969 for investigation of gases at pressures of up to a few tenths of a Torr (1 Torr= 1.33 mbar= 133 Pa). The system was based on a magnetic-type electron energy analyzer with one differential pumping stage. Four years later K. Siegbahn and H. Sieghban reported the first XPS experiment on liquids [26]. The experimental system allowed investigations of a liquid beam of liquids with a vapor pressure of less than 1 Torr and was also based on a magnetic-type electron energy analyzer with one differential pumping stage. Some other modifications of the spectrometer for liquid studies were reported later by the same group [27, 28]. In 1979 the construction of the commercialized afterwards XPS system for investigations of solids in gas at pressures of up to 1 Torr was reported by R. Joyner and M. Roberts [29]. One differential pumping stage around the high-pressure sample cell was used in combination with the commercial hemispherical electron energy analyzer ESCALAB of V.G. Scientific Ltd. Next design of a high-pressure XPS system was reported by H. Ruppender et al. in 1990 [30]. The system included three differential pumping stages and allowed to perform experiments at gas pressures of up to 1 mbar. In 2000 the first results obtained on the high-pressure XPS system designed by the group of M. Salmeron were announced [31]. The spectrometer included a two-stage differential pumping combined with the first introduced electrostatic lens system for collection of photoelectrons. The system was used with a synchrotron X-ray source and allowed investigations at pressures of up to 7 mbar. This setup was applied to investigate heterogeneous catalytic systems under reaction conditions simultaneously with the monitoring of reaction products ([32], [33], [34]) and to investigate of the process of ice premelting [32, 35]. This is why the setup got the special name "*in situ* XPS". In 2001 M.A. Kelly et al. reported construction of a high-pressure X-ray

photoelectron spectrometer for monitoring of thin films synthesis [36]. A modified SURFACE-SCIENCE-INSTRUMENTS hemispherical electron energy analyzer with the specially constructed electrostatic lens system and a one-stage differential pumping made possible measurements in gas atmosphere at pressures of up to 20 mTorr (0.03 mbar). The electrostatic focusing elements introduced into the differential pumping stage of this setup allowed collection of photoelectrons from the cone with the half angle of 15° and from the surface area of about 1-2 mm^2. Such a high collection was achieved because the electrostatic lens elements were mounted very close to the sample. Nevertheless, the distance between the sample and the inlet aperture of the differential pumping was about 40-50 mm (comparing 1-2 mm in all other designs), which limits the pressure in the sample cell to quite low values.

The system described here was constructed by our group (Fritz-Haber-Institut, Department of Inorganic Chemistry, Group of Surface Analysis) in close collaboration with the group of M. Salmeron and represents the next version of the setup described above ([32]). The differential pumping and photoelectron collection systems were improved compared with the previous design. Two almost identical exemplars of the new setup were produced. The first one is for the group of M. Salmeron and another is for our group. Our high-pressure XPS system has worked since September 2002 when it was successfully tested with a copper catalyst [33] at the beamline U49/2-PGM1 of the synchrotron BESSY II (Berlin, Germany).

In March 2004 the company GAMMADATA SCIENTA announced a commercial high-pressure XPS system based on a spectrometer SES-100. Pressure drop in the four-stage differential pumping system was specified to be "better than 6 orders of magnitude", which should correspond to the pressure limit in the sample cell of about 0.1 mbar assuming a pressure in the analyser not higher than 10^{-7} mbar.

3.3 Construction of the high-pressure XPS system and characteristics of the system

3.3.1 Factors influencing performance of the system.

As it was discussed in the previous chapter, the base feature of a high-pressure XPS system (Figure 3-10) is the differential pumping between the sample cell and the electron energy analyzer. The criterion for quality of a high-pressure XPS spectrometer is the maximum pressure in the sample cell, which can be achieved without loss of spectrum quality.

Figure 3-10. High-pressure XPS setup.

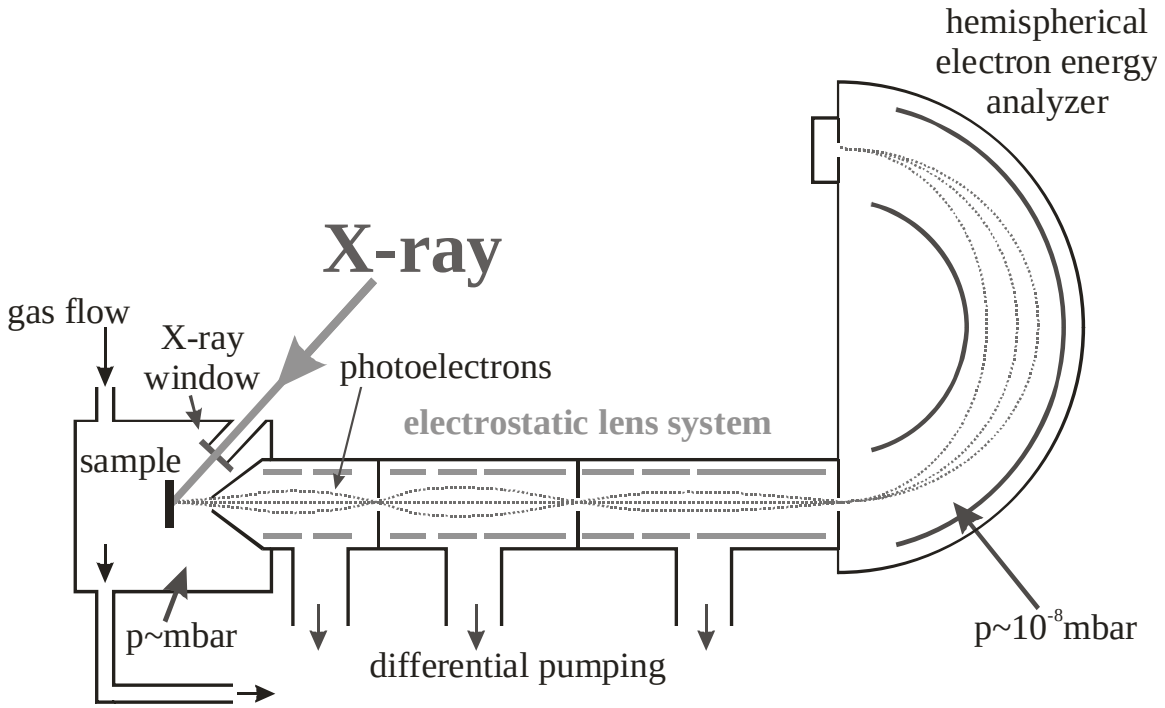

There are several parameters, which influence an XPS signal level:

1) X-ray intensity at the sample position, which depends on:
   a) flux of the X-ray source
   b) transmission of the X-ray window
   c) adsorption of X-ray by gas phase in the sample cell
2) Efficiency of photoionisation and scattering of photoelectrons in solid
3) Scattering of photoelectrons by gas phase
4) Efficiency of photoelectron collection by the spectrometer.

It should be noted that the signal value as an indicator of the spectrometer quality should be always referred to the same spectral resolution because a higher X-ray flux could always be achieved by decreasing a monochromator resolution or by better photoelectron collection caused by decrease of the electron energy analyzer resolution. Influence of these factors on the total signal will be estimated below.

The thickness and the area of X-ray window determine its mechanic stability. For example, the Si_3N_4 X-ray window of 2.5x2.5 mm^2 area and 100 nm thickness can hold the pressure difference of up to 10 mbar. The transmission of such a window and of thicker/thinner windows is plotted on Figure 3-11. From this figure it is clear that the window attenuates the total XPS signal at the most by one order of magnitude in the region of photon energies which are usually used in XPS.

Figure 3-11. Transmission of X-rays by Si_3N_4 window of different thickness
(calculated according to [37]).

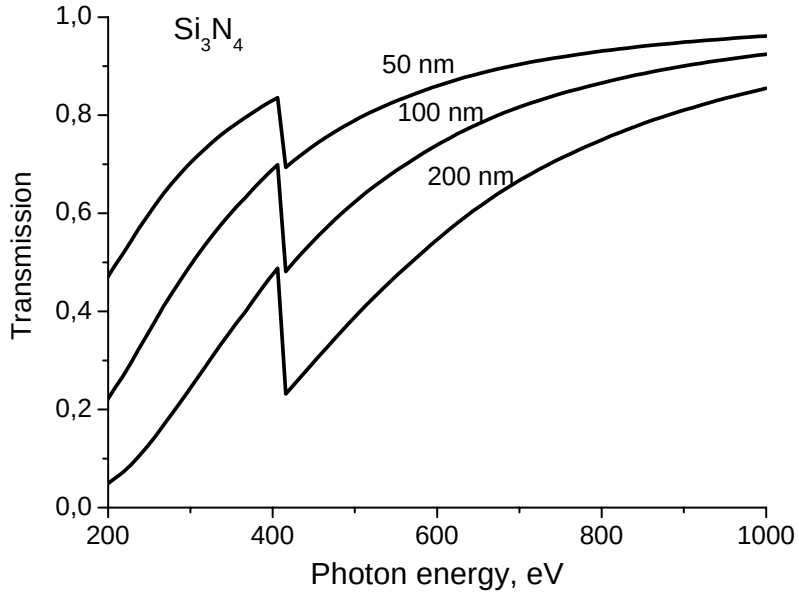

The X-ray transmission of two selected gases (oxygen and n-butane) is shown on Figure 3-12. The figure shows that absorption of X-rays by gas atmosphere on a path of a few cm will not decrease the overall signal more than by an order of magnitude.

Figure 3-12. X-ray transmission of O_2 and butane.
(calculated according [37])

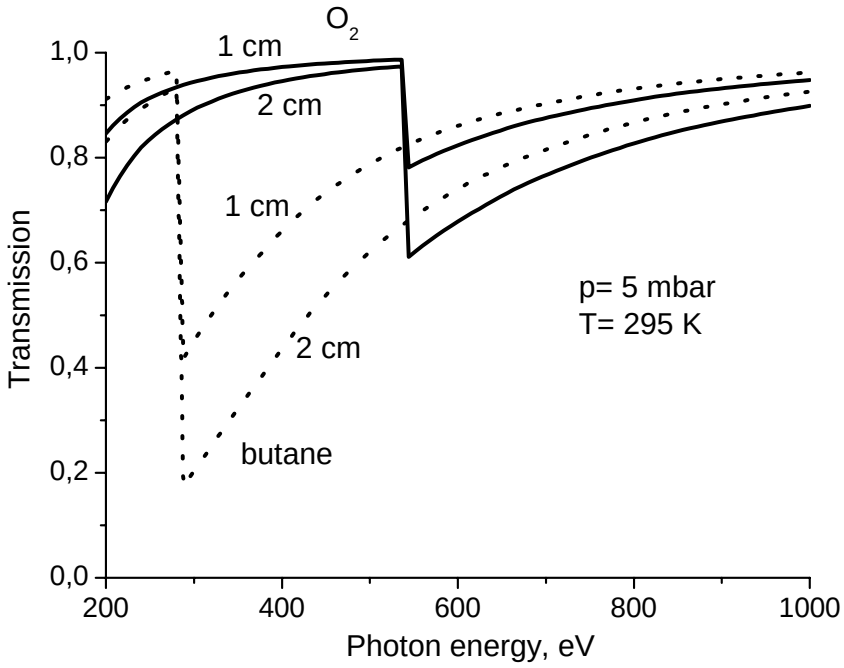

An influence of photoelectron scattering by gas phase on the overall signal depends on a pressure and on a path length of photoelectrons in gas phase. Actually, scattering of photoelectrons is the main factor limiting a maximum pressure in the sample cell. As far as a photoelectron signal decreases exponentially with the path length, a distance between the sample surface and the first aperture of differential pumping should be kept as short as possible. However, it is not possible to set the distance to be less than 1 mm for the aperture radius of 0.5 mm because a gas pressure near the sample surface depends on a distance/aperture-size ratio. The dependence was estimated in [31] using the molecular flow approach:

$$p(z) = \frac{1}{2} p_0 \left(1 - \frac{z}{\sqrt{1+z^2}} \right) \qquad (3\text{-}8)$$

Figure 3-13. Scheme for the equation (3-8)

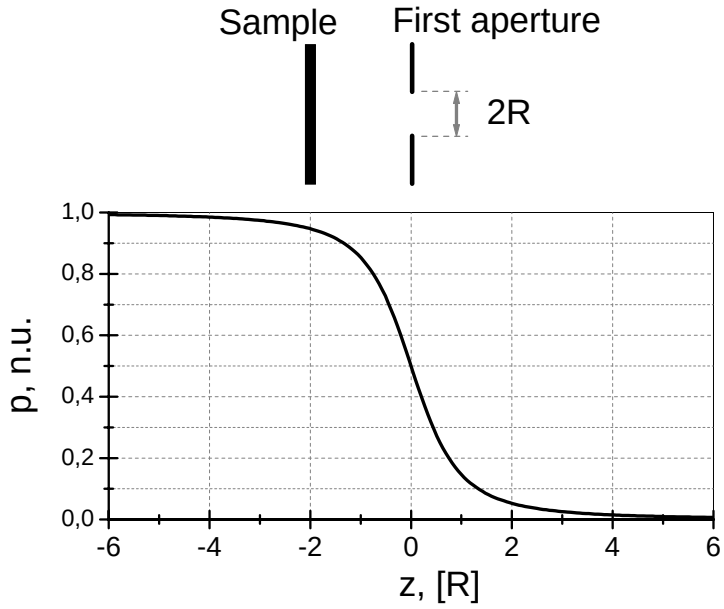

where p_0 is a pressure in the sample cell and z is measured in R units. According to this formula, the pressure near the sample surface would be 99% of p_0 for z=-4 or 95% for z=-2 or 85% for z=-1. Therefore, it is not recommended to go much closer than z=-2, which is 1 mm for the aperture diameter of 1 mm.

Cross-sections of photoelectron scattering by hydrogen molecules are shown on Figure 3-14a.

Figure 3-14. Characteristics of photoelectron scattering by molecular hydrogen

a. Cross-sections for scattering of photoelectrons by a hydrogen molecule according to [38],
b. Mean free path of photoelectrons in hydrogen at T=300 K, p=1 mbar calculated using these cross-sections.

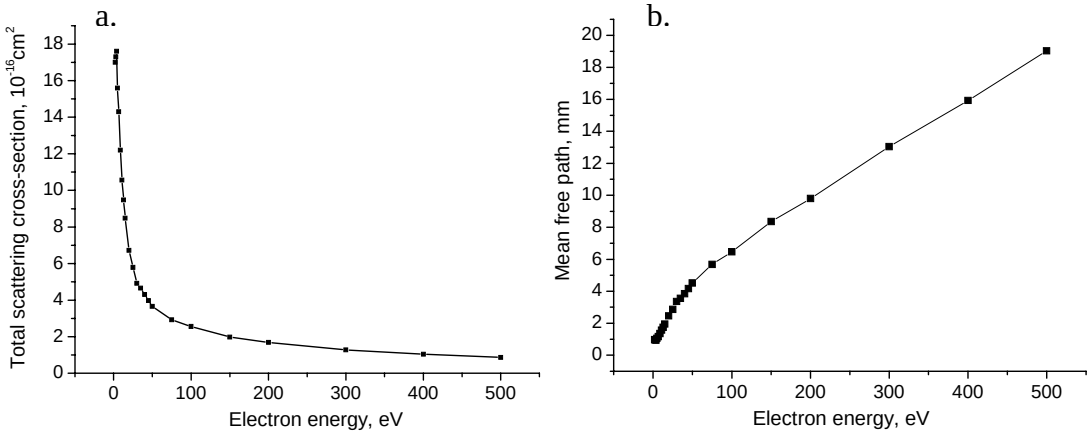

It is easy to convert these values into a mean free path of photoelectrons using the formula:

$$\lambda = \frac{4kT}{p\sigma} \qquad (3\text{-}9)$$

where ***k*** is the Boltzmann constant, $\boldsymbol{\sigma}$ is the scattering cross-section. The result for T=300 K and p=1 mbar is shown on Figure 3-14b. For low-energy electrons the mean free path at these conditions is about 1 mm. To calculate a decrease of the photoelectron signal on the whole path, the variation of the pressure along the z axis (3-1) should be taken into account. An effective path can be defined ([31]) as:

$$L = \left(\frac{R}{p_0}\right)\int p(z)dz = \frac{1}{2}R\left(\sqrt{1+z^2} - z\right) \qquad (3\text{-}10)$$

The effective path corresponds to the length which should be passed by photoelectrons in the gas at the pressure p_0 to have the same attenuation as for a variable pressure defined by the formula (3-9). For R=0.5 mm and z=-2, which correspond to the aperture diameter of 1 mm and to the distance from a sample to the aperture of 1 mm the effective path L will be 1.1 mm. The signal ***S*** for this effective path in hydrogen at p=1 mbar and T= 300 K decreases by 3 times for low-energy electrons compared to the signal in vacuum S_{vac} according the formula:

$$S = S_{vac}e^{-\lambda/L} = S_{vac}e^{\frac{4kT}{p\sigma L}} \qquad (3\text{-}11)$$

The signal decreases exponentially with pressure and effective path increase:

$$\frac{S}{S_{vac}} = \left(\frac{S(p_1, L_1)}{S_{vac}}\right)^{-\frac{p}{p_1}\frac{L}{L_1}} \qquad (3\text{-}12)$$

This means that at the same conditions in hydrogen the signal will decrease by 9 times at p=2 mbar, by 27 times at 3 mbar, by 244 times at 5 mbar and so on. It can be concluded, that a maximum pressure at these conditions should be of several mbar. Decreasing of the effective path could increase a maximum pressure, but as it was discussed above, this is possible only with simultaneous decrease of the aperture size, which will cause the requirement of higher X-ray intensity and as a consequence, beam damage of the sample and X-ray window.

It should be taken into account, that H_2 is a small molecule and for other molecules the cross-section should be bigger and consequently, the mean free path should be less and the maximum should be lower.

Efficiency of the photoelectron collection is determined by the collection solid angle Ω, which is a function of the collection plane half-angle **a**: $\Omega=4\pi\cdot\sin^2(a/2)$. This function can be well approximated by a second-order polynomial at **a**<10° (Figure 3-15).

Figure 3-15. Function $\sin^2(a/2)$ and its approximation by a second-order polynomial.

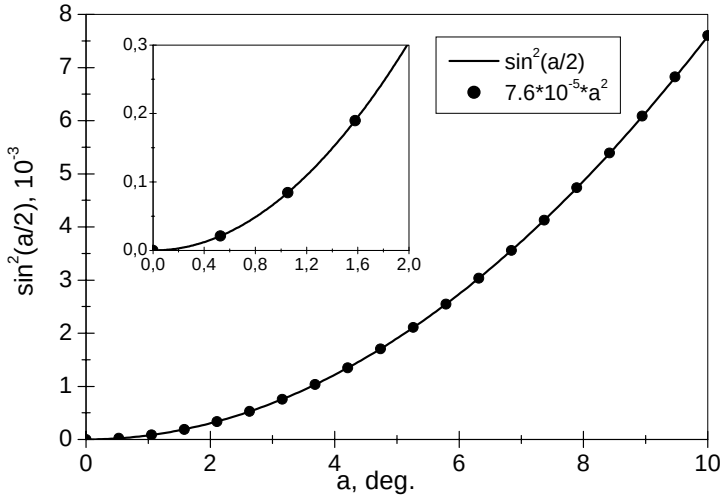

Consequently, it can be concluded that at small angles photoelectron collection efficiency depends on the collection plane half-angle squared. Therefore, it is extremely important to achieve as high a collection angle as possible to reach the best system sensitivity. In the first high-pressure XPS systems [18, 26-29, 31] photoelectron collection efficiency was quite low because no special electrostatic collection system was applied. The effect of increasing the collection angle by using an electrostatic lens system can be illustrated by Figure 3-9 on page 18. A photoelectron collection angle for a 50-cm-long differential pumping system with the radius of the exit slit of 1 mm* can be improved from 0.1° to 5° by introduction an electrostatic lens system. This improvement corresponds to the increase in a collection efficiency by $2.5\cdot10^3$ times. This example clearly demonstrates importance of use of an electrostatic collection system.

The first group who had used an electrostatic lens system in high-pressure XPS was the group of M. Salmeron from Berkley National Lab. The idea of electrostatic lenses in a differential pumping stage was implemented by attaching to a commercial analyzer from Physical Electronics of an additional part containing combined differential pumping and electrostatic lenses [31]. An acceptance half-angle of the system was reported to be 3.5°.

* The geometrical sizes were taken from the analyzer Phoibos 150 (SPECS GmbH, Berlin)

Summarizing this part it is worth noting that the main factor limiting the maximum working pressure in the sample cell is scattering of low-energy photoelectrons by gas phase molecules. A path of photoelectrons in gas phase cannot be much shorter than the size of the first aperture because it would lead to a decrease of gas pressure near to the investigated area of the sample surface. Aperture size cannot be decreased significantly below 1 mm because it influences the value of the investigated area and collection angle. The possibilities to increase a maximum pressure are to use a photon source with higher flux and tighter focus, which nevertheless, can be accompanied by beam damage of the sample, and/or to improve collection of photoelectrons by using an electrostatic lens system in differential pumping stages.

3.3.2 Calculation and design of the differential pumping system.

In this chapter details of calculations of the differential pumping system and performance of the designed system are presented. The calculations are based on the approach developed by the group of M. Salmeron for design of the prototype of the system [32].

The main parameters determining a differential pumping design are inlet gas flow and desired pressure after the last pumping stage. The inlet flow, which is the flow through the first aperture, will be estimated below. Denoting the volumetric flow rate through the first aperture as S_a and the pumping speed of the pump in the first pumping stage as S_1 we will get the expression for a pressure in the first pumping stage:

$$\frac{p_1}{p_0} = \frac{S_a}{S_1} \qquad (3\text{-}13)$$

To calculate the flow S_1 two approaches could be used.

The ***molecular flow approach*** is for the low-pressure region, where the mean free path of gas molecules λ_{gas} is greater than the aperture diameter $2R$. This approach implies the absence of molecule-molecule collisions in a space region near the aperture. According to this approach a volumetric flow rate can be determined from the formula:

$$S_a = \pi R^2 < v >= \pi R^2 \sqrt{\frac{3kN_A T}{M}} \qquad (3\text{-}14)$$

where the $<v>$ is a mean molecular velocity (which was assumed to be a mean-square velocity of ideal gas molecules), T is a gas temperature, M is a molar mass, k and N_A are the Boltzmann and Avogadro constants. As an example, the volumetric flow will be calculated for water molecules. For other gases except hydrogen and helium the volumetric flow should be less or the same. A volumetric flow of water molecules through the aperture of 1 mm diameter at room temperature is 0.5 l/s, which means a pressure drop of $0.7 \cdot 10^3$-$1.4 \cdot 10^3$ times in the first stage comparing the pressure in the sample cell if using in the first stage a high-performance Leybold Turbovac TW 700 turbo-pump with 330-680 l/s pumping speed. This means that three pumping stages are necessary to keep a pressure in analyzer in 10^{-8} mbar range simultaneously with a pressure of several mbar in the sample cell.

Even with ideal pumping the fraction $\Omega/2\pi$ of the flux will pass through the differential pumping system as a molecular beam (here $\Omega \approx \pi \cdot R_3^2/L^2$ is a solid angle of the differential pumping exit slit seen from the source aperture). This gives the expression for the minimum length L of the differential pumping system:

$$S_a p_0 \left(\pi \frac{R^2}{L^2} \right) \Big/ 2\pi \le S_3 p_3 \qquad (3\text{-}15)$$

$$\text{or } L \ge \frac{R_3}{2} \sqrt{\frac{S_a}{S_3} \frac{p_0}{p_3}} \qquad (3\text{-}16)$$

where R_3, S_3 and p_3 are the radius of the exit aperture of the third pumping stage, the volumetric flow through this aperture, and the pressure in the third stage respectively. Supposing a diameter of the third aperture is 2 mm and a pumping speed is 105-180 l/s* the minimum length will be estimated to be $L_{min}=350 \cdot R_3=70$ cm.

The second approach for the consideration of a gas flow is the ***viscous flow approach***. This approach is for high pressures for which $\lambda \le 0.01 \cdot 2R$. In this case a gas jet is described as a supersonic molecular beam [39].

In the case if the ratio $p_1/p_0 <$ ***const*** (where ***const*** is some value, which depends on the gas nature but is always greater than 0.528), which certainly takes place at $p_0=5$ mbar, the flow through the aperture becomes so-named "choked flow", which mean that a volumetric flow does not change with a pressure and is determined by the formula

$$S_a = \pi R^2 a^* \qquad (3\text{-}17)$$

where ***a**** is a sound velocity in plane of the aperture. Applying thermodynamic equations for the isentropic flow one will get:

$$S_a = \pi R^2 \sqrt{\frac{2\gamma}{1+\gamma}} \sqrt{\frac{kN_A T}{M}} \qquad (3\text{-}18)$$

where $\gamma \equiv c_p/c_v$. For all ideal gases $1<\gamma\le 1.67$, which means $1 < \sqrt{\frac{2\gamma}{1+\gamma}} \le 1.118$ or $\sqrt{\frac{2\gamma}{1+\gamma}} \approx 1$ for all gases and $S_a \approx 0.3$ l/s for water molecules at 300 K. This value is smaller than the value obtained by the molecular flow approach. Nevertheless, the supersonic flow is more directional than the molecular flow, at least before the Mach-disk-shock plane [40], which in our case is on the distance $x_M=0.67 \cdot d \cdot (p_0/p_1)^{1/2} \approx 4.7$ cm. After this plane the flow can be already accounted as a molecular flow. This means that one can first consider the flow as a non-directed molecular flow with S_a calculated using the formula (3-18) and afterwards add x_M to the obtained value. Therefore, by applying the formula (3-16) one will get the length of 55 cm and the total length L will be 60 cm, which is smaller than the value calculated by the

* Pfeiffer Vacuum TMU200MP pump

molecular-flow approach. In reality the length of the differential pumping system should be greater because of the technical reason: pumping should be performed through a tube of the same diameter as the entrance hole of a turbo-pump, which is usually of 100 mm or bigger for high-performance vacuum pumps. In the case of a smaller diameter of the tube a pumping speed of the system will be decreased. One should also consider some space for mounting pumps and vacuum valves.

As in the molecular flow approach, three differential pumping stages are necessary to keep a pressure in the analyzer in 10^{-8} mbar range.

Unfortunately, neither the molecular flow approach nor the viscous flow approach is applicable for a pressure in the sample cell of several mbar. The mean free path is determined by the formula:

$$\lambda = \frac{kT}{p\sigma_{gas}} \qquad (3\text{-}19)$$

where collision cross-section σ_{gas} can be well approximated by geometrical size of the molecule. For water molecules at room temperature and pressure of 1mbar the mean free path is $\lambda \approx 0.2$ mm, which falls into the transition region 0.01 mm$<\lambda<$1 mm between viscous and molecular flows. Nevertheless one can interpolate the data received by these two approaches taking into account that the results are not very different.

A scheme of the differential pumping system is shown on Figure 3-16.

Figure 3-16. Scheme of the differential pumping system.
See text for the abbreviations.

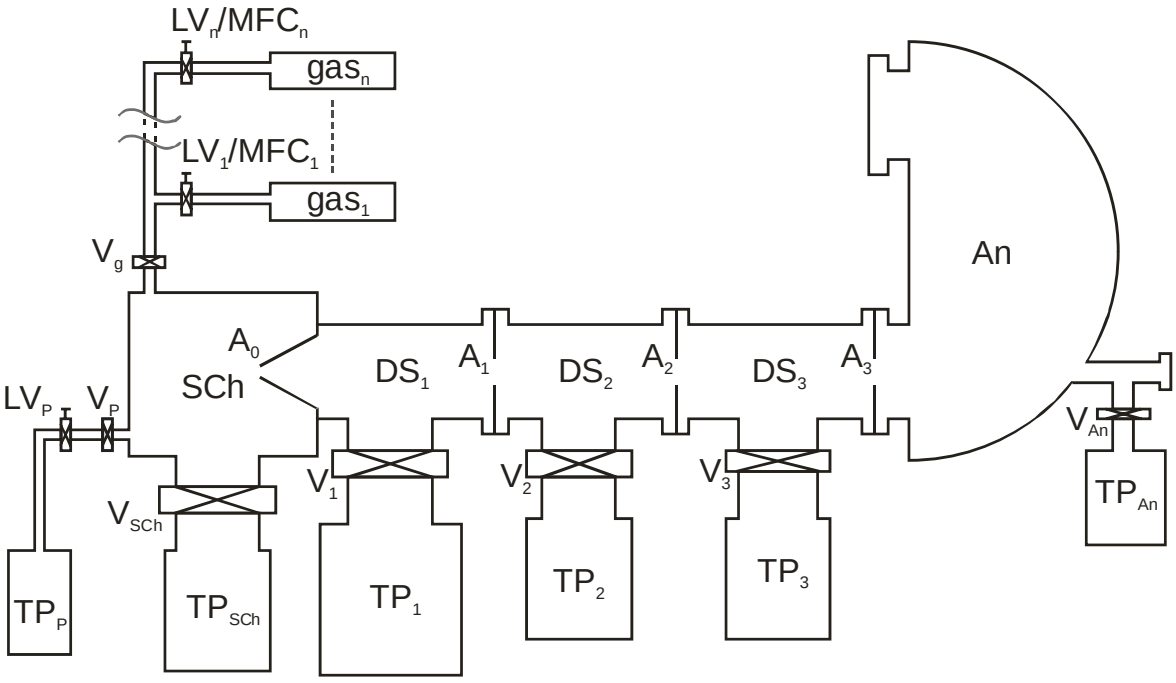

The differential pumping system between the sample chamber ***SCh*** and the analyzer ***An*** consists of three differential pumping stages $DS_{1,2,3}$ connected through the apertures A_0-A_3. The vacuum turbo-pumps TP_{Sch}, TP_{An} and $TP_{1,2,3}$ can be separated from the evacuated volume by the vacuum valves $V_{1,2,3,SCh,An}$. The separation of the pumps allows maintenance of the system at vacuum conditions during transportation and attachment to a synchrotron beamline. Moreover, separation of the pump TP_{SCh} from the sample cell allows letting into the sample cell a gas atmosphere by flowing gases through the chamber.

Characteristics of the system and results of test measurements are listed in Table 3-1 - Table 3-3.

Table 3-1. Performance of the turbo-pumps.

Part of the system	Type of a turbo-pump	Pumping speed*, l/s
DS_1	Leybold Turbovac TW 700	330-680
DS_2	Pfeiffer Vacuum TMU200MP	105-180
DS_3	Pfeiffer Vacuum TMU200MP	105-180

* A pumping speed in the pressure region below 10^{-3} mbar does not depend on a pressure, but depends on the gas nature.

Table 3-2. Aperture diameters and distances between apertures.

Apertures	Distance, mm	Aperture	Diameter, mm
A_0-A_1	260	A_0	1
A_1-A_2	240	A_1	2
A_2-A_3	334	A_2	2
A_0-A_3	834	A_3	3*

* The exit aperture of the differential pumping stage is followed by the entrance slit of the analyzer, which is of a variable size.

Table 3-3. Results of a test of the differential pumping system with air.

p(SCh), mbar	p(DS_1), mbar	p(DS_2), mbar	p(DS_3), mbar	p(An), mbar
$1.28\cdot10^{-7}$	$4.06\cdot10^{-9}$	$2.60\cdot10^{-8}$	$1.29\cdot10^{-8}$	$3.38\cdot10^{-8}$
$1.02\cdot10^{-6}$	$4.33\cdot10^{-9}$	$2.64\cdot10^{-8}$	$1.29\cdot10^{-8}$	$3.38\cdot10^{-8}$
$1.07\cdot10^{-5}$	$7.72\cdot10^{-9}$	$2.63\cdot10^{-8}$	$1.29\cdot10^{-8}$	$3.38\cdot10^{-8}$
$1.08\cdot10^{-4}$	$4.08\cdot10^{-8}$	$2.65\cdot10^{-8}$	$1.29\cdot10^{-8}$	$3.38\cdot10^{-8}$
$1.15\cdot10^{-3}$	$3.75\cdot10^{-7}$	$2.85\cdot10^{-8}$	$1.30\cdot10^{-8}$	$3.38\cdot10^{-8}$
$1.50\cdot10^{-2}$	$4.06\cdot10^{-6}$	$4.62\cdot10^{-8}$	$1.30\cdot10^{-8}$	$3.41\cdot10^{-8}$
0.11	$3.65\cdot10^{-5}$	$2.15\cdot10^{-7}$	$1.40\cdot10^{-8}$	$3.58\cdot10^{-8}$
0.22	$7.88\cdot10^{-5}$	$4.18\cdot10^{-7}$	$1.51\cdot10^{-8}$	$3.67\cdot10^{-8}$
0.50	$2.24\cdot10^{-4}$	$1.10\cdot10^{-6}$	$1.86\cdot10^{-8}$	$4.10\cdot10^{-8}$
1.04	$5.77\cdot10^{-4}$	$2.63\cdot10^{-6}$	$2.62\cdot10^{-8}$	$5.07\cdot10^{-8}$
2.01	$1.32\cdot10^{-3}$	$5.89\cdot10^{-6}$	$4.33\cdot10^{-8}$	$7.28\cdot10^{-8}$
5.03	$3.44\cdot10^{-3}$	$1.60\cdot10^{-5}$	$9.74\cdot10^{-8}$	$1.43\cdot10^{-7}$
10.2	$6.67\cdot10^{-3}$	$3.34\cdot10^{-5}$	$1.96\cdot10^{-7}$	$2.62\cdot10^{-7}$

Constant flow of the reaction gases is organized as it was briefly discussed above and was shown on Figure 3-16. A more detailed scheme is shown on Figure 3-17.

Figure 3-17. Scheme of gas flow through the reaction chamber.
See text for the abbreviations.

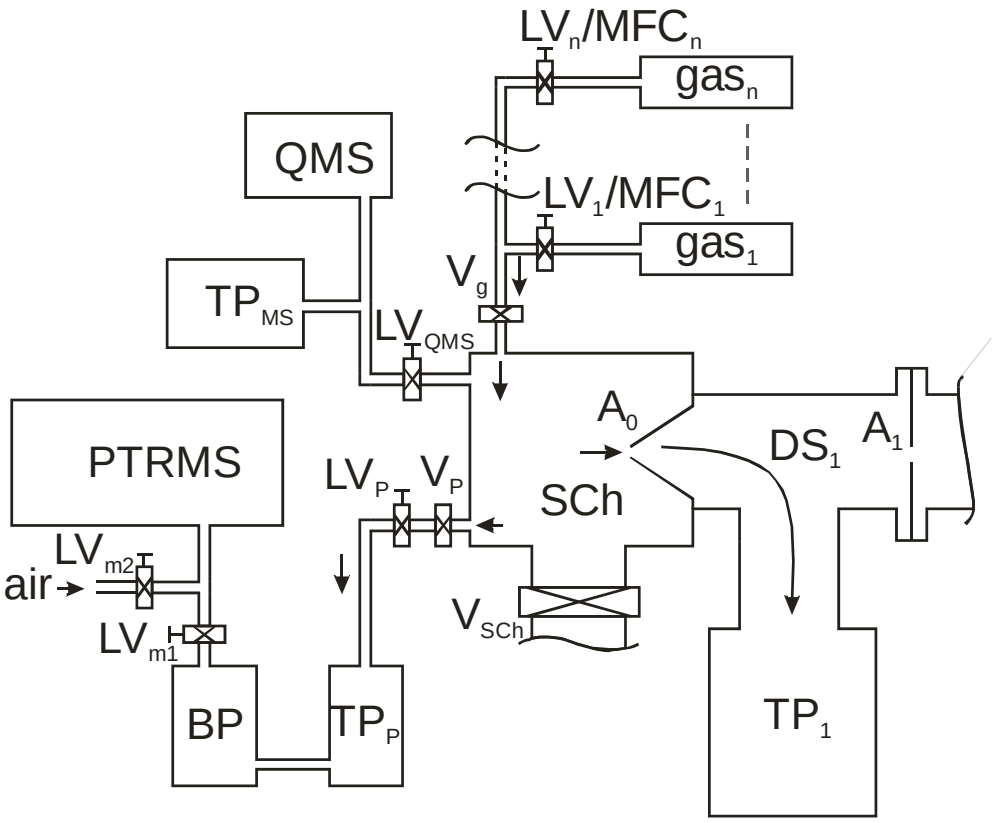

Gases or liquid vapors are introduced into the sample chamber (sample cell) ***SCh*** through the mass-flow controllers $\boldsymbol{MFC_{1,..,n}}$ or through the leak valves $\boldsymbol{LV_{1,..,n}}$. The outlet of the system is an aperture $\boldsymbol{A_0}$. Additional pumping can be provided through the process turbo-molecular pump $\boldsymbol{TP_P}$. A gas composition in the reaction chamber is monitored by the quadrupole mass-spectrometer ***QMS*** [41] and by the proton-transfer reaction mass-spectrometer ***PTRMS*** [42]. The quadrupole mass-spectrometer is connected to the sample chamber through the leak-valve $\boldsymbol{LV_{QMS}}$. The leak valve together with the turbo-pump $\boldsymbol{TP_{MS}}$ allows setting of a working pressure in QMS, which should be in the range 10^{-7}-10^{-6} mbar. PTRMS requires the inlet pressure of 1 bar. Therefore, it was connected to the outlet of the backing pump ***BP***. The outlet gas from the backing pump can be diluted with air if necessary. PTRMS can be also connected to the backing pump of the TP_1 if flow through the process pump TP_P is closed.

3.3.3 Electrostatic lenses.

3.3.3.1 Requirements for the electrostatic lens system.

As it was already discussed in previous chapters, the concept of the design of the described (our) system is exchange of a most part of the electrostatic lens system of a standard commercial analyzer by a home-made differential pumping system combined with a new electrostatic lens system. It was desirable to fit several practical conditions for the new electrostatic lens system:

1) Geometrical dimensions (diameter and total length) of the lens stages should fit the dimensions of the differential pumping stages.
2) The number of independent lens elements should not exceed the number of high-voltage power supplies in standard analyzer hardware. In this case lens voltages can be driven by the standard hardware and software, just the voltage table should be changed.
3) Calculated voltages should not exceed a maximum voltage provided by standard power supplies.
4) A best collection angle should be achieved.
5) A best focusing on the last aperture should be achieved, which means minimum aberrations of the system.
6) A magnification coefficient (enlargement) should be fixed over the whole electron kinetic energy range.
7) No significant deceleration should be applied to low energy electrons, otherwise electron trajectories will be significantly affected by weak magnetic fields always existing in an iron-containing system.

Additionally, several operation modes were planned for the electrostatic lenses:

1) The accelerating mode is a normal operation mode with acceleration of photoelectrons in the first differential pumping stage.
2) The low-voltage mode is supposed to avoid gas discharge in the first stage at high pressures by means of reducing voltage values.
3) The magnification mode should provide a high magnification to operate with a space-resolution detector (such as for example, a CCD camera with a phosphor screen).

Unfortunately, in spite of a great number of publications existing on the topic of electrostatic lens designing, no general theory for optimization of an electrostatic lens system exists. General properties of an electrostatic lens, the approach chosen for the lens system optimization and results of calculations will be presented bellow.

3.3.3.2 General information about electrostatic lenses.

Estimation of properties of an electrostatic lens usually includes two steps:

1) Estimation of a space distribution of electrostatic potential.
2) Estimation of trajectories of electrons or other charged particles in the electrostatic field.

In the case of a high volume charge of the particle beam this approach will not work, which is nevertheless not the case for a low-current electron flow in XPS (ca. 10^9 electrons/sec with 50 eV kinetic energy will induce on the aperture, where the influence is maximal, a voltage of circa 0.07 V).

The electrostatic potential ***V*** in neglecting of an electron beam charge should satisfy Laplace equation:

$$\Delta V = 0 \qquad (3\text{-}20)$$

where Δ is the Laplace operator. Estimation of a potential distribution implies solution of the Laplace equation with certain boundary conditions.

A trajectory of an electron can be calculated by solving the non-relativistic equation of motion (which has a relativistic correction less than 1% for an electron kinetic energy of up to 10 KeV):

$$m\frac{dv}{dt} = e \cdot \nabla V \qquad (3\text{-}21)$$

where ***v*** is an electron velocity vector, ***e*** and ***m*** are the charge and the mass of an electron respectively and ∇ is the Hamilton operator.

In the case of the rotational symmetry the paraxial approximation (small r and r') allows treating an electrostatic lens as a thick lens by analogy with geometrical optics (Figure 3-18).

Figure 3-18. Notation of thick electrostatic lens parameters
according to [44].

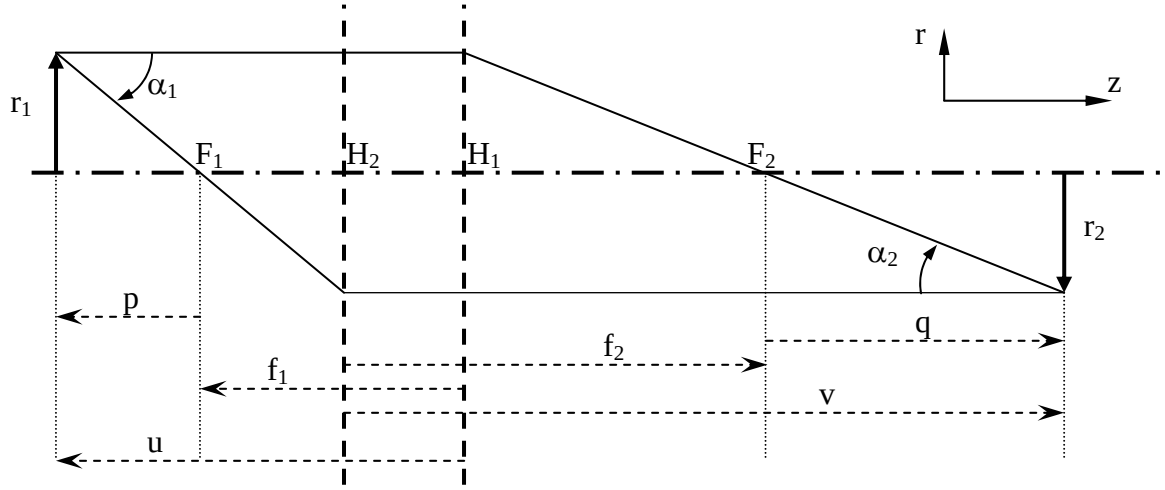

Here r_1 and r_2 are sizes of an object and an image respectively, H_1 and H_2 are the principle planes, F_1 and F_2 are the focal points. The rays should be considered as the asymptotes of the electron trajectories at $z \to \pm\infty$ because electrostatic lenses have no sharp boundaries between media with different refraction coefficients, but rather a smooth potential change, which lead to curved trajectories.

The thick lens approach makes the problem of an electrostatic lens system construction analogous to the problem of an optical system construction. An electrostatic lens system can be constructed from separate lenses with desired characteristics, which can be easily calculated and adjusted by lens voltages as it will be discussed below. In the case of a small distance H_1H_2 comparing f_1, f_2, u and v the problem can be simplified by using the thin lens approach.

A trajectory equation derived from (3-21) for a system with rotation symmetry will have the form:

$$r'' + \frac{1}{2}\frac{V'}{V}r' + \frac{1}{4}\frac{V''}{V}r = 0 \qquad (3\text{-}22)$$

where r is a distance from the axis of symmetry, V is always taken at r=0 and differentiation is made by the variable z, which is the coordinate along the axis of symmetry.

By introduction of the reduced radius $R=rV^{1/4}$ the equation (3-22) will be reduced to Picht equation [43]:

$$R'' = -\frac{3}{16} \cdot R \cdot \left(\frac{V'}{V}\right)^2 \qquad (3\text{-}23)$$

From this equation one can conclude that R" always has a sign which is opposite to the sign of R. This means that an electron trajectory is always curved towards the z axis and a lens is always convergent.

A distribution of a potential can be calculated numerically using equation (3-20) and boundary conditions. After this the lens cardinal points can be estimated by numerical simulation of two principle rays (those are parallel to the optical axis z at $z\rightarrow+\infty$ and at $z\rightarrow-\infty$) using the equation (3-23). Such an approach is realized in the program LENSYS [44]. Potential distributions for some lens geometries were calculated numerically and stored in a data file. This approach allows fast adjustment of lens voltages without performing extensive and time consuming calculations. Lens parameters received by this method can be further adjusted by other software. The program SIMION [45] calculates a potential distribution with a user-defined lens geometry, space step and lens voltages. Electron trajectories are calculated by use of equation of motion (3-21) without the paraxial approximation. Such a method allows achievement of more realistic results comparing the program LENSYS, while consuming more time and computer resources.

The figure of merit of a system design besides the collection angle should be a minimum size of the spot of an electron beam on the last aperture, which means minimum spherical aberrations of the system. The spot size of a mono-energetic electron beam in the image plane is given by the formula:

$$r = MC_s\alpha_0^3 \qquad (3\text{-}24)$$

where $\boldsymbol{r}$ is a spot radius, $\boldsymbol{M}$ is a magnification coefficient, $\boldsymbol{\alpha_0}$ is a collection half-angle and $\boldsymbol{C_s}$ is a coefficient of spherical aberrations. The problem of minimization of aberrations thus, reduces to the problem of minimization of the product MC_s or even of C_s if M is fixed.

The formula for an aberration coefficient is expressed [44] as:

$$C_s = \frac{1}{64\cdot V_0^{1/2}}\int_{-\infty}^{\infty}\frac{R^4}{V^{1/2}}\left[(3T^4+5T'^2-\frac{11}{2}T^2T')+4TT'\frac{R'}{R}\right]dz \qquad (3\text{-}25)$$

where V is an axial potential, $T(z)\equiv V'(z)/V(z)$, $V_0=V(-\infty)$ and R(z) corresponds to the ray which passes through the axial object point with the unit slope.

This equation is hard to apply directly to optimization of lens geometry and voltages, but some practical conclusions can be derived for minimization of C_s:

1) R should be minimized, i.e. electron trajectories should be as close to the axis as possible

2) R' should be minimized, i.e. electron trajectories should be as smooth as possible.

Unfortunately, no practically useful relation can be drawn between an aberration coefficient of the whole lens system and aberration coefficients of separate lenses as can be done for example for focal properties. The only rule is an overall aberration coefficient will decrease/increase with decreasing/increasing of any aberration coefficient. Nevertheless, contributions of different parts of a lens system into an overall aberration coefficient do not have to be equal or even of one order of magnitude.

3.3.3.3 Calculation of the electrostatic lens system.

The general idea of the electrostatic lens system design was developed by analogy with geometrical optics, i.e. the system is constructed from a limited number of thin lenses.

The differential pumping system consists of three stages. This means that the electrostatic lens system should also contain three independent parts (see Figure 3-19). The first two stages require development of a lens system, while the third one was initially designed as a differential pumping stage and should not be changed. The third part is intended for work with photoelectrons of one tenth of initial photoelectron kinetic energy E_{k0}. This means that the first lens element of the third lens stage and correspondingly, the last lens element of the second lens stage should have the voltage of $-0.9 \cdot E_{k0}$, supposing E_{k0} is measured in eV. Photoelectrons are decelerated by the third stage to the kinetic energy equal to the pass energy of the analyzer E_p.

Figure 3-19. Electron kinetic energy in the lens system.

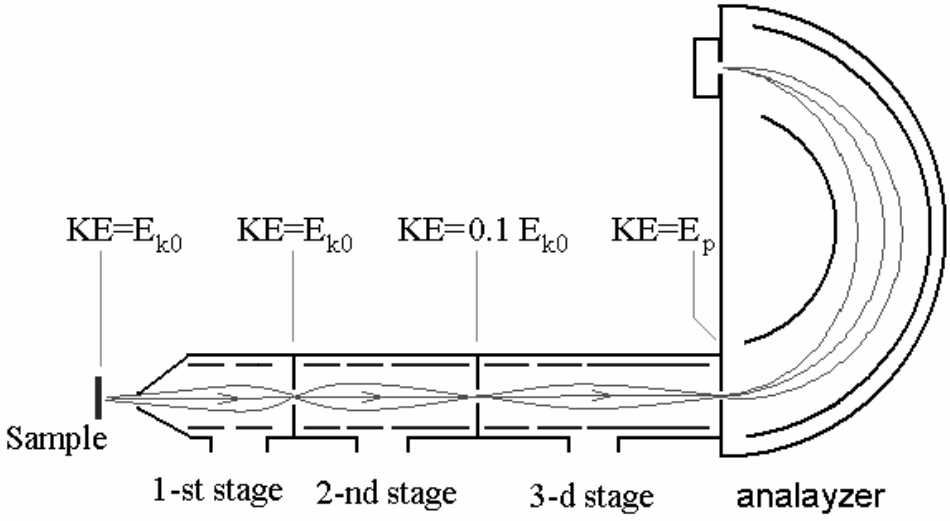

Deceleration of photoelectrons from E_{k0} to $0.1 \cdot E_{k0}$ can be done even in the first stage or in the second stage or in both step-by-step. It was performed in the second stage because it is more preferable to keep a high electron energy in the first stage where a gas pressure can be quite high and consequently, scattering of low-energy electrons can be significant.

The concept of the lens design is shown on Figure 3-20.

Figure 3-20. Concept of the lens design by analogy with geometrical optics.

a. Acceleration and low-voltage modes

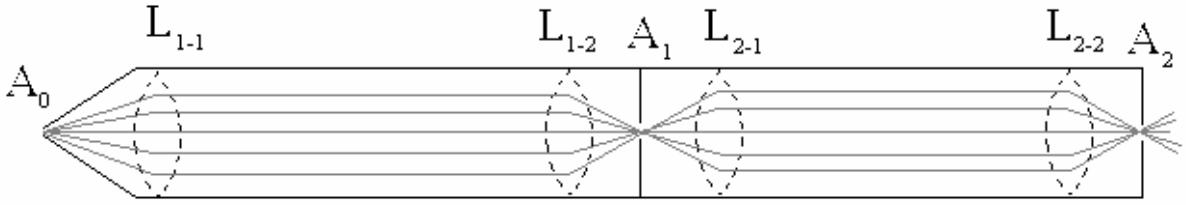

b. Magnification mode

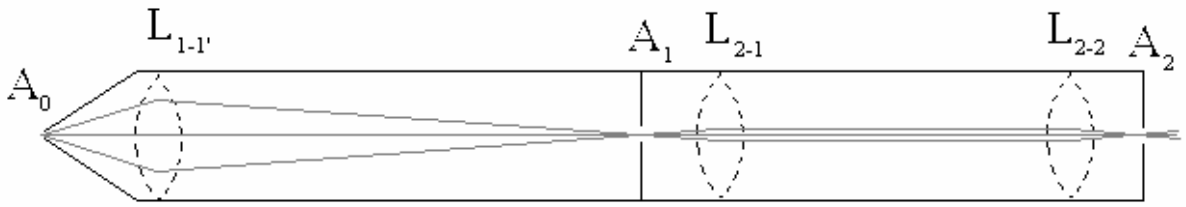

From this drawing it is obvious that the lens $L_{1\text{-}1}$ as well as the lens $L_{1\text{-}1'}$ should be as close to the aperture A_0 as possible to provide a maximum collection angle. A focal length of the lens $L_{1\text{-}1}$ should be the same as the distance $A_0L_{1\text{-}1}$, while a focal length of the lens $L_{1\text{-}1'}$ should satisfy (in the approximation of a thin lens) the equation:

$$\frac{1}{f} = \frac{1}{A_0 L_{1-1'}} + \frac{1}{L_{1-1'} A_1} \qquad (3\text{-}26)$$

The first part of the system in the acceleration mode should be symmetrical with respect to the center.

Fast fitting of lens geometry and voltages was performed in the program LENSYS [44]. This program is able to estimate the focal properties of a single lens or a small lens system and to calculate the aberration coefficient C_s and magnification M. Fine adjustment of the voltages was performed in the program SIMION ([45]).

The minimum length of the differential pumping system was estimated to be 70 cm (see page 28). In reality the length should be increased to 83 cm to provide a space for mounting turbo-pumps and for assembly work. Further increasing of the length would not influence the photoelectron collection of our system in a positive way. The lengths of the differential pumping stages are listed in Table 3-2 on page 30. Choice of the inner diameter of lens elements determines the length of a lens stage in units of the diameter. Decrease of the diameter allows decreasing of an aberration. Nevertheless, too small diameter will limit the collection angle. The diameter of the lens elements in the first and second stages was chosen to be 40 mm. It is less than of 60 mm, which is the inner diameter of the elements of the

standard analyzer [46]. The third differential pumping stage was not changed, which implies the inner diameter of the lenses in this stage of 60 mm.

The first stage should keep an electron kinetic energy at exit aperture A_1 to be the same as after leaving the sample ($KE=E_{k0}$). The magnification in this stage should be about unity for the acceleration and low-voltage modes and about 5 for the magnification mode.

The second stage should decelerate photoelectrons to 0.9 of initial kinetic energy E_{k0} to provide the interfacing with third stage that was designed by the manufacturer of the analyzer. The magnification of the third lens stage should be about unity for all the modes. Lens voltages for the first two lens stages can be calculated for some electron kinetic energy and afterwards scaled linearly for any other one.

Five independent power supplies from the standard analyzer hardware are available for the first two stages: This is the limit for a number of lens elements.

As it was already discussed before, the first lens should be situated as close to the inlet aperture as possible to provide a best possible photoelectron collection angle. For such a condition it would be reasonable to choose for the first lens stage the symmetrical scheme with two lenses $L_{1\text{-}1}$ and $L_{1\text{-}2}$ as it is drawn on Figure 3-20a. This scheme provides the unity magnification with minimal aberrations because a photoelectron trajectory will be parallel to the z-axis on a most part of the way, which is the smoothest and closest to the axis trajectory. The lens elements of the lens $L_{1\text{-}1}$ can be also used for the lens $L_{1\text{-}1'}$ in the magnification mode. The scheme for the magnification mode (Figure 3-20b) will also provide a desired magnification coefficient and aberrations will be minimized. The lens geometry for the acceleration mode was calculated taking into account the maximum voltage of 3500 V provided by the power supplies, which should correspond to the upper limit of electron KE range of 1400 eV. Three-element lenses $L_{1\text{-}1}$ and $L_{1\text{-}2}$ were used because a two-element lens cannot satisfy simultaneously the voltage and geometrical conditions. A four-element lens would not bring significant improvement of aberration, but will need an additional power supply. The lenses $L_{1\text{-}1}$ and $L_{1\text{-}2}$ are formed by the electrodes #1, #2, #3-#5 and #3-#5, #6, #7 respectively (see Figure 3-21 and Table 3-4).

Figure 3-21. Electron trajectories for the first two lens stages. (calculated in SIMION)

Acceleration mode

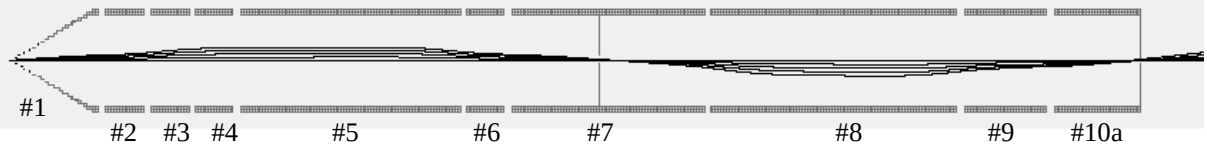

Magnification mode

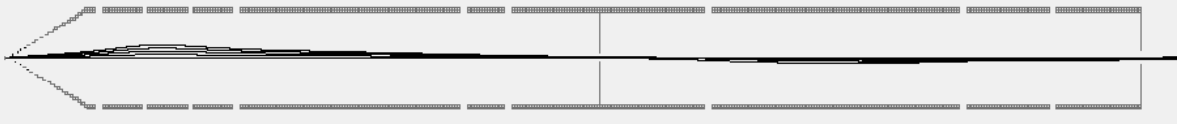

Low-voltage mode

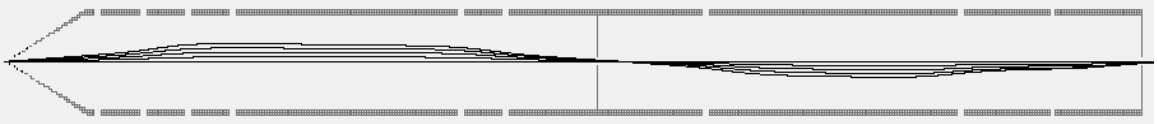

Table 3-4. Table of lens voltages for the first two stages. D=40 mm

		Voltage/E_{k0}, V/eV		
Electrode	Length, mm	Acceleration mode	Magnification mode	Low-voltage mode
#1	40	0	0	0
#2	20	2,5	-0,9	
#3	20	-0,55		-0,875
#4	20		-0,5	
#5	100		0	
#6	20	2,5		
#7	40+48	0		0
#8	112	-0,9	-0,9	-0,9
#9	40	-0,4	-0,5	-0,45
#10a	40	-0,9	-0,9	-0,9
M		2	5	2
Cs/D, rad^3		35	21	45
MCs/D, rad^3		**70**	**105**	**90**

The length of electrode #1 is determined by geometrical reasons and the length of electrode #2 was set to the minimum value of D/2 at which the electrical field still can be found as a superposition of the electrical fields of contiguous electrode pairs. The voltage of electrode #3-#5 may be experimentally adjusted, while voltages #2 and #6 are fixed to the calculated value. In the magnification mode the four-element lens $L_{1\text{-}1'}$, consisting of electrodes #1, #2-#3, #4, #5-#7, is employed. Electrode #4 here also plays an adjustable role.

For the low-voltage mode two two-electrode lenses are enough. The lenses are formed by electrodes #1-#2, #3-#6 and #3-#6, #7 respectively. The lens geometry for this mode is slightly asymmetrical, which nevertheless, does not worsen lens characteristics, but makes it possible to adjust the focusing by one voltage only. The mode has the advantage of low voltage values, which allow to avoid gas discharge at high pressures in the sample cell. However, photoelectrons in this mode are decelerated to $0.125 \cdot E_{k0}$ on a most path, which is 5 eV for E_{k0}=40 eV. Photoelectrons of such a low kinetic energy can be easily deflected by a relatively weak electric or magnetic field. Therefore, the acceleration mode is more preferable as compared to the low-voltage mode if no danger of gas discharge is present.

Estimation of the pressure at which gas discharge appears is not trivial in our case because experimental data for a breakdown voltage are usually available for pressure·distance values starting from ~1 Torr·mm (1 Torr= 1.32 mbar), which corresponds to the breakdown voltages of several hundred volts. In our case the maximum voltage difference between neighbor lens elements is 3500 V. The gap between lens elements is 2 mm and a maximum pressure in the first differential pumping stage is in the 10^{-3} mbar range (see Table 3-3). This corresponds to a maximum pressure·distance value in the 10^{-3} Torr·mm range. Experimental curves for the breakdown voltage vs. pressure·distance (so-called Paschen curves) ([47], [48], [49]) were extrapolated for low pressure·distance values to obtain the information for the required region. A pressure at which breakdown should occur at 3500 V on the distance of 2 mm is 0.1-0.7 mbar for such gases as H_2, NO, CO_2, SO_2, Air [47] and Ar [48]. Therefore, no gas discharge is expected for diatomic and monoatomic gases. Nevertheless, for bigger molecules such as for example, some saturated hydrocarbons (normal pentane, hexane, heptane, octane and decane) gas discharge in the first differential pumping stage can occur already at $0.4 \cdot 10^{-5}$-$2 \cdot 10^{-4}$ mbar [49], which corresponds to a pressure in the sample cell of 0.1-0.5 mbar.

The second lens stage is the same for all three modes. The electrons here should be decelerated to $0.1 \cdot E_{k0}$, which means that the voltage of the last electrode should be $-0.9 \cdot E_{k0}$ V, where E_{k0} is in eV units. This stage is formed by the two-element lens $L_{2\text{-}1}$ (electrodes #7, #8) and by the three-element lens $L_{2\text{-}2}$ (electrodes #8, #9, #10a). A voltage of the electrode #8 is fixed to the same value as a voltage of the electrode #10a and a voltage of electrode #9 can be adjusted. The calculated voltages for the first two stages are listed in Table 3-4.

The third lens stage was designed by the manufacturer. Voltages cannot be scaled just with photoelectron kinetic energies in this stage as it was done in the first and second stages.

The stage consists of three elements: #10b-#11, #12, #13-#14 (see Figure 3-22 and Table 3-5).

Figure 3-22. Electron trajectories for the third lens stage (calculated in SIMION).

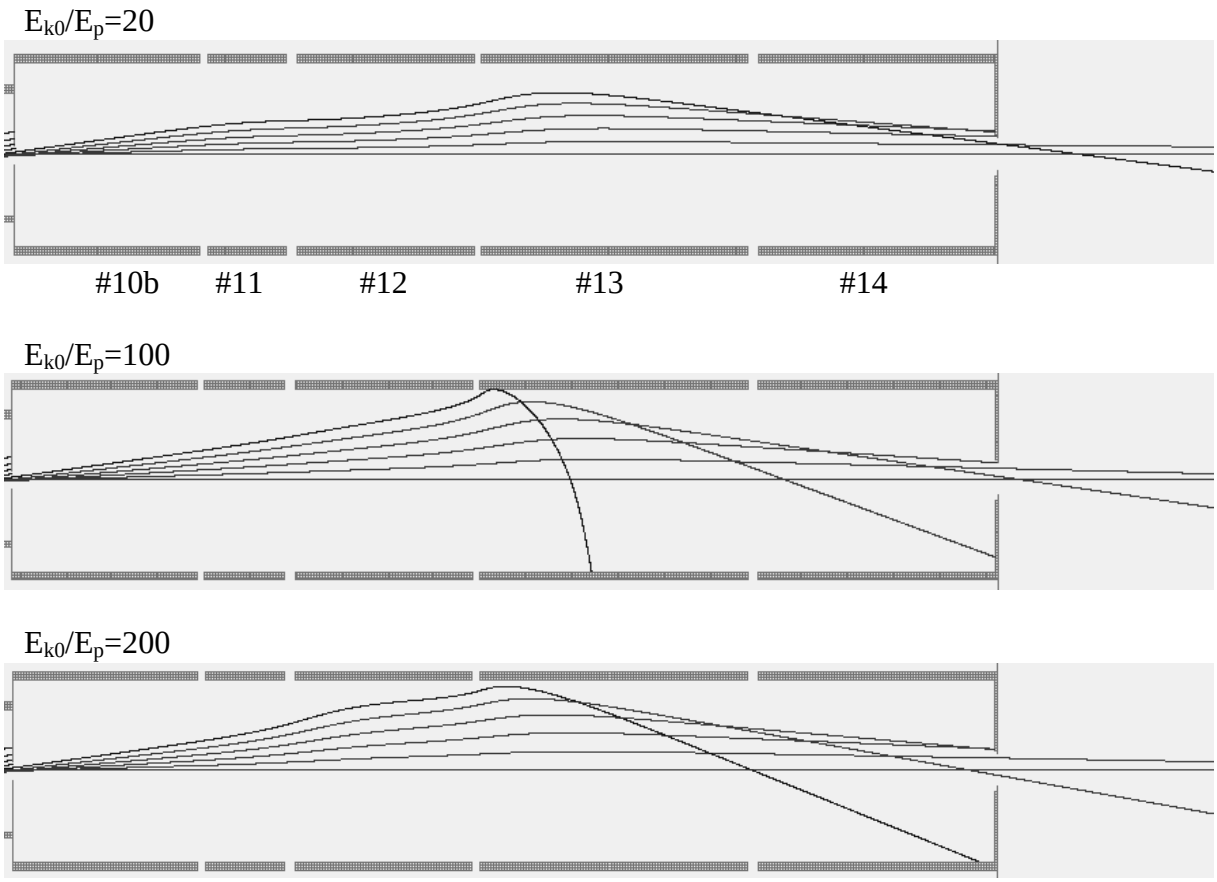

Table 3-5. Table of lens voltages for the third stage. D=60 mm.

Electrode	Length, mm	Voltage/Ep, V/eV
#10b	63	$-0.9E_{k0}/E_p$
#11	29	
#12	62	$-E_{k0}/E_p$+spline(E_{k0}/E_p)
#13	91	$-E_{k0}/E_p$+1
#14	89	

The kinetic energy of photoelectrons at the entrance of the stage should be $0.1 \cdot E_{k0}$ and consequently, the voltage on the first lens electrode (#10b-#11) is $-0.9E_{k0}$ V (here E_{k0} is in eV). At the exit of the stage photoelectrons should have the kinetic energy equal the pass energy of the analyzer E_p. Therefore, the voltage of the third lens element is $-E_{k0}+E_p$ V (E_{k0} and E_p are in eV). A voltage of the second element should be a function of the ratio E_{k0}/E_p. The voltage was calculated for several electron kinetic energies and the spline function

(Figure 3-23) is used by the voltage-driving software. A collection angle and an aberration of this stage is a function of the ratio E_{k0}/E_p (see Figure 3-22).

Figure 3-23. Spline function for the voltage in the third stage.

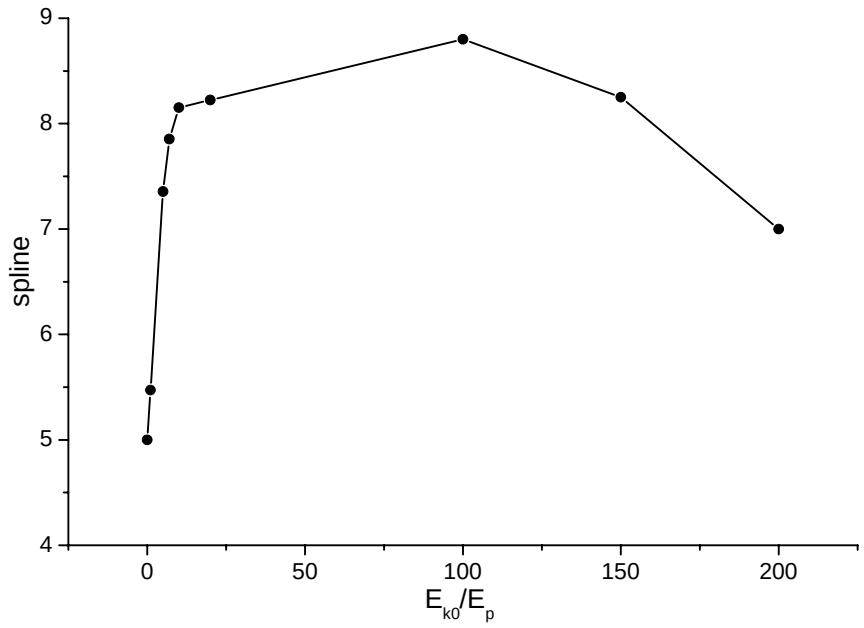

A scheme of the calculated electrostatic lenses and of the differential pumping system is presented on Figure 3-24 and a general view of the spectrometer is shown on Figure 3-25.

Figure 3-24. Scheme of the differential pumping system and electrostatic lenses.

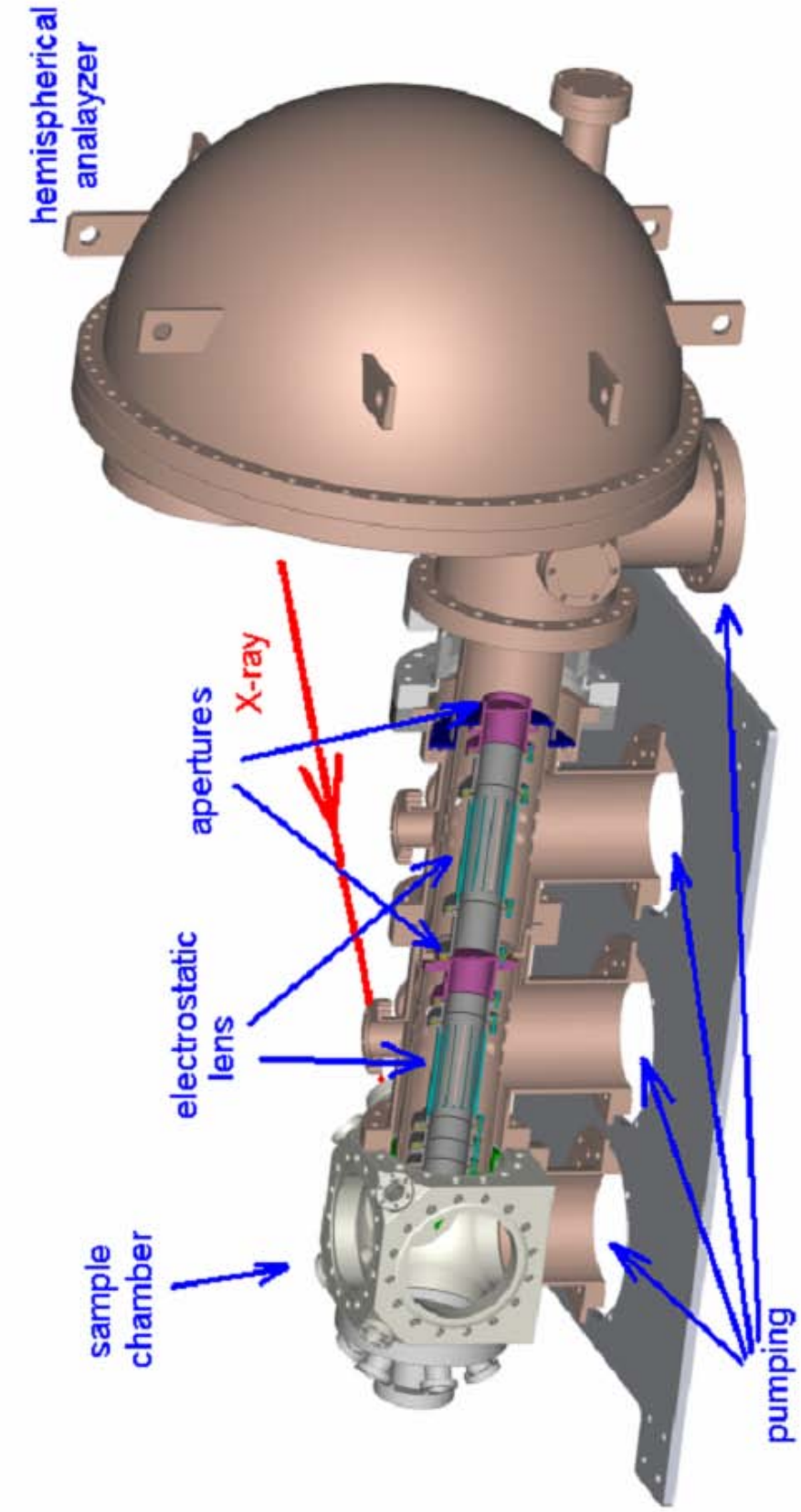

Figure 3-25. Scheme of the *in situ* XPS instrument.

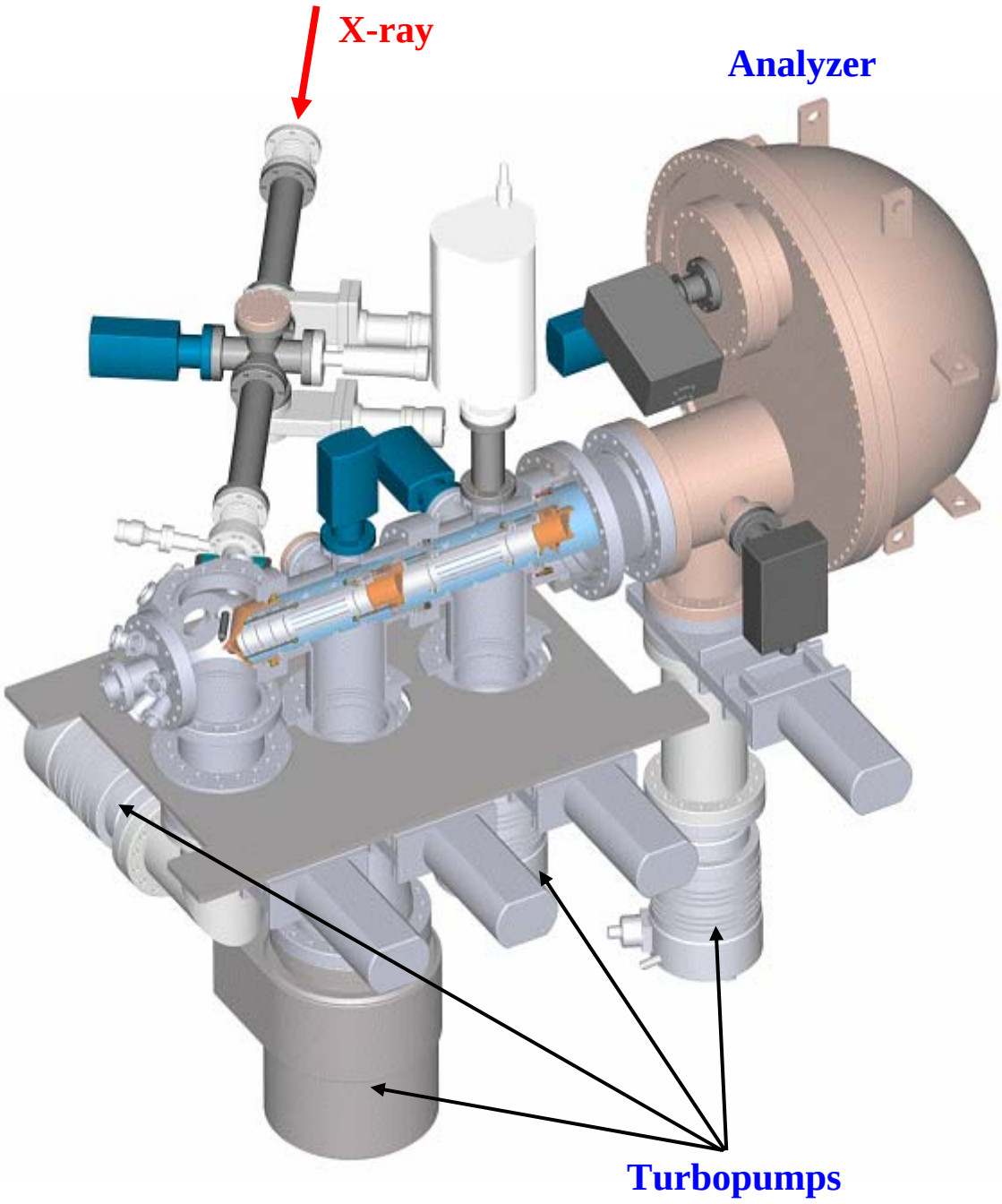

3.4 Peculiarities of data analysis in high-pressure XPS

Data analysis in XPS usually includes element identification, estimation of stoichiometric ratios and estimation of an oxidation state from a chemical shift or from fitting the peak shape by sum of several components. Work with a laboratory X-ray source implies also subtraction of satellites appearing because of non-monochromatic X-ray, which is nevertheless, not the case for monochromitized synchrotron radiation.

Though the procedure for XPS spectra analysis is well described in many publications (see for example [22]), analysis of high-pressure XPS data differ in some points from ordinary XPS.

Firstly it is concerning a BE shift, which appears because of charging. Gas composition, pressure and sample temperature influence the value of charging (see for example Figure 3-26). In addition, our setup is constructed for work with synchrotron radiation. This means the presence of variations in X-ray intensity and as a consequence, the presence of variations in a sample surface charging. This fact makes charge correction much more complicated comparing ordinary XPS in the case of an insulating or semiconducting material. One should always have a reference in the spectrum for BE correction, such as for example, the O1s peak for vanadium and titanium oxides or the Au4f peak from gold atoms deposited on the surface especially for this reason[*].

Figure 3-26. Apparent binding energy of the O1s peak of a VPO catalyst depending on a temperature [81].

The catalyst was heated up in a mixture of n-butane/helium and oxygen at the total pressure of 2 mbar.

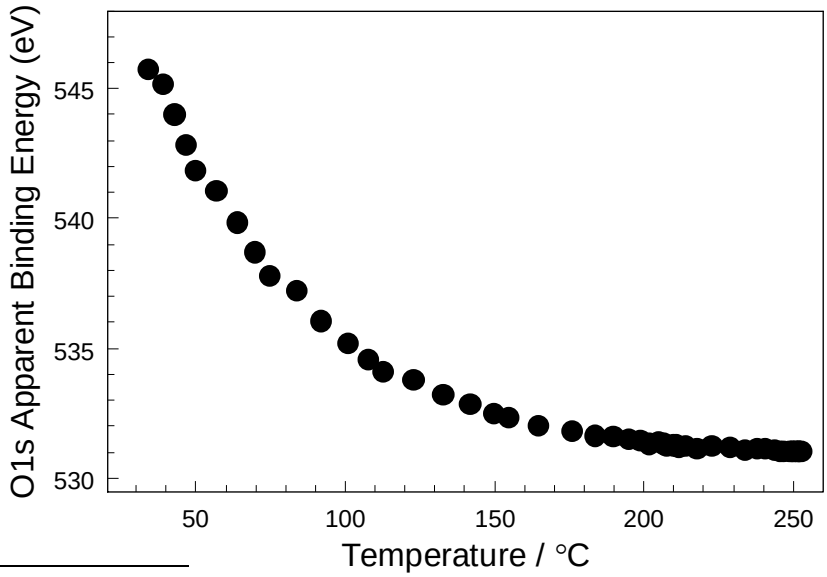

[*] Nevertheless, gold deposition is not recommended for catalysts because gold nanoparticles are known to be catalytically active.

The ***second*** difference is in estimation of stoichiometric ratios. Photoelectrons emitted from the sample surface are scattered elastically and inelastically by gas phase molecules resulting in a different spectrum background shape as compared to vacuum (Figure 3-27).

Figure 3-27. Au4f XPS peak shape for different Ar pressures.

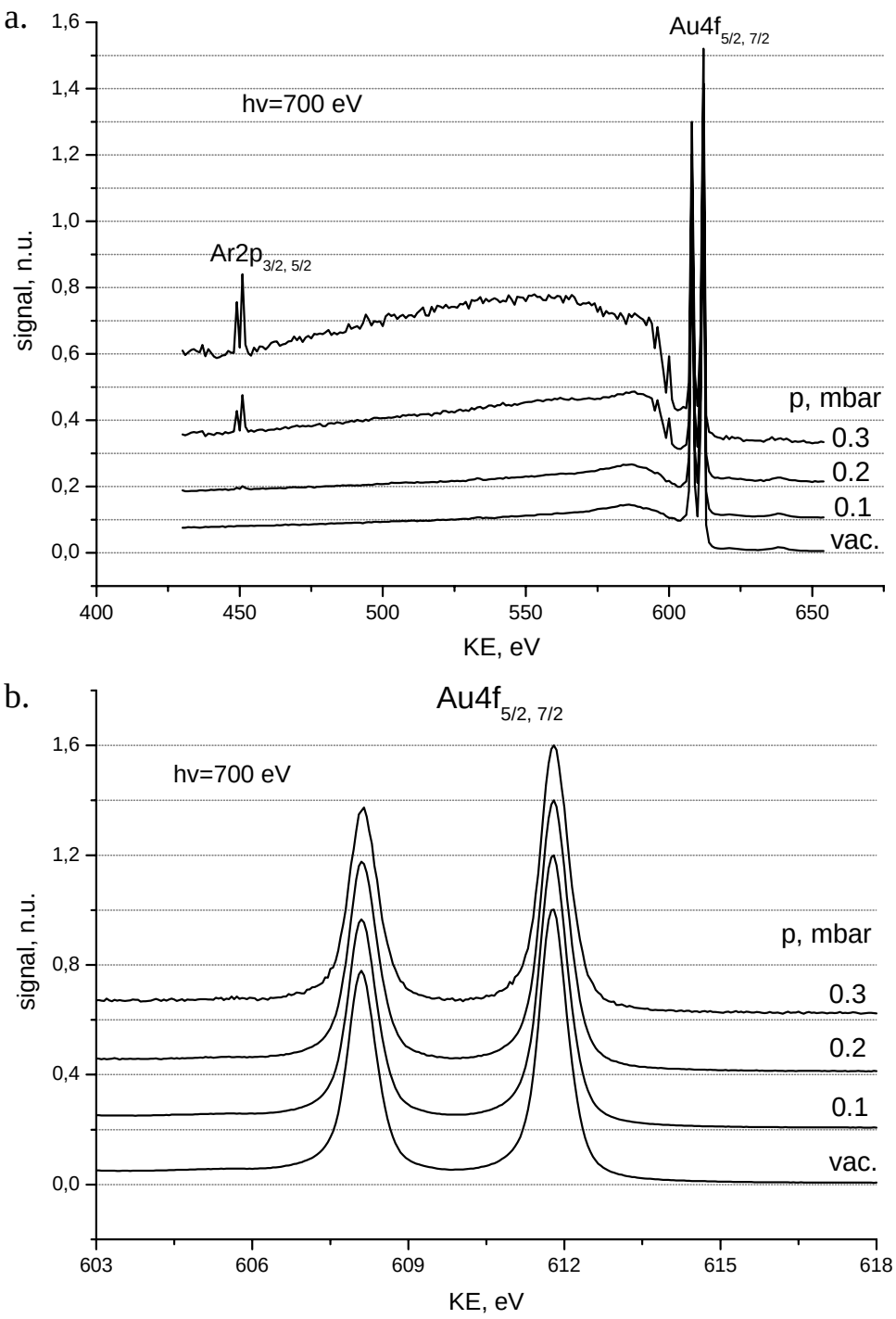

The scattering process changes the overall transmission function of the spectrometer. Moreover, the transmission function in high-pressure XPS depends also on a pressure and on a gas composition. To calculate a change in the transmission function because of the scattering process the scattering cross-sections should be known as a function of an electron kinetic energy (the data in literature about them is very poor). Additionally, experimental geometry should be taken into account and a pressure distribution near the first aperture should be calculated. Estimation of the pressure distribution implies extensive numerical calculations because the analytical approaches do not work in the case of a pressure in the mbar range (see part 3.3.2). Nevertheless, use of synchrotron radiation makes it possible to avoid all these difficulties. Excitation energy can be tuned in such a way, that photoelectron kinetic energies for two different peaks, taken in separate scans, will be equal to each other. In this case an overall transmission function of the spectrometer will be the same for both peaks because the transmission function depends only on an electron kinetic energy and it will not be necessary to take into account the scattering of photoelectrons by gas phase. Moreover, one more advantage will be achieved by this approach: an information depth depends on the photoelectron kinetic energy only. This means that the same information depth will be achieved for both elements. The formula for a stoichiometric ratio in this case will have the form (3-7). The cross-section σ and the X-ray flux f (after the X-ray window) should be known or measured. The intensity should be always monitored by a photodetector or referred to a synchrotron ring current.

The ***third*** difference in the spectra analysis between ordinary and high-pressure XPS can be a background subtraction. Although, a Shirley-type background [19] gives quite accurate results and at the same time is well practical, the series of works of S. Tougaard [50, 51, 52, 53] showed dependence of the background on a photoelectron path in a scattering medium. The author had even tried to extract from the background shape a value of a mean free path of photoelectrons. In the case of the presence of gas phase scattering depends on a pressure (equation (3-11)). Change in the background shape with pressure is clearly visible on Figure 3-27a. At the same time Figure 3-27b shows that the peak shape is not affected by scattered photoelectrons and the same type of background (for example, Shirley) can be applied to spectra taken at different gas pressures in a close neighborhood of the peak.

3.5 Monitoring the catalytic performance: gas-phase XPS peaks, MS and PTRMS.

The most common techniques for reaction products registration in catalytic investigations are MS and gas chromatography. Our system provides the possibility to register reaction products by PTRMS and conventional MS. A scheme of connection of the mass-spectrometers is drawn on Figure 3-17 (page 31).

A description of the conventional ***quadrupole mass-spectroscopy*** technique ***with ionization*** of gas molecules ***by the electron beam*** can be found in many literature sources (for example in [54]). Our system employs the possibility to obtain mass-spectra of a gas inside the sample cell with a BALZERS PRISMA™ quadrupole mass-spectrometer [41] connected to the sample cell as it is shown on Figure 3-17. The operating pressure in this mass-spectrometer should be in the 10^{-7}-10^{-6} mbar range. To keep this pressure the mass-spectrometer volume is pumped by the turbopump $\boldsymbol{TP_{MS}}$. A gas flow and consequently, a pressure in the mass-spectrometer are regulated by the leak-valve $\boldsymbol{LV_{QMS}}$. A gas flow through the leak valve is negligible comparing a gas flow through the aperture A_0 and through the process pump TP_P, if the leak valve LV_P and the valve V_P are open. The conventional mass-spectrometry technique has nevertheless, quite limited suitability for detection of big molecules, such as for example, a molecule of maleic anhydride, because of a complicated dissociation-fragment pattern. To register such kind of molecules the ***proton transfer reaction mass-spectrometry (PTRMS)*** was applied. A description of this not widespread technique can be found in [55]. A schematic diagram of the PTRMS instrument [42] is shown on Figure 3-28.

Figure 3-28. Schematic diagram of the PTRMS system according [55].

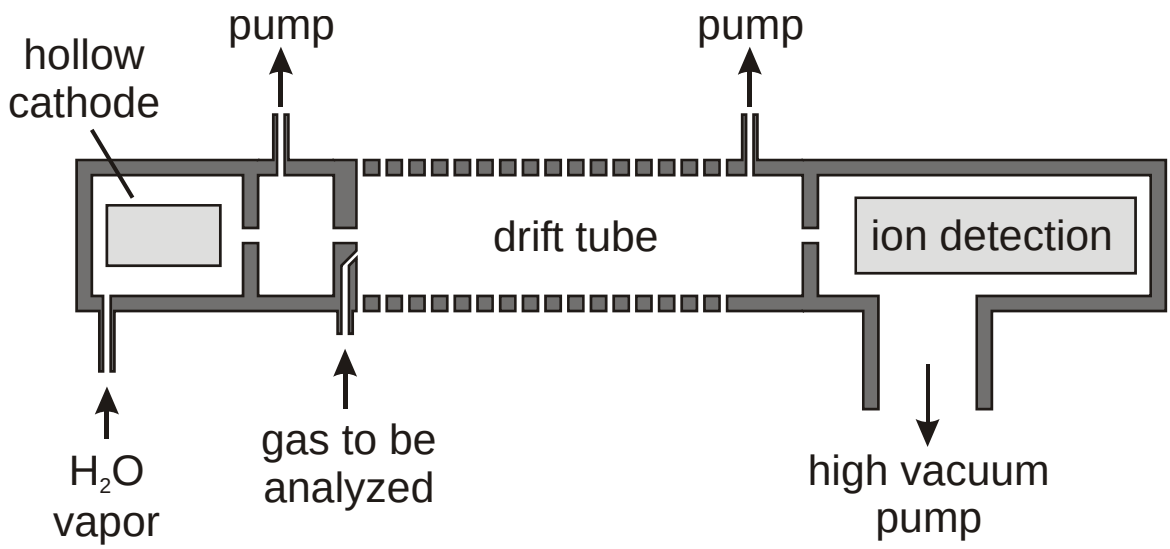

Diluted in a buffer gas (which is usually air) investigated gas is supplied to the drift tube. H_3O^+ ions are produced in the hollow cathode by ionization of water molecules and injected into the same drift tube. The ions collide with buffer gas molecules without reacting with them and thus, being kinetically thermalizied. Once the ion meets an investigated gas molecule ***R*** it may undergo the reaction

$$H_3O^+ + R \rightarrow RH^+ + H_2O \qquad (3\text{-}27)$$

To make this reaction possible the molecule R should have a higher proton affinity as compared with a water molecule. Therefore, not all chemical compounds can be investigated by the PTRMS method. For example, butane and CO_2 molecules have lower proton affinity than water, but maleic anhydride can be readily protonized by H_3O^+. Produced RH^+ ions will be further moved in the drift tube by electrical field and registered by the ion detection system, which is analogous to the detection system of a quadrupole mass-spectrometer. A scheme of connection the PTRMS instrument to the sample cell is also drawn on Figure 3-17. In the described experiment the investigated gas is compressed by the baking pump ***BP*** and diluted with air or nitrogen afterwards. The PTRMS instrument allows measurement of an absolute concentration of investigated gas molecules in the drift tube, which is proportional to the concentration in the sample cell.

Another type of a technique for registration of gas-phase reaction products is analysis of gas-phase XPS peaks. Such kind of analysis was performed in [33] to monitor O_2, CO_2, H_2O, CH_2O and CH_3OH presented in gas phase during the process of selective oxidation of methanol to formaldehyde on a copper catalyst. This technique is very useful for *in situ* XPS because it does not require any additional equipment such as a mass-spectrometer.

Unfortunately, gas peaks are very sensitive to the charging effect and the analysis is almost impossible with insulating samples.

4 Vanadium phosphorus oxide catalyst

The object of this investigation is a vanadium phosphorus oxide catalyst, which is an important industrial catalyst for oxidation of *n*-butane to maleic anhydride. In part 4.1 will be given a short introduction about this catalyst including a state of the catalyst in modern economics, conditions of operation and catalyst preparation procedures. A review of published up to date experimental data and theoretical ideas concerning the active species on the VPO surface is given in part 4.2. Parts 4.3-4.8 are devoted to the experimental procedure, experimental data and its analysis. The experimental results will be discussed in part 4.9 from the point of view of their meaning for understanding of the nature of catalytically active species and the strategy of improvement of a VPO catalyst.

4.1 VPO catalyst for industrial production of maleic anhydride from *n*-butane.

Maleic anhydride (MA) is an intermediate in industrial production of such chemicals as unsaturated polyester resins, fumaric and maleic acids, lube oil additives, maleic copolymers, agricultural and others (Figure 4-1).

Figure 4-1. Consumption of MA in different fields of economics in the United States according [60].

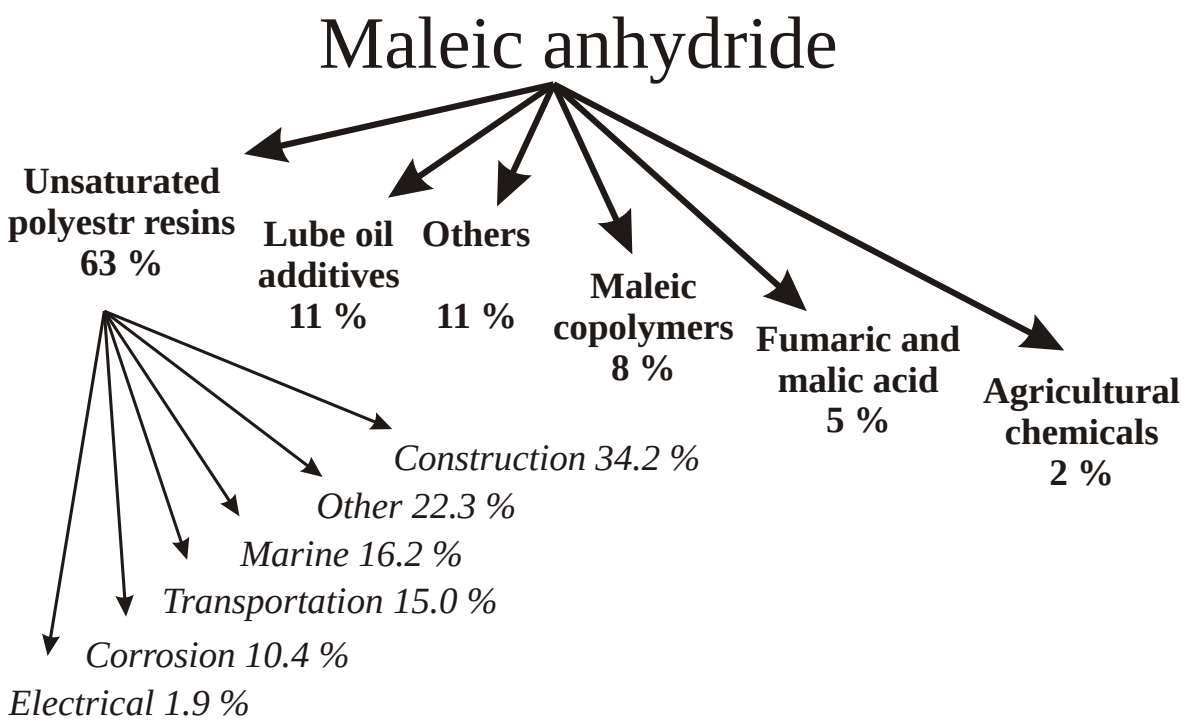

The main consumption of MA is in production of polyester resins, which are widely used in construction, boat-building, automotive and electrical industries in the form of so-called glass reinforced plastics. MA was first prepared in 1830s [56, 57] and commercial manufacture began a hundred years later in 1933 by National Aniline and Chemical Co., Inc., using a process based on benzene oxidation catalyzed by the vanadium oxide catalyst [58]. Benzene had been used as the only raw material for industrial production of MA till 1970s then economical reasons and recognition of benzene as a hazardous chemical intensified search for an alternative feedstock. Various C_4 compounds were evaluated as possible substitutes for benzene and finally, industry came to production of MA by oxidation of *n*-butane catalyzed by vanadium phosphorus oxide (VPO), which was discovered as a catalyst in 1966 [59]. Nowadays (in 2000) 100% of MA in the US and more than 65% of the world

amount (1359 kiloton/year) [60] are produced by the oxidation of *n*-butane (Figure 4-2) and VPO is the only industrial catalyst for this reaction.

Figure 4-2. Reaction of *n*-butane oxidation to MA

$$C_4H_{10} + 7/2\ O_2 \rightarrow C_4H_2O_3 + 4H_2O \quad \Delta H=-1236\ kJ/mol\ C_4H_{10}$$

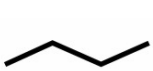

n-butane

maleic anhydride

Three different types of industrial process for obtaining MA from *n*-butane can be distinguished, i.e. the fixed-bed process, the fluidised-bed process and the recirculating-solids process.

A ***fixed-bed reactor*** consists of a number of tubes, which are packed with coarse catalyst bodies. The reactants (*n*-butane and air) flow through these tubes. As far as a mixture of *n*-butane in air has the concentration explosion limit of about 2 vol.% of n-butane, special care should be taken in this process about mixing and pre-heating of the gases before the reaction zone. High exothermicity of the reaction brings also the problem of hot spots in the reactor, which should be solved by a complicated cooling design or by reducing a catalyst activity.

Application of a ***fluidised-bed reactor*** reduces the problems of the gas explosivity and hot spots, but puts strict limitations on a catalyst particle size (10-150 microns). In this process reaction gases flow upward through the bed of the catalyst particles. A gas flow is adjusted in such a way, that the force of the flow on a catalyst particle is equal to a weight of the particle and the catalyst bed is brought in continuous motion.

DuPont company operates the ***process in the recirculating-solids reactor***. In this kind of process the oxidation of *n*-butane by lattice oxygen of the catalyst and regeneration of the catalyst by gas-phase oxygen are carried out in two separate reaction zones. Such a process allows increased selectivity towards MA and almost completely solves the problem of explosivity, but because of difficulties to control the regeneration process on a large industrial scale this process had not got wide spread up to now.

Technical peculiarities impose different requirements for properties of a catalyst material in these processes, i.e. different requirements for heat conductance, particle size, attrition resistance, activity, ability to regenerate and to supply bulk oxygen to the surface. Consequently, the term "catalyst optimization", which often appears in scientific literature

concerning VPO has sense only in view of certain process. Usually people understand by this term increasing of selectivity of a catalyst for the fixed-bed-process, as the mostly used in the industry one (more than 50% of MA production [60]).

One should distinguish bulk and supported VPO catalysts. Although significant efforts were performed to synthesize a supported VPO catalyst [61], [62], [63], the selectivity of the synthesized samples is far from a bulk VPO catalyst and thus, supported VPO still cannot be considered as a suitable candidate for industry. Nevertheless, studies on supported VPO will be referred further in connection with searching of catalytically active species.

A bulk VPO catalyst is usually produced by activation of a catalyst precursor at reaction conditions for several hundred hours. The indication for the catalyst formation which is usually used in the preparation is formation of the dominant vanadyl pyrophosphate $(VO)_2P_2O_7$ phase monitored by XRD.

There are three well-established ways to prepare hemihydrate, which is the precursor for a VPO catalyst. In literature (see for example [64, 76]) they are referred to as ***VPA*** (aqueous route), ***VPO*** (alcoholic route) and ***VPD***. The first route, ***VPA*** involves preparation of the precursor by reduction of V_2O_5 in aqueous solution of HCl. In the second, ***VPO,*** route alcohol is used as a solvent and reductant of V_2O_5. This method is currently used for preparation of an industrial VPO catalyst. In the ***VPD*** method $VOPO_4 \cdot H_2O$ is first prepared from V_2O_5 and H_3PO_4 and then reduced using alcohol. These three preparation routes lead to catalysts with different surface areas and intrinsic catalytic performances. Additionally, there are two ways to improve catalytic performance and a surface area, i.e. doping of a catalyst by metal atoms (so-called promotion) and mechanotreatment of the precursor. Although all of these methods lead to different catalytic performances, it is believed that they influence the number and distribution of the active species, but not the nature of them. In other words, investigation of the nature of active species can be performed with a catalyst having a composition most suitable for the experimental method. The presence of metal dopants and alcohol molecules would complicate the *in situ* XPS investigation. This is why a catalyst prepared by the ***VPA*** route without promoters was chosen for *in situ* XPS studies.

4.2 Catalytically active species of a VPO catalyst. Literature review.

Vanadium oxides are widely used in catalysis thanks to the existence of a wide range of vanadium oxidation states and the ability of vanadium atoms to easily convert between them (so-called ***redox behavior***). This makes a vanadium atom a good center for accommodation and release of oxygen atoms during the catalytic cycle of oxidation, reduction and oxidative dehydrogenation reactions. Performance of a catalyst depends on several factors such as the structure and the morphology of the material, its redox properties and elemental composition. The right oxidation state and geometrical arrangement of the active species and whether they should be in the form of a certain crystalline phase or dispersed on the surface are the questions which are always discussed in connection with a vanadium oxide catalyst. Despite the long time of use of the VPO catalyst in industry and numerous investigations of the catalyst, still there is no agreement about the nature of the catalytically active species of the catalyst surface and about the reaction mechanism. Though a good literature review concerning searching of the active species of the VPO catalyst can be found in some works issued not a long time ago [65, 66, 67], some publishing activity in this field was observed since that time. In this chapter key works in this field will be briefly reviewed.

Various VPO phases are discussed in literature concerning *n*-butane oxidation (see for example [68], [69]). These are the phases with vanadium in 5+ oxidation state (for example, α-, β-, γ-$VOPO_4$), 4+ oxidation state (for example, $(VO)_2P_2O_7$) and 3+ oxidation state (for example, VPO_4). It is generally accepted that well crystallized vanadyl pyrophosphate $(VO)_2P_2O_7$ (which is a V^{4+} phase) is the major phase which is presented in an industrial VPO catalyst after a long operation time. Several groups suggested that the (100) crystalline plane of vanadyl pyrophosphate $(VO)_2P_2O_7$ is the most catalytically active VPO surface while other VPO phases are thought to be much less active or even detrimental for the activity of a sample [70, 71, 72]. T. Shimoda et al. [70] performed XRD, IR and XPS investigations of differently prepared VPO catalysts in order to estimate a responsible for MA formation crystalline phase. As a result the raw of catalyst selectivity was drawn: $(VO)_2P_2O_7 > X_2$, $X_1 >$ α-, β-$VOPO_4$, where X_1 and X_2 were some V^{5+} phases revealed by XRD. A selectivity of $(VO)_2P_2O_7$ was at least 50% higher than a selectivity of any other phase. V. Guliants et al. [71] have followed by ^{31}P NMR, XRD and Raman spectroscopy evolution with activation time of catalyst precursors prepared by different method. Correlation of a catalytic performance with a bulk composition of the catalysts determined by XRD allowed authors to conclude that a best catalyst contains

only highly crystalline vanadyl pyrophosphate. However, it was also concluded that XRD alone is not effective for identifying the presence of other minor phases. Coupling of XRD with two other techniques helped to identify $VOPO_4$ phases, which have V atoms in 5+ oxidation state, to be detrimental for a catalytic activity and vanadyl metaphosphate $VO(PO_3)_2$ to be inactive. Similar experiments enforced by electron microscopy were performed by the same group several years later [72]. It was observed that a disordered surface layer of ca. 2 nm thickness covering the (100) planes of $(VO)_2P_2O_7$ disappears with time on stream yielding a solid with a high steady-state catalytic performance. This led authors to the conclusion about responsibility of solely (100) planes of $(VO)_2P_2O_7$ for an activity and a selectivity of VPO catalyst. Nevertheless, *in situ* Raman spectroscopy in these experiments showed the appearance of $VOPO_4$ phases when the precursor was transformed to the active catalyst and the catalyst obtained at this moment contained only poorly crystalline $(VO)_2P_2O_7$ which was fully crystallized only after hundreds of hours under reaction conditions. This discrepancy was referred to the low activity and selectivity of the freshly prepared catalyst.

In situ electron microscopy and selected-area electron diffraction studies were performed by P.L. Gai and K. Kourtakis on VPO samples in various gas atmospheres at 400°C [5]. On the basis of the experimental data authors built a model of the defect formation mechanism during $(VO)_2P_2O_7$ reduction. The presence of a certain type of oxygen vacancies in $(VO)_2P_2O_7$ structure was concluded to be necessary for *n*-butane activation (hydrogen abstraction), i.e. vanadium atoms in an oxidation state lower than 4+ are necessary.

Other investigations indicate participation in the catalytic process of V^{5+} species in the form of $VOPO_4$ phases, surface insulated centers, surface and bulk crystalline defects [73, 74, 75, 76]. Importance of presence of both V^{4+} and V^{5+} in the active catalyst was stressed in these works. J.-C. Volta with colleagues showed in [73, 74] importance for the catalytic process of the presence of limited number of V^{5+} centers dispersed on the (100) $(VO)_2P_2O_7$ crystalline plane. Evolution of the precursor during the activation under reaction conditions was followed by *in situ* Raman and NMR spectroscopies supplemented by XRD and XPS. Bands corresponding to $VOPO_4$ and $(VO)_2P_2O_7$ appeared in Raman spectra simultaneously with beginning of MA production. Similar observation appeared in work [76] of G.J. Hutchings with colleagues. They investigated precursors prepared by the VPA, VPO and VPD methods by XRD and by *in situ* NMR and TEM. Nevertheless, authors recognize as the active centers the V^{4+}/V^{5+} couples dispersed on various VPO phases including $(VO)_2P_2O_7$. K. Aït-Lachgar et al. [75] oxidized pure and well-crystallized $(VO)_2P_2O_7$ in oxygen flow at 500°C for different times up to 24 hours. The samples were characterized by UV-VIS, XRD

and NMR. While an oxidation state value increased continuously, selectivity had a maximum value at an oxidation time of 1 hour. This led authors to the conclusion about existence of a proper for MA production density of V^{5+} species on top of $(VO)_2P_2O_7$.

Furthermore, Coulston et al. [77] correlated the time dependence of MA formation on the α_I-$VOPO_4/SiO_2$ and $(VO)_2P_2O_7/SiO_2$ samples with decay of V^{5+} species measured by time-resolved VK-edge XAS. Authors argued the central role of V^{5+} in the catalytic process and the responsibility of V^{4+} for by-product formation.

Such a wide range of opinions supported by experimental facts can be well explained by location of an active material in a topmost (1-2 nm) surface layer. This layer can hardly be investigated by the techniques used in the works mentioned above. Existence of such a layer on top of amorphous material or various crystalline phases was suggested by several experimental works. In [78] authors investigated exchange of gaseous and lattice oxygen using gaseous ^{18}O isotopes and a long-time operated (equilibrated) catalyst. Involvement of lattice oxygen in formation of MA and participation of the four topmost layers in oxygen exchange was concluded on the basis of the obtained time dependence of ^{18}O-balance in gas phase. Recent TEM investigations showed existence of a thin (about 1nm) amorphous layer on top of $(VO)_2P_2O_7$ for about 50 equilibrated VPO catalysts from different sources [79]. This layer was marked as a suitable candidate for localization of the active species. The authors nevertheless, failed to correlate the observations with a catalytic performance. This was accounted for the existence of other factors influencing the performance, such as the electronic structure. Figure 4-3 shows an example of a TEM image of such an amorphous layer.

Figure 4-3. HRTEM image of a VPO catalyst.
An amorphous layer of 2.5-4 nm thickness is clearly visible on top of a crystalline phase.
Details of the sample preparation and characterization are described in [64] (sample VPO_{P1}).

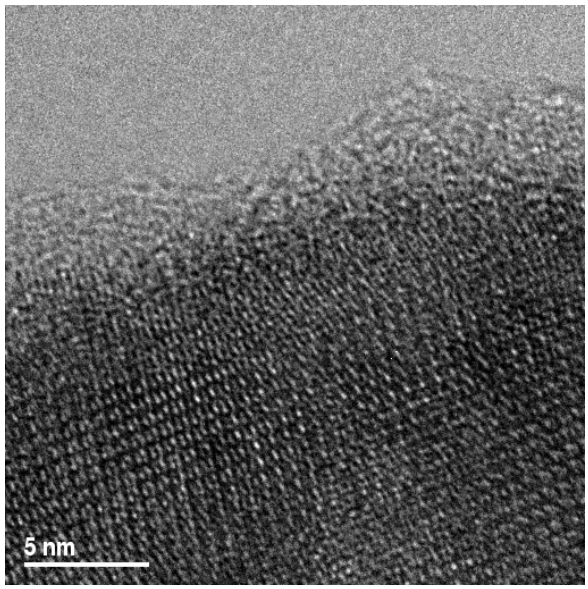

Additionally, some other observations [61, 76, 80] can be viewed as indirect proof of the presence of a thin active layer on top of a bulk phase. M. Ruitenbeek et al. [61] investigated bulk and supported VPO. The sample with SiO_2 support was found to have a catalytic activity equal to the activity of the bulk VPO sample. An EXAFS spectrum, however, showed the amorphous nature of SiO_2-supported VPO, while bulk VPO had the structure of well-crystalline $(VO)_2P_2O_7$. This led the authors to conclusion that the oxidation of n-butane takes place over an amorphous VPO surface. Furthermore, a completely amorphous VPO catalyst was synthesized using supercritical CO_2 [80]. The amorphous nature of the catalyst was concluded from NMR, XRD, electron diffraction and HREM measurements. For this catalyst no activation was necessary to reach full catalytic performance. The catalyst showed a better intrinsic catalytic activity towards MA comparing samples prepared by VPA, VPO and VPD route. In addition, no crystallization of the catalysts material was observed during the reaction, which is in contradiction to the observations of material crystallization with time on stream for catalysts prepared by the standard procedures (VPA, VPO and VPD). In the same paper the authors argue about different structure of the surface layer and of the bulk on base of some experimental observations. Among them are:

1) XPS consistently shows phosphorous enrichment on the surface.
2) Catalysts prepared by different methods gave very different relative amounts of the $(VO)_2P_2O_7$ and $VOPO_4$ phases, but have very similar activities for MA production.

3) EXAFS measurements give bond lengths which do not fit to the geometric structure of $(VO)_2P_2O_7$ obtained by XRD

In situ NEXAFS measurements performed on the amorphous catalyst in this work showed evidence of *in situ* formation of the active surface layer. In work [76] G. Hutchings with colleagues report preparation of VPO catalysts by three different methods. The samples showed a similar intrinsic activity to MA, but had different bulk phase compositions. This observation also indicates that the surface layer and the bulk do not necessarily consist of the same phase.

As it was demonstrated by our previous *in situ* NEXAFS studies, the electronic structure of the VPO surface is very sensitive to reaction conditions [81, 82]. In [81] a catalyst prepared by the aqueous route was investigated under different reaction conditions. V L_3-edge features were correlated with MA yield. Both showed reversible changes with reaction conditions, which allowed us to conclude a dynamic nature of the surface structure, those catalytically active state forms under reaction conditions. These observations led us to the conclusion that receiving of right information about the active species requires application of a surface sensitive method under reaction conditions (*in situ*).

A phosphor/vanadium (P/V) stoichiometric ratio of the active VPO surface is a separate topic, which was widely discussed in literature. It is generally known that this stoichiometic ratio is an important parameter in preparation of a VPO catalyst. Many authors also believe that a surface P/V ratio does not necessarily match the bulk ratio and its value has an essential influence on a catalytic performance of the catalyst [83, 84, 85, 86]. The industrial process to obtain MA from *n*-butane includes the addition of phosphor-containing compounds in raw gases to compensate for a loss of phosphor by the catalyst and consequently, to prevent the deactivation.

In [83, 85] a surface P/V ratio slightly higher than 1 was concluded on the base of XPS measurements to be the optimum ratio. P/V values less than 1 were recognized as detrimental for selectivity towards MA. Furthermore, in [86] authors presented a depth profile of P/V ratio in the optimal VPO catalyst. According to this profile a ratio should be about 6 in the topmost crystalline layer and it should decrease to the bulk value of 1 within the first 2 nanometers. The data were obtained by combination of SIMS with depth profiling by Ar sputtering. Nevertheless, in work [87] a catalyst demonstrated almost no change in P/V ratio determined by XPS with time on stream. At the same time *n*-butane conversion had increased from 22 to 65% and selectivity towards MA raised from 34 to 69%. This experimental fact clearly shows that P/V ratio alone does not serve as a predictor of catalyst performance. Most

experimental works gave a P/V ratio higher than 1 for a well-active and selective VPO catalyst. Estimated P/V values range from close to 1 [85] up to 3 [88] and sometimes even higher, while a bulk P/V ratio is always close to 1. Various hypotheses exist in literature about the role of phosphor enrichment on the surface. Some authors suggest the active site insulation role of phosphor atoms [89], [90], [91]. According the hypothesis of site insulation lattice oxygen atoms on the active surface of a VPO catalyst are arranged in domains, which are fully insulated from each other by surface phosphor [89]. It is stated that only such a distribution of oxygen atoms is inherent to a selective VPO catalyst and absence of the insulation or insulation of single oxygen atoms would lead to loss of selectivity [90]. Other authors assign to phosphor the property of prevention of overoxidation of vanadium atoms [84], [92]. It can be also assumed that the presence of phosphor is necessary to set the right distance between two vanadium atoms to accommodate *n*-butane molecules and reaction intermediates [93]. Presence of V vacancies on the surface was also suggested [94], which can explain the high P/V ratio values. Nevertheless, the speculations should be taken with caution because they are mostly based on XPS and LEIS experimental data. These methods were shown to give in some cases a wrong P/V ratio because of two possible reasons. The *first reason* is deviation of XPS sensitivity factors from their true values. These sensitivity factors are used to calculate stoichiometric ratios from XPS peak area ratios. Coulston et. al [25] performed XPS measurements of organometallic reference compounds containing phosphor and vanadium. The sensitivity factors based on theoretical calculations [95], which are commonly used in XPS for P/V ratio estimation, were shown to be wrong by factor of two for these measurements. T. Okuhara and M. Misono [83] have also used reference compounds (phosphor-vanadium containing glasses) and obtained P/V values slightly above unity for well-active and selective VPO catalysts. The *second possible reason* is the preferential masking of surface vanadium atoms by carbon or hydrocarbons, which leads to a decrease of the V signal in XPS and LEIS experiments. Existence of this effect was demonstrated by W. Jansen with colleagues [96]. They measured by LEIS a P/V surface ratio of a VPO catalyst with the bulk ratio of 1.1. The measurements were done before and after high-temperature treatment in oxygen and hydrogen. The surface after the oxygen treatment was supposed to be clean, while an oxidation state measured by XPS had not changed significantly. A P/V ratio after the oxygen treatment was found to be 2.0 comparing 2.9 before the treatment. After consequent hydrogen treatment a P/V value increased to 3.6. In view of all mentioned in this paragraph it became clear that the value of a surface P/V ratio of an active VPO catalyst is still a question under discussion.

Because of a wide range of opinions concerning the active species of a VPO catalyst, an investigation of the nature of the catalytically active surface would have big practical importance. Next chapters are devoted to experimental details and results of the investigation of VPO catalysts by the XPS technique under reaction conditions.

4.3 Sample preparation and characterization

The VPO samples were prepared by the group of Prof. Hutchings from Cardiff University and characterized by several groups as it was discussed in detail in [64]. I denoted the samples as "sample-1" and "sample-2", which corresponds to the notations in the paper "VPO_{P9}" and "VPO_{P4}" respectively. A brief description of a preparation procedure and of characterization results is given in Table 4-1.

Table 4-1. Sample preparation, catalytic selectivity and BET surface area.

Sample	Raw material	Preparation	Selectivity to MA*	BET, m^2/g
sample 1 (VPO_{P9})	V_2O_4, H_3PO_4, H_2O	Heated (145°C, 72 h), washed, dried, activated*	57%	11
sample 2 (VPO_{P4})	V_2O_5, $H_4P_2O_7$, H_3PO_4, H_2O	-//-, refluxed in water, activated*	51%	23

* in a laboratory microreactor in the mixture of 1.7% *n*-butane in air at 400°C, 1 bar

The samples were prepared by aqueous rout using H_3PO_4 and $H_4P_2O_7$ as reducing agent instead of widely used HCl. The precursor for the sample-1 was prepared from V_2O_4 (5. 9g), H_3PO_4 (6.7 g) and distilled water (20 ml). The mixture was heated in an autoclave (145°C, 72 h), then washed with cold distilled water (50ml) and dried in air (120°C, 16 h). The precursor of sample-2 was prepared using V_2O_5 (5.9 g), $H_4P_2O_7$ (1.703 g), H_3PO_3 (4.1 g) and distilled water (20 ml) in the same way as sample-1, with subsequent reflux in distilled water (20 ml·(g solid)$^{-1}$) for 2 h. Both precursors were found by XRD and Raman spectroscopy to have the $VOHPO_4{\cdot}0.5H_2O$ structure, which is the normal structure for VPO catalyst precursor. The activation was performed in a laboratory microreactor in the mixture of 1.7% n-butane in air at 400°C. After the activation the samples were characterized by XRD, NMR and HREM. The sample-1 appeared to have mainly the $(VO)_2P_2O_7$ phase, while the sample-2 was mainly α_{II}-$VOPO_4$ with admixture of $(VO)_2P_2O_7$.

After testing the catalytic performance, the catalyst powder (50 mg) was pressed into pellets of 13 mm diameter using the pressure of 10 MPa in order to perform *in situ* XPS measurements on these samples. A separate experiment showed that pressing at such conditions does not change a relative BET area of VPO catalysts.

4.4 Experimental conditions

The experimental investigations were performed on the *in situ* XPS setup described in detail in sections 3.3 and 3.5.

The experiments were performed at the beamline U49/2-PGM1 [97] at the synchrotron BESSY-II [98] in Berlin. An overall spectral resolution of the system was evaluated from the Ar $2p_{3/2}$ gas phase peak and was found to be better than 0.3 eV at the photon energy of 700 eV. The pressure for the reaction gas mixture in our experiments was set to 2 mbar. At this pressure it was still possible to get spectra with good signal to noise ratio. The samples were investigated in a constant gas flow of 1.5% *n*-butane in He (partial pressure 1.6 mbar) and oxygen (partial pressure 0.4 mbar).

The aim of the investigation was to observe a difference in the electronic structure of the catalysts in the catalytically active and inactive states. Change of the catalyst state was performed by change of a temperature. The usual temperature of the catalyst to operate the reaction of oxidation of *n*-butane to MA is 400°C. Consequently, this temperature was chosen to investigate properties of the catalyst in the catalytically active state. At room temperature the catalyst is known to be practically inactive. Unfortunately, VPO was highly charged at room temperature during *in situ* XPS experiments in the reaction mixture. The charging broadens XPS peaks and consequently, makes analysis of their shape difficult or not possible at all. Usually charging in high-pressure XPS experiments is reduced relative to vacuum conditions because of charge transfer by electrons extracted by the X-ray beam from gas phase. Nevertheless, in the case of VPO samples the presence of the ions is obviously not enough to compensate the charging effect and the use of standard methods of charge compensation (such as an electron flood gun) is not possible in gas atmosphere. Fortunately, as it was shown by our preliminary studies [81] a charging decreasing with temperature and practically disappearing at some temperature not higher than 250°C. This fact can be explained by an increase in electrical conductivity with temperature, which is inherent for semiconductors and by changing the conductivity because of changes in the electronic structure. The temperature offset of MA formation is well above 250°C and the catalyst state can be considered as inactive at the temperature of charging disappearance. Therefore, spectroscopic measurements were done at temperatures of 150-200°C, where a MA yield was negligible, and at 400°C, which is the usual reaction temperature. Additionally, change with time of the electronic structure of the samples was observed while they were kept in absence

of oxygen (in 1.6 mbar of 1.5% n-butane in He) at 400°C to investigate sample stability towards reducing conditions.

In the described XPS experiments the O1s/V2p, C1s, P2p core-levels and the valence band region were recorded. An incident photon energy was varied in such a way that a kinetic energy of the photoelectrons was constant for all recorded XPS regions, thus, providing for a uniform information depth, a constant contribution of the analyzer transmission function as well as a constant contribution of gas phase scattering. Additionally, depth-profiling by varying the excitation photon energy applied to the same core-level was performed, which leads to a change of photoelectron kinetic energy and as a consequence, to a change in information depth. The values of excitation energy and corresponding information depths, estimated using the "universal curve" [3] (Figure 3-4), are presented in Table 4-2.

Table 4-2. Experimental conditions: excitation energies and information depth for O1s-V2p and P2p XPS regions.

Photoelectron kinetic energy, eV	Excitation energy, eV				Information depth [3]**, nm.
	O1s-V2p	P2p	C1s	VB	
200	730	335	485		1.0
330	860	465	615		1.3
720	1254*	854	1005	730	1.8
1240				1254	2.3

* The photon energy of 1254 eV corresponds to MgKa line, which is in common use in laboratory XPS systems for chemical analysis (ESCA).

** An inelastic mean free path of electrons was calculated in [3] in terms of monolayers on base of experimental data for crystals with a thickness of monolayer of about a mean interatomic distance. To calculate an information depth for VPO, the monolayer thickness was chosen to be equal to the mean interatomic distance for oxygen atoms in $(VO)_2P_2O_7$, which is about 0.3-0.4 nm [99].

4.5 Sample activity during *in situ* XPS measurements.

The catalytic reactivity of the samples was measured by proton-transfer-reaction-mass-spectroscopy (PTRMS). A conventional quadrupole MS was found to be not sensitive enough to detect a small amount of MA produced at our experimental conditions.

Protonated MA molecules produce signal at m/e=99 amu per electron charge. The signal is measured in units of concentration of the selected mass inside the PTRMS. The concentration is different from the concentration in the sample cell because investigated gas was compressed and diluted with air. Nevertheless, relative concentrations are suitable for comparison. Mass spectra were recorded simultaneously with XPS measurements, which allow correlation of XPS results with catalytic activity of the material. MA signal in PTRMS, showed the exponential time behavior with a time-constant of about 10 min, which results from accumulation of products in the pumping system.

The mass-spectra are shown on Figure 4-4 and Figure 4-5.

Figure 4-4. Maleic anhydride yield during *in situ* XPS experiments with the sample-1
In the reaction mixture and in *n*-butane/He atmosphere. The points, where XPS spectra were recorded, are marked by arrows and letters.

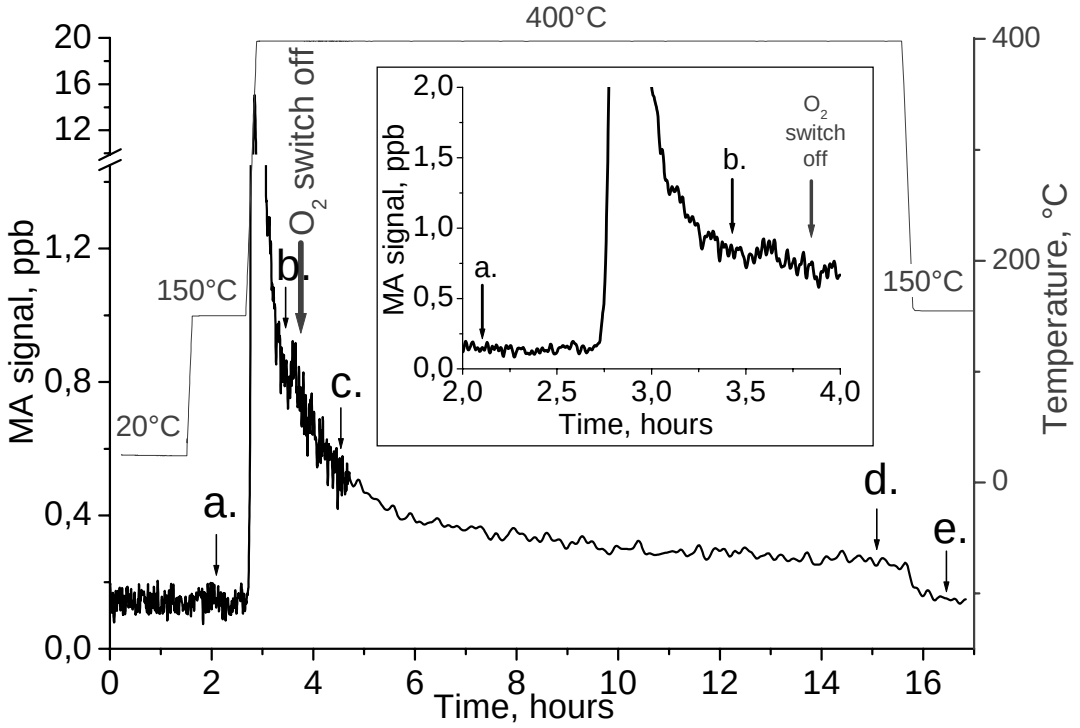

Figure 4-5. Maleic anhydride yield during *in situ* XPS experiments with the sample-2
a) in the reaction mixture, first heating, b) second heating, c) third heating and switching to *n*-butane/He atmosphere. The points, where XPS spectra were recorded, are marked by arrows and letters.

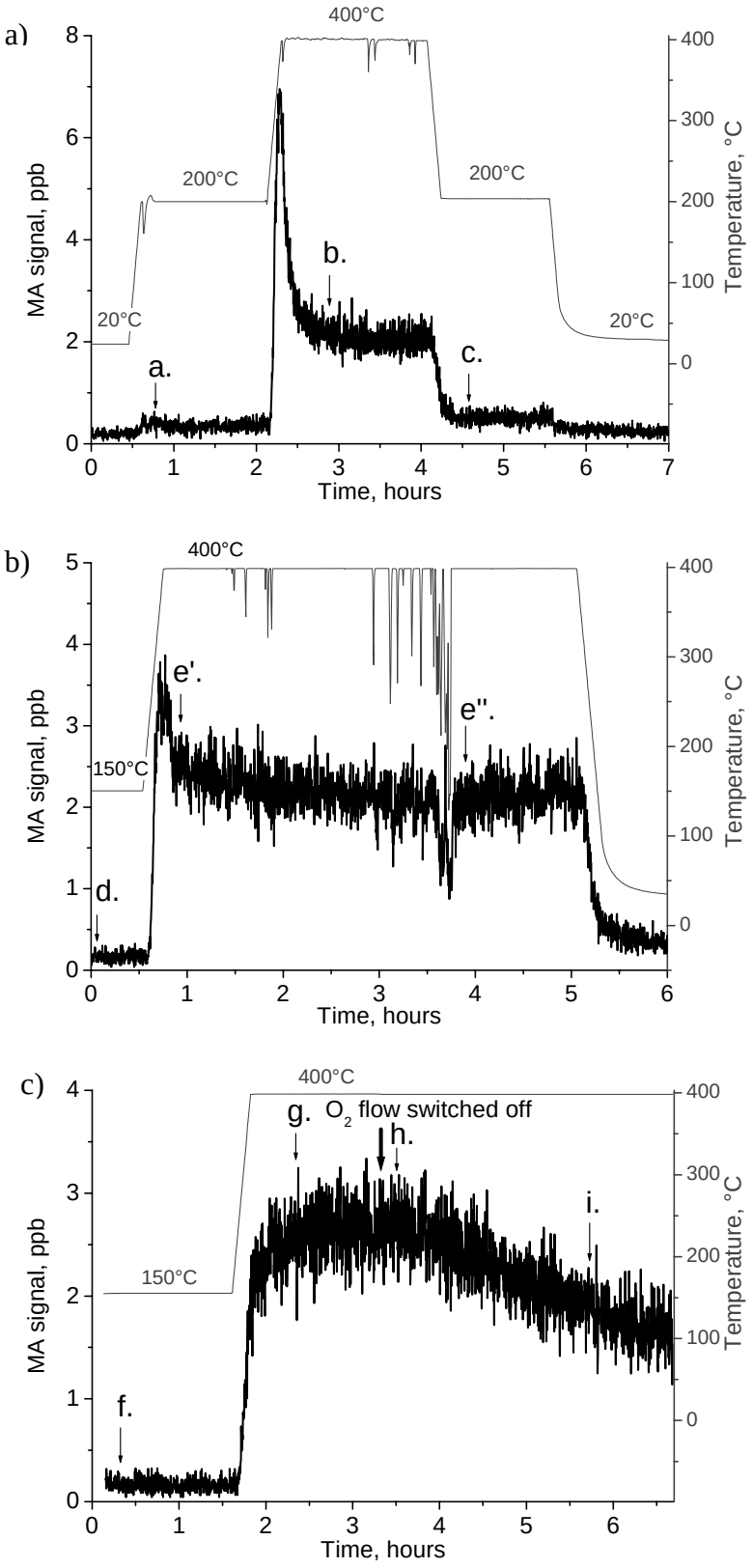

The signal-to-noise ratio in the spectrum on Figure 4-4 changed during the measurements because a dwell time of the mass-spectrometer was increased in order to limit the size of the data file in the region where no fast time response is necessary. No significant increase in a MA signal was observed after heating the samples to 200°C. When the samples were heated to 400°C with the heating ramp of 20°C/min (Figure 4-4, Figure 4-5 a), the peak in the MA signal followed by decrease to a constant level after less than one hour was observed. It can be clearly seen that MA could be detected for both catalysts at 400°C and practically no MA was detectable after cooling down to temperatures lower than 200°C. Heating tests with the same reaction mixture in absence of a sample in the chamber did not show any production of MA, which allows to relate the catalytic activity to VPO material. For sample-2 the temperature was cycled 3 times between 150 or 200°C and 400°C (see Figure 4-5). A steady-state level of the MA yield at 400°C was found to be the same in all three cycles, which indicates that MA is a product of the catalytic reaction but not of an unsteady-state process. An amplitude of the initial peak of MA signal in PTRMS was significantly lower during the second heating cycle (see Figure 4-5 b), and no peak was visible during the third cycle (Figure 4-5 c). The behavior of this peak clearly shows that the peak is caused by desorption of MA, which was produced during activation of the catalyst in a microreactor in a reaction mixture at 1 bar before the *in situ* XPS experiments. The same behavior was observed for a VPO catalyst in our *in situ* XAS experiments [81]. The absence of a desorption peak during the third heating cycle does not indicate the absence of adsorbed MA molecules but rather, a lack of sensitivity of our system to register a desorption of a small amount of MA attached to the surface at the low-pressure conditions. A steady-state MA yield in the reaction gas mixture at 400°C was (2.6±0.7) times higher for the sample-2 as compared to the sample-1. After normalization to the BET surface area (11 and 23 m^2g^{-1} for the sample-1 and sample-2, respectively. See Table 4-1) the ratio of normalized yields was obtained to be (1.2±0.3), which indicates that both samples have nearly the same intrinsic activity to MA.

Reduction of the samples in *n*-butane/He atmosphere (see Figure 4-4 a, Figure 4-5 c and Figure 4-6) led to significantly different deactivation time behavior. Fit of a MA yield time behavior in n-butane/He with a first order exponential decay function gave the time constants of 0.9 and 6.4h for the sample-1 and sample-2, respectively (Figure 4-6).

Figure 4-6. Time dependence of normalized MA yield in *n*-butane/He atmosphere at 400°C.

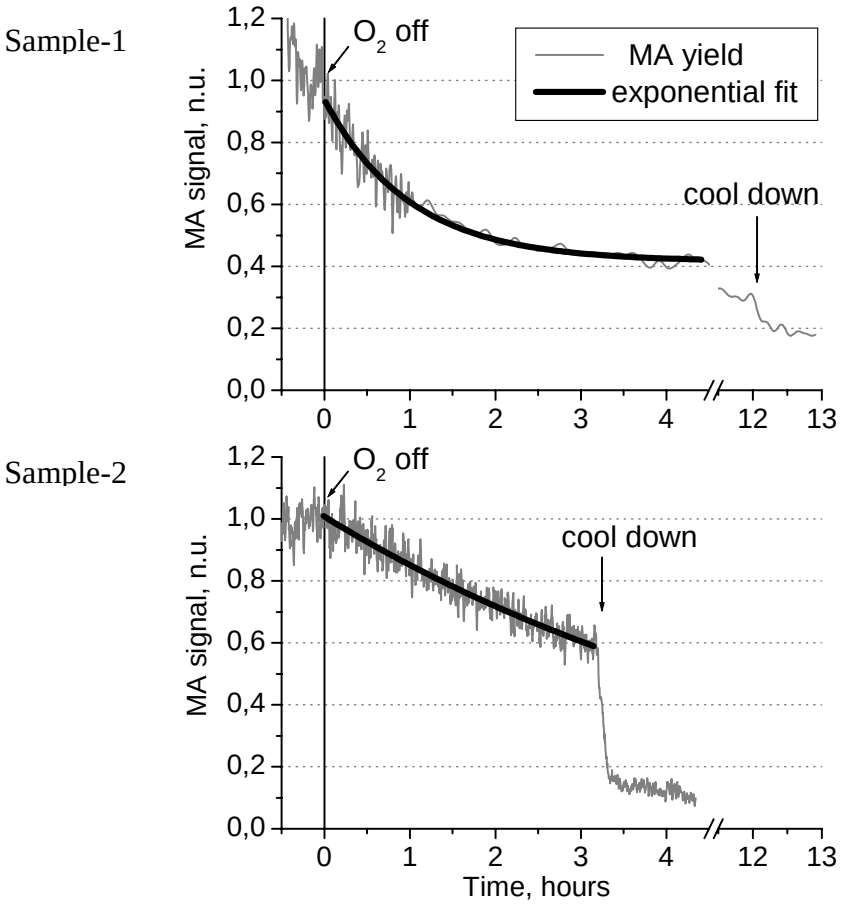

4.6 XPS data.

A typical XPS spectrum of a VPO compound is shown on Figure 4-7.

Figure 4-7. Typical survey photoelectron spectrum of VPO.
Sample-2, 400°C, reaction mixture (p=2 mbar), hv=1254 eV.

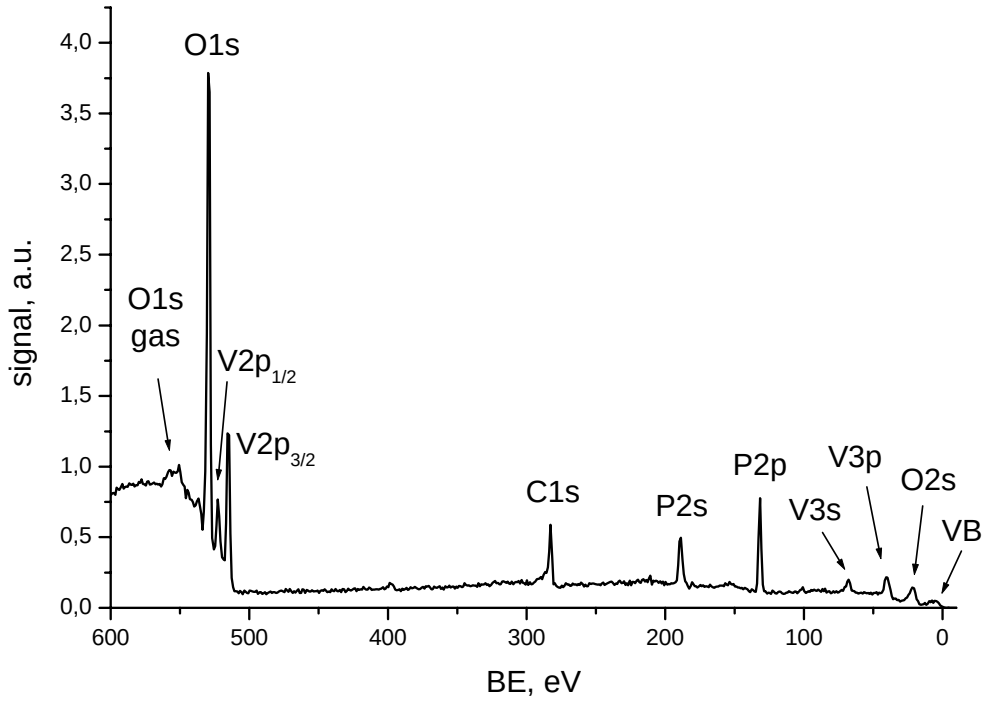

The assignment of XPS peaks was made according [22, 100]. Most intense peaks, corresponding to V, P, O and C elements, were recorded separately with small KE step in order to extract information about a chemical state and stoichiometry. The peak at BE of 530 eV corresponds to photoelectrons emitted from the O1s core-level. The broadened doublet at 550-555 eV is the O1s photoelectron peak of gas phase oxygen molecules. Broadening of this peak changes with sample charging and with sample position. In some spectra it became so broad that it was not possible to recognize it anymore. The doublet with binding energies of about 515 and 522 eV corresponds to electrons from the V2p level having the total angular momenta j=3/2 and 1/2 respectively. The C1s and P2s peaks are around 285 and 190 eV respectively. P2p have a form of one broad peak around 135 eV because the doublet components (j=1/2 and 3/2) are not resolved in the spectrum because they have a BE difference of about 1 eV. V3s is around 67 eV. The V3p doublet is also not resolved and has a BE of about 40 eV. O2s peak is around 20 eV. The valence band is composed from oxygen, vanadium, phosphor and carbon valence orbitals.

Evolution of the peaks during the experiment is presented on Figure 4-10 - Figure 4-19 and Figure 4-20 - Figure 4-21. Every region was recorded with two different excitation energies, corresponding to the most surface and the most bulk sensitive modes (see Table 4-2 on page 30). The spectra in the bulk sensitive mode were taken with the excitation energy corresponding to the photoelectron kinetic energy 720 eV (spectra ***B.***). The kinetic energy of 200 eV was chosen for most of the spectra in the surface sensitive mode (spectra ***S.***). Several O1s and V2p spectra were recorded with the photoelectron kinetic energy of 330 eV (Figure 4-11-S, Figure 4-13-S, Figure 4-15-S) to obtain good-quality spectra at low temperature. An information depth for these spectra is a little bit different as compared with the spectra taken with KE~200 eV. Nevertheless, as it will be shown further, no remarkable gradient of oxidation state was observed for the sample-2 and consequently, the spectra can be related to the surface sensitive mode just as well as the spectra with KE~200 eV. The valence band region was recorded in the bulk sensitive mode with KE~720 eV (Figure 4-20-B and Figure 4-21-B) because a spectral intensity of the excitation source around hv=200 eV does not allow to record the region with a reasonable quality. Additionally, the VB region was recorded with the photoelectron kinetic energy of 1250 eV (Figure 4-20-D and Figure 4-21-D) to observe possible spectral changes with information depth.

The O1s, V2p (Figure 4-8) and VB (Figure 4-9) peaks of V_2O_5 and reduced V_2O_5 were recorded as reference spectra for VPO.

Figure 4-8. O1s and V2p$_{3/2}$ XP spectra of V_2O_5 (001).
The sample was reduced in 10^{-3} mbar of oxygen at 350°C.

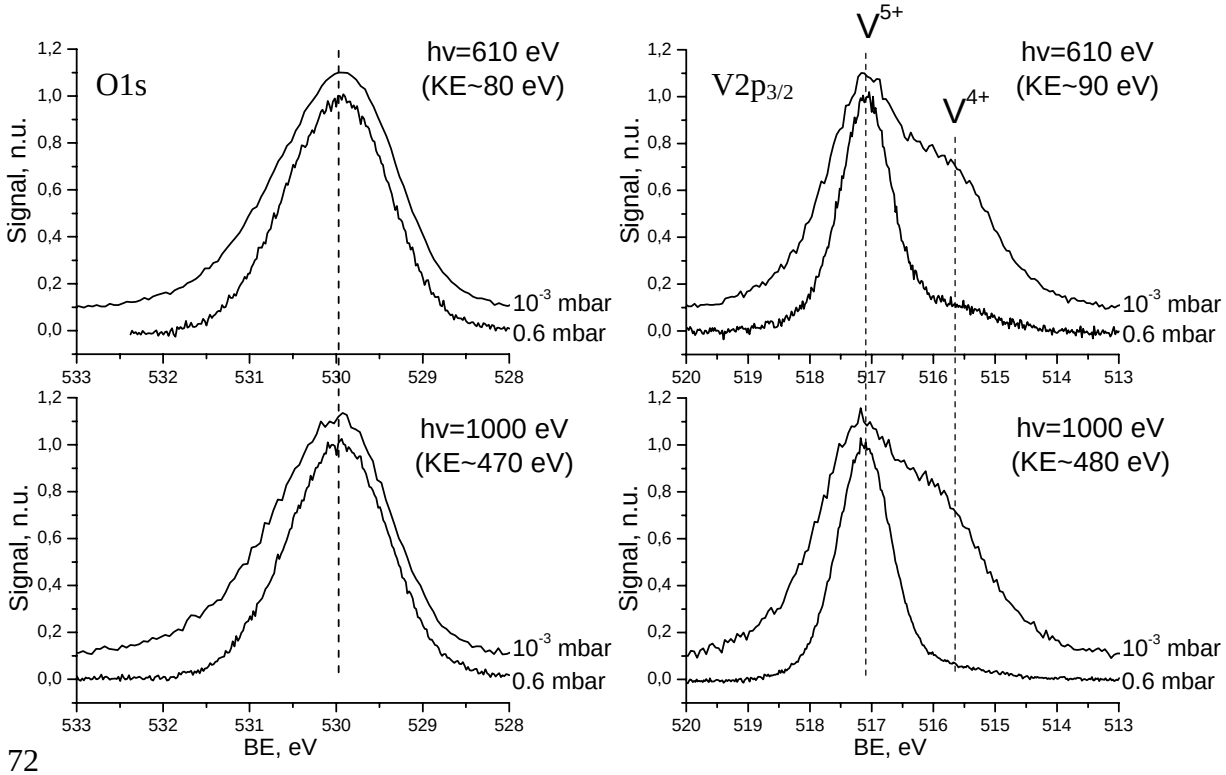

Figure 4-9. VB XP spectra of V_2O_5 (001).
The sample was reduced in 10^{-3} mbar of oxygen at 350°C.

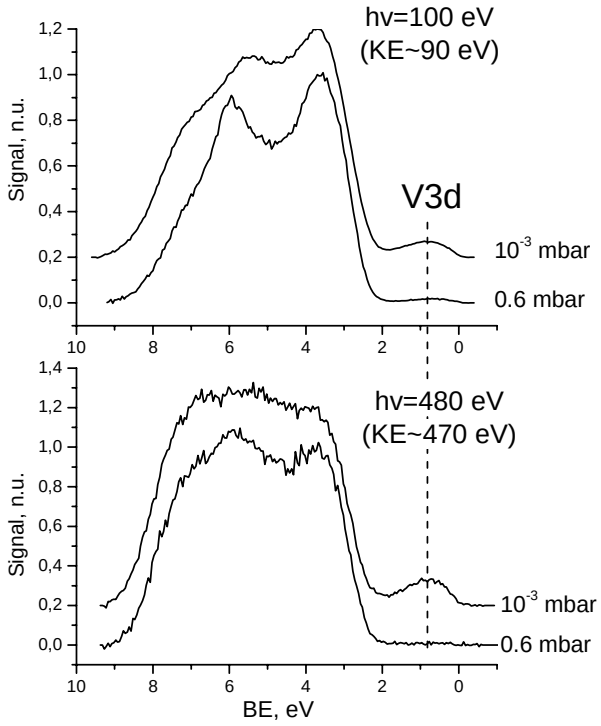

Spectra of the O1s-V2p regions on Figure 4-10 and Figure 4-11 and of valence band on Figure 4-20 and Figure 4-21 are shown "as is" without background subtraction but after normalization of the peak amplitude to unity. Other spectra on Figure 4-12 - Figure 4-19 were subjected to subtraction of a Shirley-type background and normalization to unity. Calibration of BE scale is a difficult task, which in our case should be performed separately for every region. BE scale of an O1s-V2p region was calibrated to the position of the maximum of an O1s peak at 530 eV. This value is inherent to binary vanadium oxides [22]. Nevertheless, the choice of this binding energy for the O1s peak of VPO is somewhat arbitrary and was performed solely because there is no agreement in literature about the right BE of this peak (see for example Table 1 in Ref. [101]). The C1s and P2p peaks were calibrated to the positions of their maxima, which are 285 and 135 eV respectively. BE scale of the VB region was calibrated to the low-BE threshold of the small low-energy-side peak. This peak was assigned to the V3d states and the threshold corresponds to FE.

The shape and a BE position of an XPS peak gives in principle information about the chemical state of an element. Nevertheless, shifting and broadening of the peaks because of charging and overlapping of spectral features sometimes make very complicated or not possible at all extraction of firm data from a spectrum. Below the principle possibilities to obtain information about chemical states of elements on the basis of XPS data received during our experiment will be discussed.

Figure 4-10 and Figure 4-11 show the O1s-V2p region "as it is".

Figure 4-10. Evolution of the O1s-V2p region of the sample-1.
Sample activity during the experiment is shown on Figure 4-4.

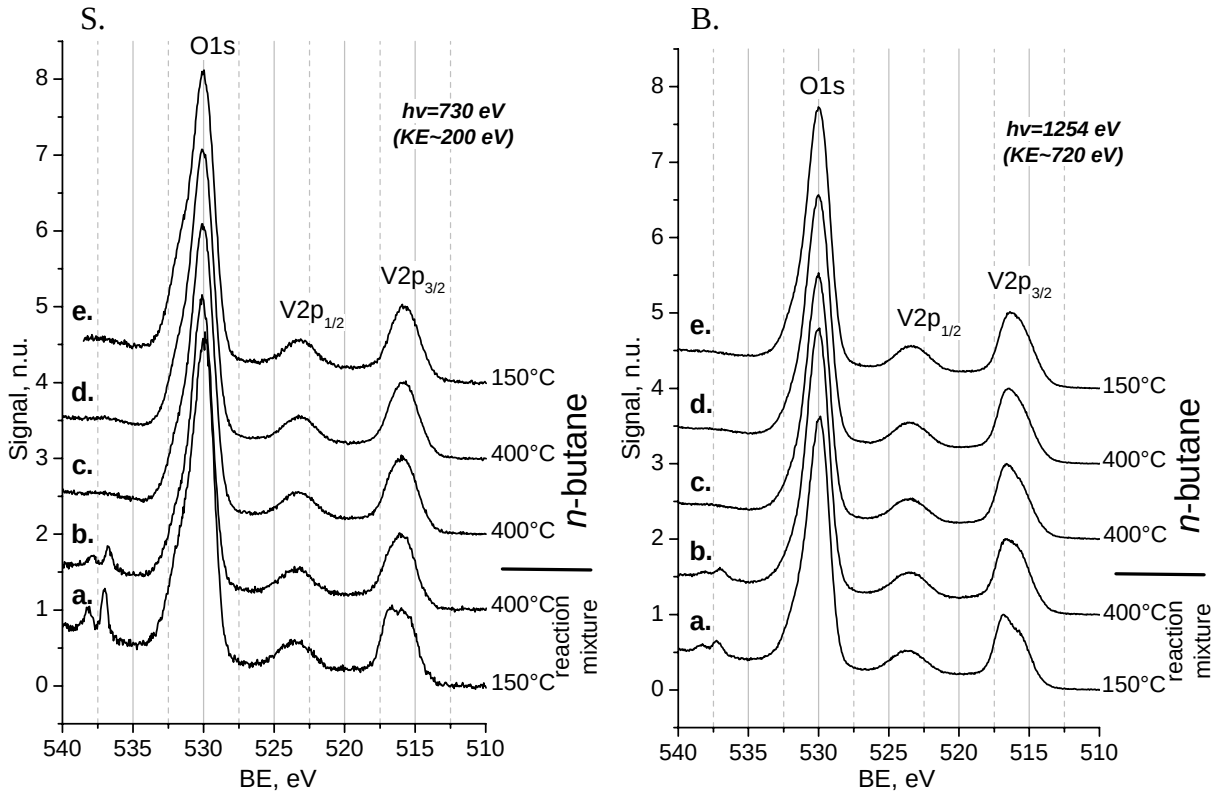

Figure 4-11. Evolution of the O1s-V2p region of the sample-2.
Sample activity during the experiment is shown on Figure 4-5-(a-c).

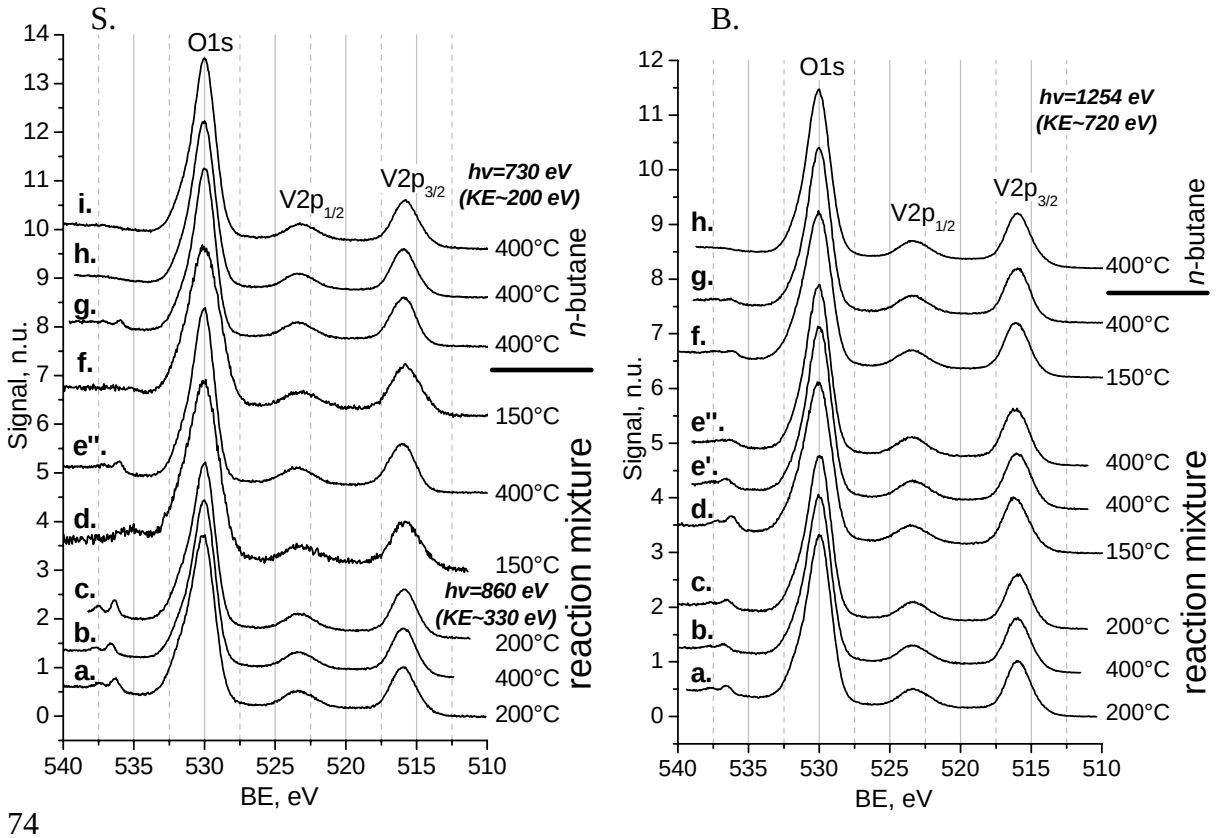

BE scale of the region was calibrated to the position of the maximum of the O1s peak at 530.0 eV. The O1s regions after Shirley background subtraction are shown on Figure 4-12 and Figure 4-13.

Figure 4-12. Evolution of the O1s peak of the sample-1.
Sample activity during the experiment is shown on Figure 4-4.

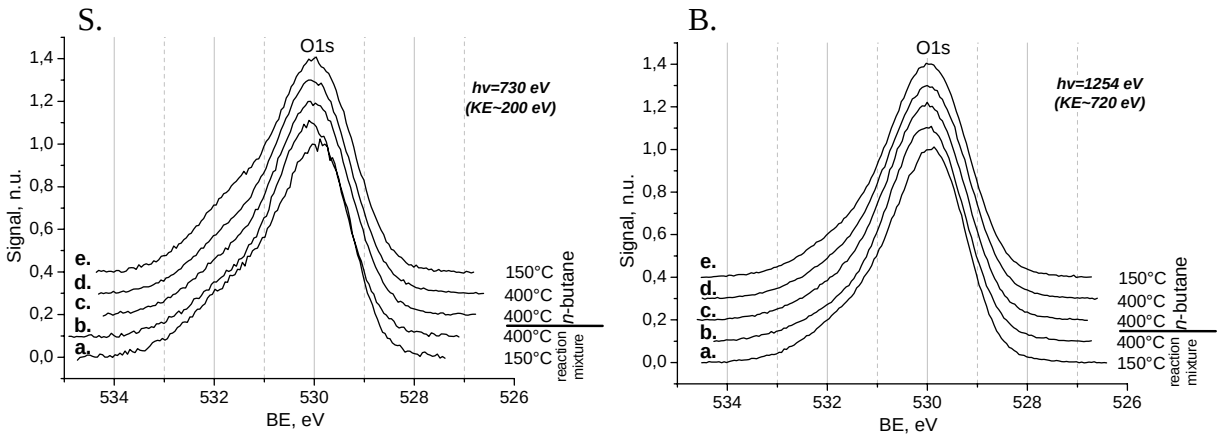

Figure 4-13. Evolution of the O1s peak of the sample-2.
Sample activity during the experiment is shown on Figure 4-5-(a-c).

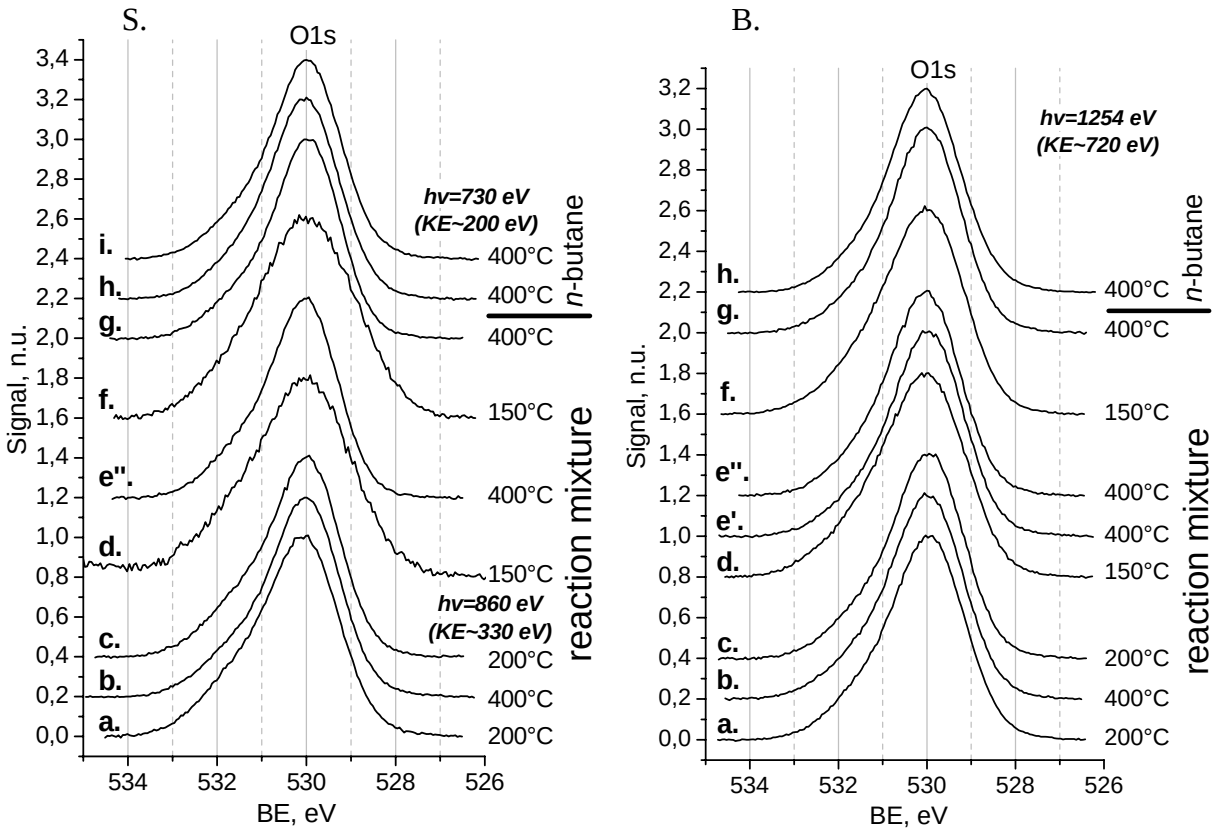

As it was already discussed in part 4.2 the bulk phase of an industrial VPO catalyst is $(VO)_2P_2O_7$. The structure of this phase ([102] and references therein) is built by VO_6 octahedra and PO_4 tetrahedra. Therefore, there are three types of oxygen: singly coordinated (V=O, P=O), doubly coordinated (V-O-P, V-O-V, P-O-P) and triply coordinated (to two V and one P atom) [103]. Other VPO structures or amorphous phases should contain the same types of oxygen atoms, perhaps with different bond lengths. One should also take into account various types of carbon-oxygen-containing adsorbates which are present on the surface. A BE of O1s electrons in V-O-V atoms can be estimated from data for binary vanadium oxides. Various vanadium oxides have an O1s peak at almost the same BE of 530.0 eV (±0.5 eV) [22]. A BE about 532.5 eV for the O1s level of P-O-P oxygen atoms can be obtained from bridging oxygen atoms of P_2O_5 [22]. From the same compound one can estimate a BE of about 534 eV for P=O oxygen. A BE of V-O-P O1s component should than be between 530.0 and 532.5 eV, which are the values corresponding to V-O-V and P-O-P oxygen atoms. From general considerations, the triply coordinated oxygen should contribute the O1s peak at lower BE than that of V-O-V oxygen, and this contribution should be smaller than the contribution of V-O-V oxygen. The O1s component of oxygen bonded to carbon should appear around 533-534 eV ([104], page 469). Therefore, from the possible kinds of oxygen atoms V-O-V should have a lowest BE of O1s electrons and it is reasonable to assign the main peak of the experimental O1s spectra (Figure 4-12 and Figure 4-13) to this kind of oxygen. The position of this peak was artificially set to 530.0 eV to calibrate BE scale of O1s-V2p spectra. The high-energy wing of the O1s peak should be than formed by other oxygen species. Although the O1s peaks showed some changes around 531.5-532 eV, the effect was too small to relate these changes to an alternation of a relative amount of certain oxygen species.

$V2p_{3/2}$ region is shown on Figure 4-14 and Figure 4-15.

Figure 4-14. Evolution of the $V2p_{3/2}$ peak of the sample-1.
Sample activity during the experiment is shown on Figure 4-4.

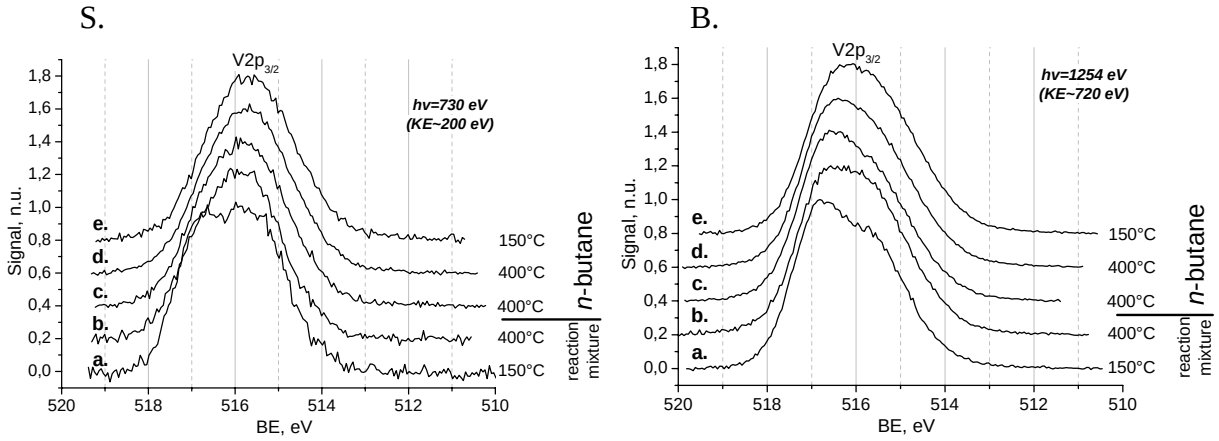

Figure 4-15. Evolution of the $V2p_{3/2}$ peak of the sample-2.
Sample activity during the experiment is shown on Figure 4-5-(a-c).

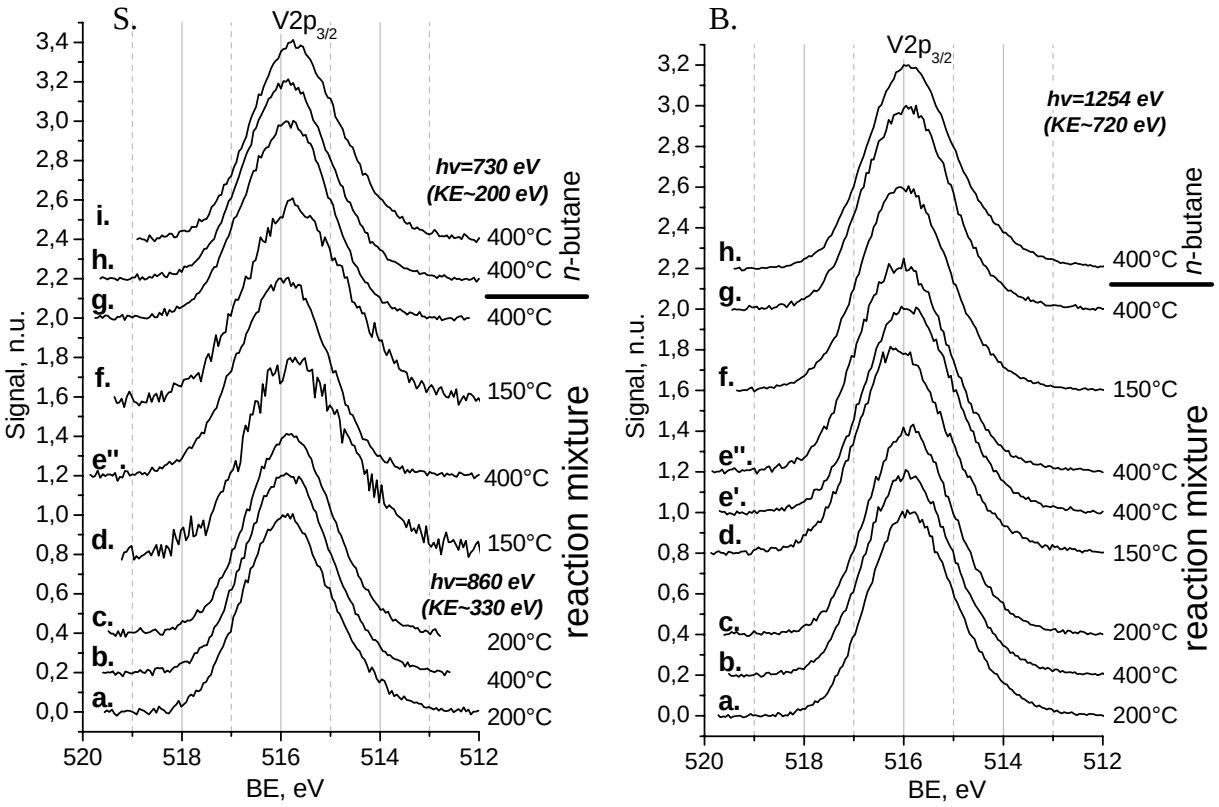

As it is well-known from literature ([105], [106], [107]) the shape of the $V2p_{3/2}$-peak contains information about an oxidation state of vanadium atoms. Contributions to the spectra from vanadium atoms in different oxidation states were found at binding energies different

enough to distinguish these contributions and extract information about a mean oxidation state. Different literature sources refer to different values of BE of single-oxidation-state components (see chapter 4.7). The BE of V^{5+}-component was determined to be in the region from 516.9 to 517.2 eV, the V^{4+} component is between 515.7 and 516.2 eV and the broad V^{3+}component with a width of ca. 4 eV has a maximum at about 515.5 eV. The procedure and results of oxidation state determination will be discussed in chapter 4.7.

The P2p peak is shown on Figure 4-16 and Figure 4-17.

Figure 4-16. Evolution of the P2p peak of the sample-1.
Sample activity during the experiment is shown on Figure 4-4.

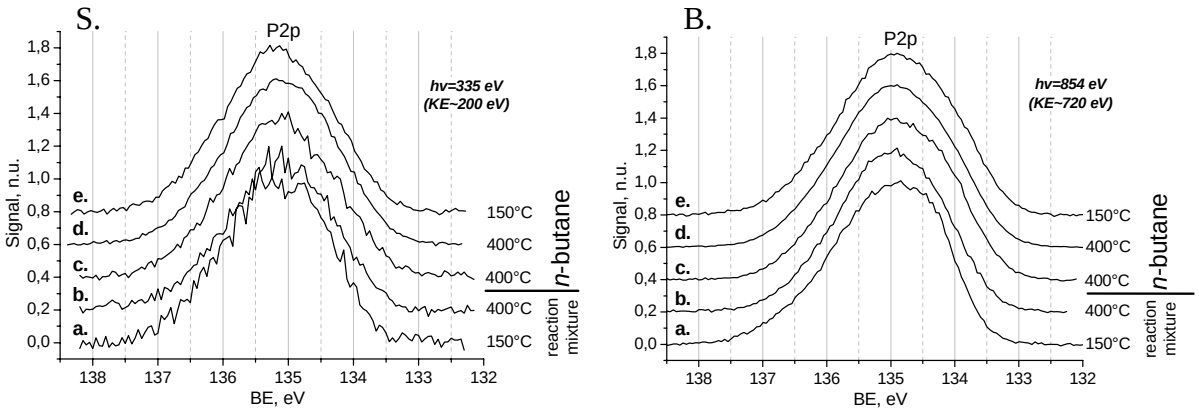

Figure 4-17. Evolution of the P2p peak of the sample-2.
Sample activity during the experiment is shown on Figure 4-5-(a-c).

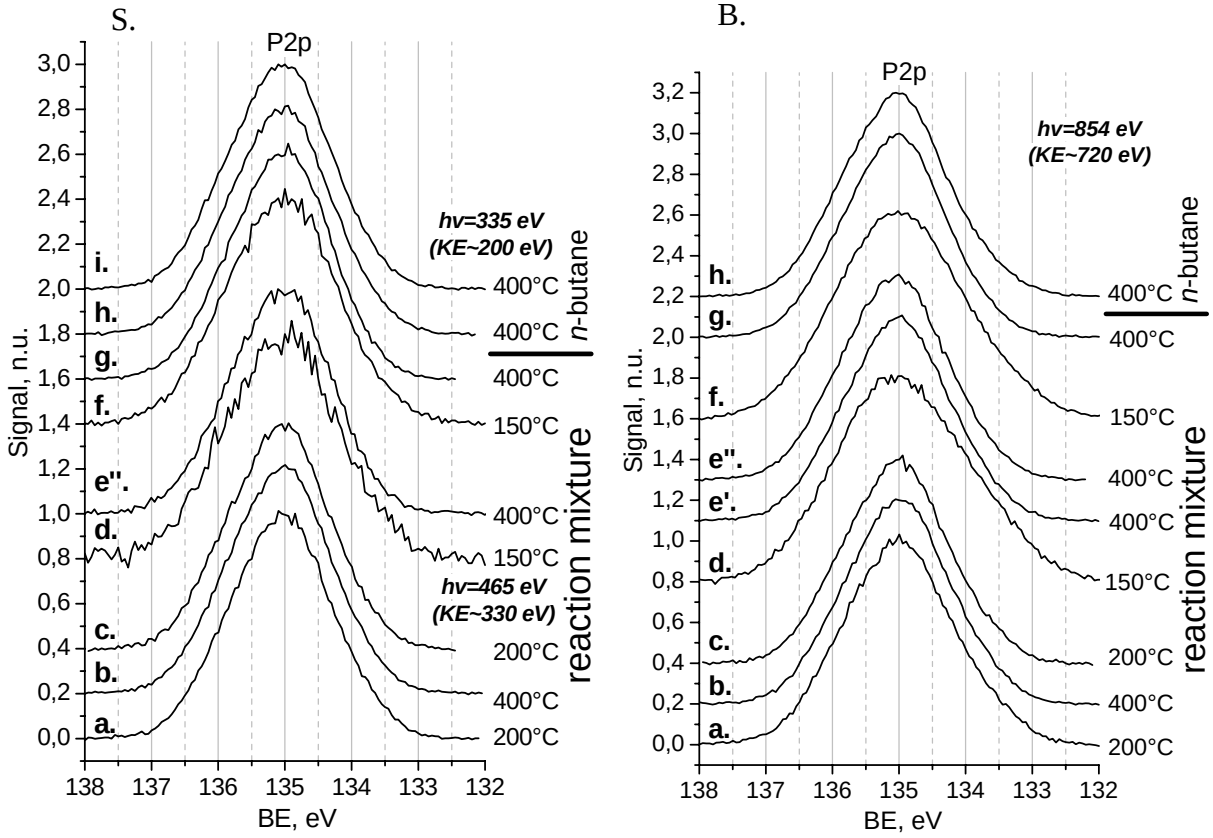

This peak could in principle, provide information about the chemical state of phosphor atoms. Nevertheless, the changes in the peak shape are very small and a reliable BE reference is necessary for extraction of the information. The O1s peak, which was used for BE calibration of the $V2p_{3/2}$ region is unfortunately, not suitable for BE calibration of the P2p region in the surface sensitive mode, because it is not present in the spectra due to the low excitation energy.

The C1s peak is formed by carbon-containing species of various natures. The most interesting thing in respect of understanding of the reaction mechanism would be of course, obtaining from the C1s peak information about the nature and an amount of reaction intermediates and products on the surface. Nevertheless, investigation of a real (not model) catalyst under reaction conditions implies the presence on the surface of carbon oxides, different kinds of hydrocarbons and a graphitic layer, which appears because of adsorption and decomposition of reaction gas molecules as well as because of diffusion of carbon incorporated in a catalyst material and because of gas-assisted transport of carbon containing on the surface of the experimental chamber. Most of these carbon species are not related to the catalytic reaction. In the experimental C1s spectra (Figure 4-18 and Figure 4-19) at least three features changing their relative intensity are visible.

Figure 4-18. Evolution of the C1s peak of the sample-1.
Sample activity during the experiment is shown on Figure 4-4.

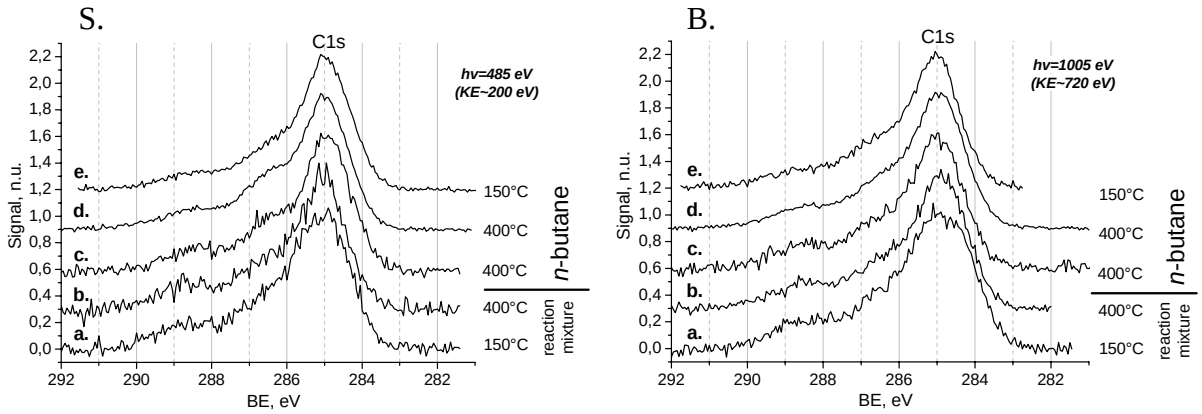

Figure 4-19. Evolution of the C1s peak of the sample-2.
Sample activity during the experiment is shown on Figure 4-5-(a-c).

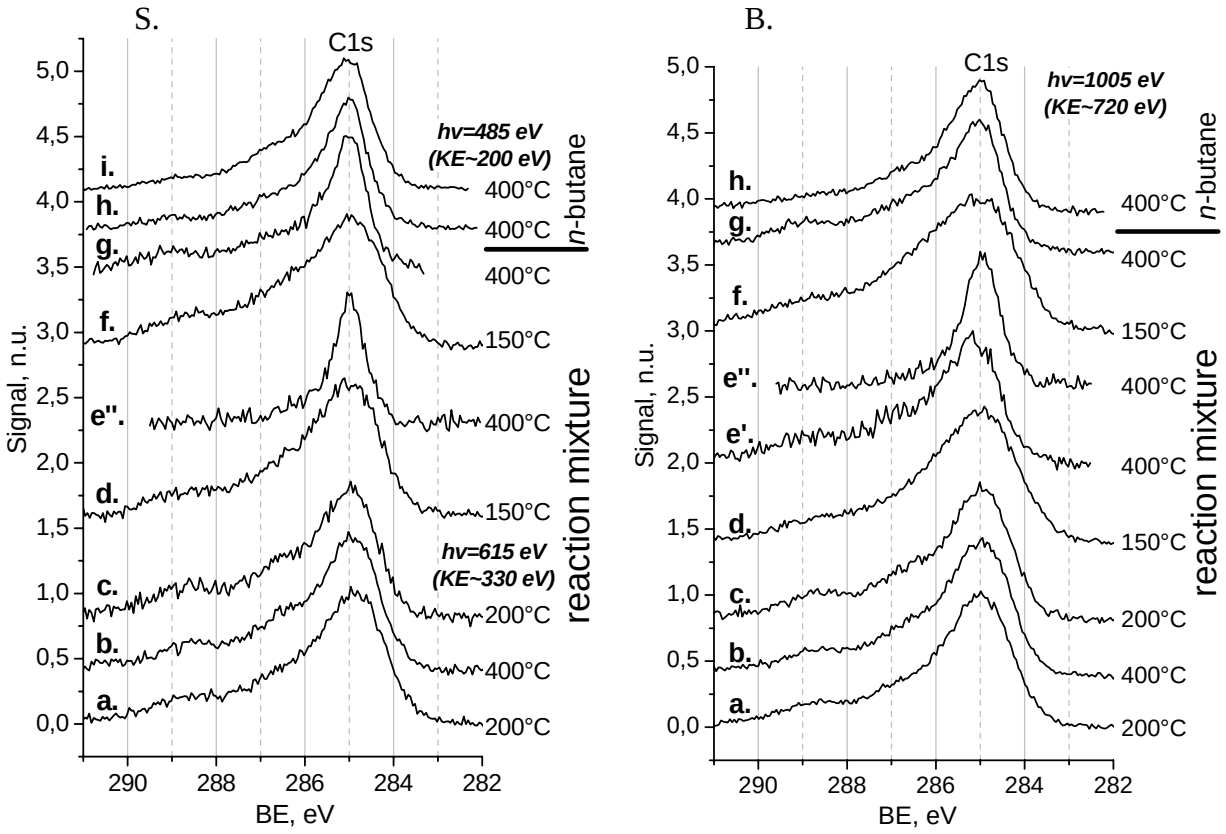

The first feature is the highest peak in the C1s region. BE scale of this region was calibrated to the position of the maximum of this peak at 285 eV. The gas-phase C1s peak was found to have a similar BE position, but this feature cannot be related solely to the gas phase because it was observed also in vacuum and in oxygen atmosphere. The second feature is at 286.5 eV and the third one is at 288.5-289 eV. Although one can try to assign these features to some carbon-containing compounds based on literature data, observation clearly

shows that two of these features do not relate to the catalytic reaction. The spectra e" on Figure 4-19 have no peak at 286.5 and 288.5-289 eV, while all the other spectra do have it, including the spectra b, e' and g, which were recorded at the same conditions. Figure 4-5-b shows the time dependence of temperature and MA yield during a part of experiment with the sample-2.

Some time after 400°C was reached the temperature starts to fluctuate. These fluctuations were caused by a defect of electric heater contacts, which was fixed afterwards. The spectra e' and e" (Figure 4-19-B) were recorded before and after these fluctuations. The data for the stoichiometry which will be discussed in part 4.8 show a significant drop in C/V ratio after heating to 400°C, but not between the spectra e' and e". Obviously, fast thermal fluctuations caused desorption of carbon species from the surface, which were replaced by another carbon species. This change in carbon content had no influence on the catalytic performance of the sample (Figure 4-5-b), which allows one to conclude that the desorbed species were not the intermediates or products. After recording this series of spectra the sample was cooled down and kept for 9 hours in air till the next experiment in which the C1s spectra "f" and "g" had already the initial three-peak structure. The failure to detect the intermediates in this experiment nevertheless, should not be viewed as a general inability of the method to do that. The detection of the intermediates would be a separate extensive study implying preparation of a carbon-free catalyst material, combined thermal-desorption and high-pressure XPS studies and *in situ* XPS experiments with variation of reaction conditions in order to change a catalytic activity.

The valence band region of VPO is formed by valence orbitals of phosphor, vanadium, oxygen and carbon atoms. The $(VO)_2P_2O_7$ structure of the bulk of an industrial VPO catalyst consists of vanadium and phosphor atoms surrounded by oxygens. Other VPO phases, defects and surface termination would add to this structural pattern P=O and V=O bonds. One can expect formation of the valence band by the V3d, O2p and hybridized oxygen-vanadium and oxygen-phosphor orbitals. Although in P_2O_5, which is a P^{5+} oxide, phosphor valence orbitals are formally empty, one can nevertheless, expect appearance in the spectra of a P3s-component because of defects and surface termination. The spectra are also complicated by the presence on the surface of carbon-containing compounds. They will introduce into the spectra the C2s and C2p components as well as the components corresponding to carbon-oxygen hybridized orbitals. In such a view the comparison of the VPO VB shown on Figure 4-20 and Figure 4-21 with the VB of binary vanadium oxides from Figure 4-9 and [105], [106], [108] as well as with the VB of P_2O_5 [109] and carbon films [110] can help

understanding of peculiarities of VPO VB. The small peak at 1 eV can be assigned to V3d states, which are inherent to vanadium oxides with oxidation sate of vanadium lower than 5. The broad structure with three peaks between 3 and 13 eV is mostly formed by O2p states hybridized with valence orbitals of vanadium, phosphor and carbon atoms. The peak at 15 eV can be related to carbon valence orbitals [110] as well as the peak at 10 eV, which grows up in the *n*-butane/He atmosphere on Figure 4-21. Therefore, the valence band region of VPO has quite a complicated structure with contribution of several elements and consequently, is not suitable for extraction of reliable information about the electronic structure of elements without additional extensive experimental and theoretical studies.

Figure 4-20. Evolution of the VB region of the sample-1.
Sample activity during the experiment is shown on Figure 4-4.

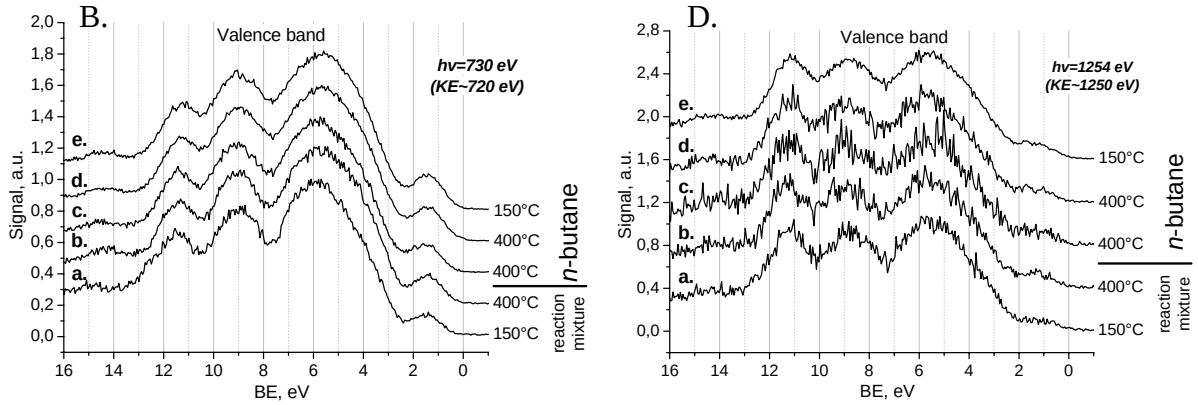

Figure 4-21. Evolution of the VB region of the sample-2.
Sample activity during the experiment is shown on Figure 4-5-(a-c).

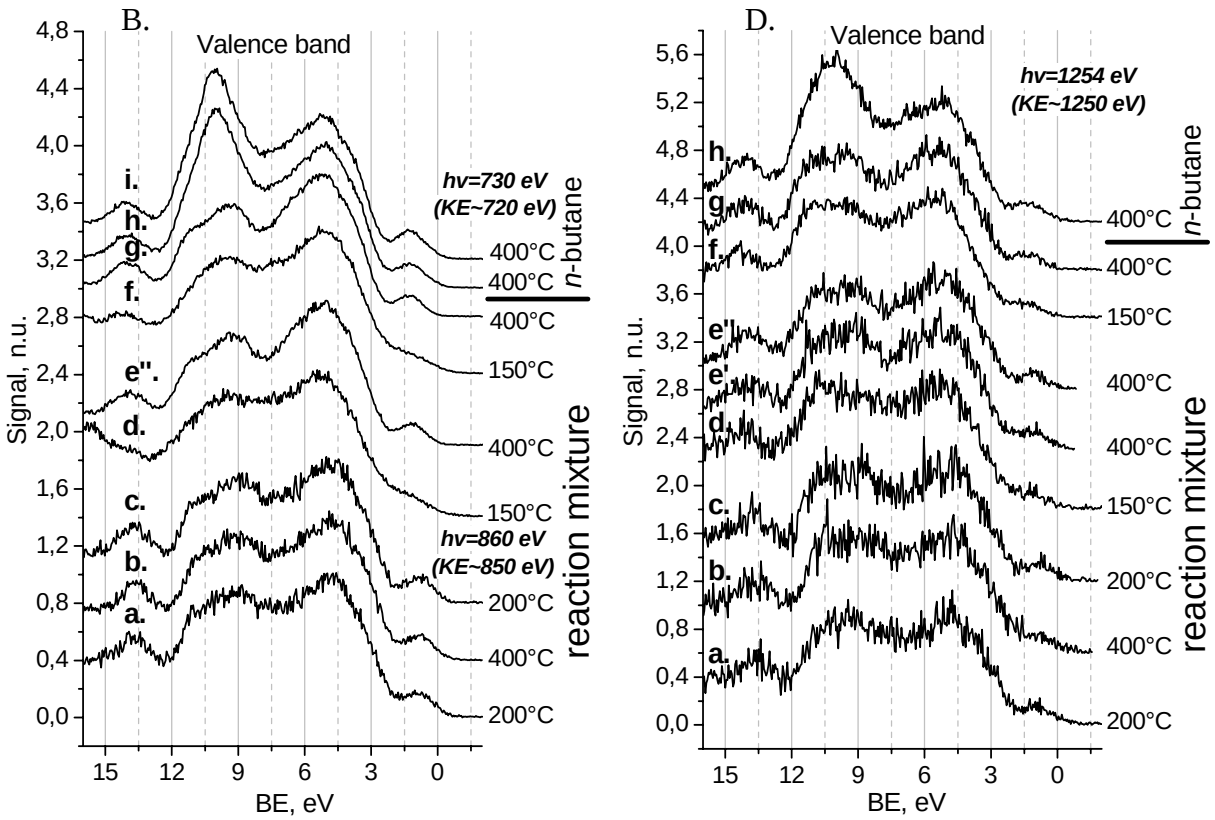

4.7 Change of vanadium oxidation state.

The XP spectra of various vanadium oxides, which are the reference compounds for determination of vanadium oxidation state, were extensively discussed in literature ([105], [106], [107], [111]). Data of a BE of $V2p_{3/2}$ of these compounds are summarized in Table 4-3.

Table 4-3. Summary of data for determination of a vanadium oxidation state.

Source	Oxide	Ox.st.	BE of Ref. peak, eV	BE (O1s), eV	BE ($V2p_{3/2}$), eV	FWHM ($V2p_{3/2}$), eV	ΔBE (O1s-$V2p_{3/2}$), eV
Figure 4-8	V_2O_5, reduced	5	O1s 530.0	530.0	517.1	0.8-1.4	12.9
		4			515.6-516.0	1.3-1.4	14.0-14.4
[105]	V_2O_5	5	FE of sample holder	529.8	516.9	1.6	12.9
	VO_2	4		529.9	516.2	3.2	13.7
	VO_2	4		529.7	515.9	4.1	13.7
	V_2O_3	3		530.1	515.7	4.2	14.4
	V_2O_3	3		530.3	515.9	3.8	14.4
[106]	V_2O_5	5	Au4f/C1s 84.0/285	(530)	517.2	1.2	(12.8)
	VO_2	4			516	1.95	(14.0)
	V_2O_3	3			515.85	4	(14.15)
[107]	V_2O_5	5	O1s 329.8/ 530.0	529.8	517.0	1.3-1.4	12.8
	V_6O_{13}	4.33		530.0	516.5	3.4	13.5
	VO_2	4		530.0	515.65	4.0	14.35
	V_2O_3	3		530.0	515.15	4.8	14.84
[111]	V_2O_5	5	FE of Au	530.0	517.1	1.1	12.9
	VO_2	4		530.1	516.2	2.5	13.9
	V_2O_3	3		530.2	515.6	3.5	14.8

The fact, that the peaks corresponding to the 5+ and 4+ oxidation states are nicely separated can be used for determination of a relative amount of atoms in a certain oxidation state or for estimation of an average oxidation state. The data for the ΔBE for V^{5+} are very well internally consistent, but the data for V^{4+} and V^{3+} have big scattering. Nevertheless, the V^{3+} component in the $V2p_{3/2}$ peak always has a lower BE and a greater width compared with V^{4+}. In the case of admixture of the V^{3+} component to a spectrum having the main V^{4+} component the resulting spectrum would be asymmetrically broadened towards the low-BE side. As we will see further below, this is not the case for the recorded VPO spectra.

There are several procedures to estimate an oxidation state from an XPS spectrum.

Peak-profile fit is a mostly used procedure. Determination of the oxidation state ***x*** by this method implies that the peak consists of several components of known profile. Each of

these components corresponds to the contribution of atoms with a certain whole oxidation state ***n***. Fit of the experimental spectrum points ***{y_i}*** by sum of the components ***{$y(x_i)$}*** is usually performed by minimization of the square deviation $\sum_i (y_i - y(x_i))^2$ by variation of component areas and in some cases also by variation of widths, positions and line shapes (for example Gauss-Lorentz ratio in the Voigt profile). Nevertheless, this method implies knowledge of the shapes of these components, which is quite rarely available. Usually one use some idealized profiles, such as the Voigt (or the simpler to handle Gauss-Lorentz product) or Doniach-Sunjic profiles. This idealization is based on simple assumptions about the physical processes of X-ray emission, monochromatization, photoemission, photoelectron scattering and photoelectron kinetic energy monochromatization. The intrinsic profile of photoemission lines is usually assumed to be lorentzian because of the life-time broadening, while an X-ray monochromator and an electron energy analyzer introduce the gaussian instrument broadening. Differential charging is usually assumed to introduce the gaussian broadening. The result of convolution of these profiles is the Voigt profile. In the case of a metallic material the photoelectron line shape is non-symmetrical and Doniach-Sunjic profile should be used. Although the fit approach works quite well for low-resolution measurements, it is hardly applicable to spectra measured with a high resolution because of a fine structure of a core-level, which often makes the peak asymmetrical. An example of an asymmetrical peak is $V2p_{3/2}$ corresponding to the V^{5+} state on Figure 4-8 (page 72). Use of the mentioned above profiles for an asymmetrical peak would lead to a systematic error in the calculated oxidation state. Another problem, which is nevertheless, a general problem for estimation of an oxidation state from XPS data is limited adaptability of the concept of proportionality of a formal oxidation state to a BE position of the component. The BE position is sensitive to the effective charge of the atom or ion in the lattice, which in general, cannot be described by integer charge values only. Additionally, a BE position depends on the final-state effect, which also depends on the atom surroundings. This can lead to different binding energies of compounds with the same formal oxidation state and finally, to an error in the estimated oxidation state. The last and probably, the most important problem of this method is uncertainty in fit parameters. This usually appears in low-resolution spectra with strong-overlapping components. Such a profile can be successfully fitted by various numbers of components with various widths and relative binding energies. In such a case the analysis of the same experimental data by different persons can give completely different results. The main rule in the analysis of such overlapping spectral structures is to fix or constrain from *a priori* or *a posteriori* knowledge as many fit parameters as possible. Nevertheless, this meets

with success not always and an absolute value of oxidation state received by this approach can be easily criticized.

Another approach to estimate an oxidation state or at least, its relative change is the ***difference spectrum*** approach, which is based on subtraction from the data of a reference spectrum of a compound with known oxidation state. Although this approach is free from most drawbacks of the peak-profile fit method, it nevertheless, implies very careful BE calibration and peak amplitude normalization because even small shifts, which would not affect the fit procedure results, will lead to appearance of additional structure in the difference spectrum. The correct subtraction procedure is described in [112] and an example of its application can be found in [113]. Charging or other effects causing broadening of a peak would strongly affect in a negative way the shape of the difference spectrum. To compensate the broadening one can convolute the subtracted spectrum with a gausssian of an appropriate width. The method of a difference spectrum is especially valuable for analysis of small shape changes while in the case of pronounced changes and symmetrical components it will give practically the same result as the fit procedure, but will cost much more in data manipulation efforts.

Some other methods can be applied to extract information about a mean oxidation state. Coulston et al. [25] estimated the ***dependence of a vanadium oxidation state of VPO on a difference of first momenta of the O1s and V2p$_{3/2}$ peaks***. The equation x=13.82-0.68*[O(1s)-V(2p$_{3/2}$)] was estimated for the oxidation state ***x*** by reference compound measurements (here the first momenta O(1s) and V(2p$_{3/2}$) should be measured in eV). The result is independent on peak broadening because symmetric broadening will not change the first momenta. The disadvantage of the method is dependence of a first momentum of the O1s peak on the presence of adsorbates. This method is hardly applicable for our case because adsorbates are obviously present on the surface.

The method of a difference spectrum was chosen as the most suitable method for determination of a change in oxidation state on base of our experimental data. Application of the fit method could lead to a bigger error in oxidation state because of uncertainty in component widths and positions.

The V2p$_{3/2}$ spectra of the sample-1 and sample-2 during the experiment of heating-cooling in the reaction mixture are shown on Figure 4-22. The same spectra were already presented as the spectra (a-b) on Figure 4-14 and (a-c) on Figure 4-15. The difference spectra are also shown on this figure.

Figure 4-22. V2p$_{3/2}$ spectra of the sample-1 and sample-2 before and after heating in the reaction mixture.

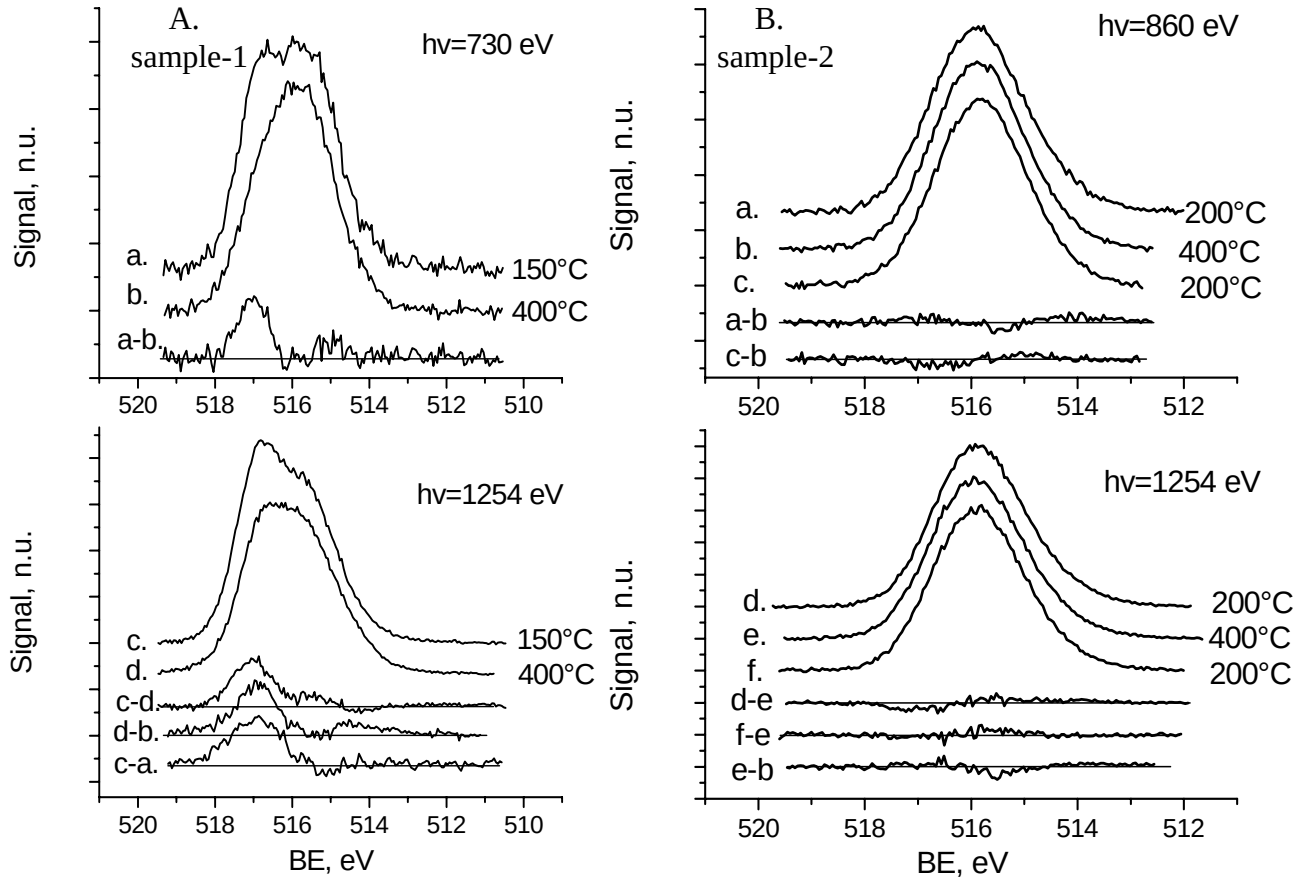

The spectra of the sample-1 are shown on Figure 4-22-A. The spectra reveal strong changes of vanadium oxidation state with temperature. The peak at 517 eV is clearly visible in the difference spectra for both bulk (spectrum c-d.) and surface (spectrum a-b.) sensitive measurements. This peak has a BE-difference of about -13 eV relative to the maximum of O1s, which is a typical value for V^{5+} species (see Table 4-3). The same feature was observed in the difference between bulk and surface spectra at 150°C (the spectrum c-a.) and at 400°C (the spectrum d-b.). This means that a strong gradient in oxidation state is present in the near-surface region of the sample-1 under the reaction and non-reaction conditions.

Different behavior was observed for the sample-2. The difference spectra on Figure 4-22-B show only small features with amplitudes of about the noise amplitude, which implies that no changes are observed in the spectra within the uncertainty of our experiments. This leads us to the conclusions that a vanadium oxidation state of the sample-2 is uniform with depth in the near-surface region and does not change with temperature.

On Figure 4-23-A the spectra under reaction conditions (the reaction mixture, 400°C) are drawn. These spectra were already shown on Figure 4-22-A and -B. From comparison of the spectra it is obvious that values of oxidation state of the surface of the catalysts are closer to each other than values of oxidation state of the bulk.

Figure 4-23. Comparison of the V2p$_{3/2}$ peaks of the sample-1 and sample-2 in the reaction gas mixture.

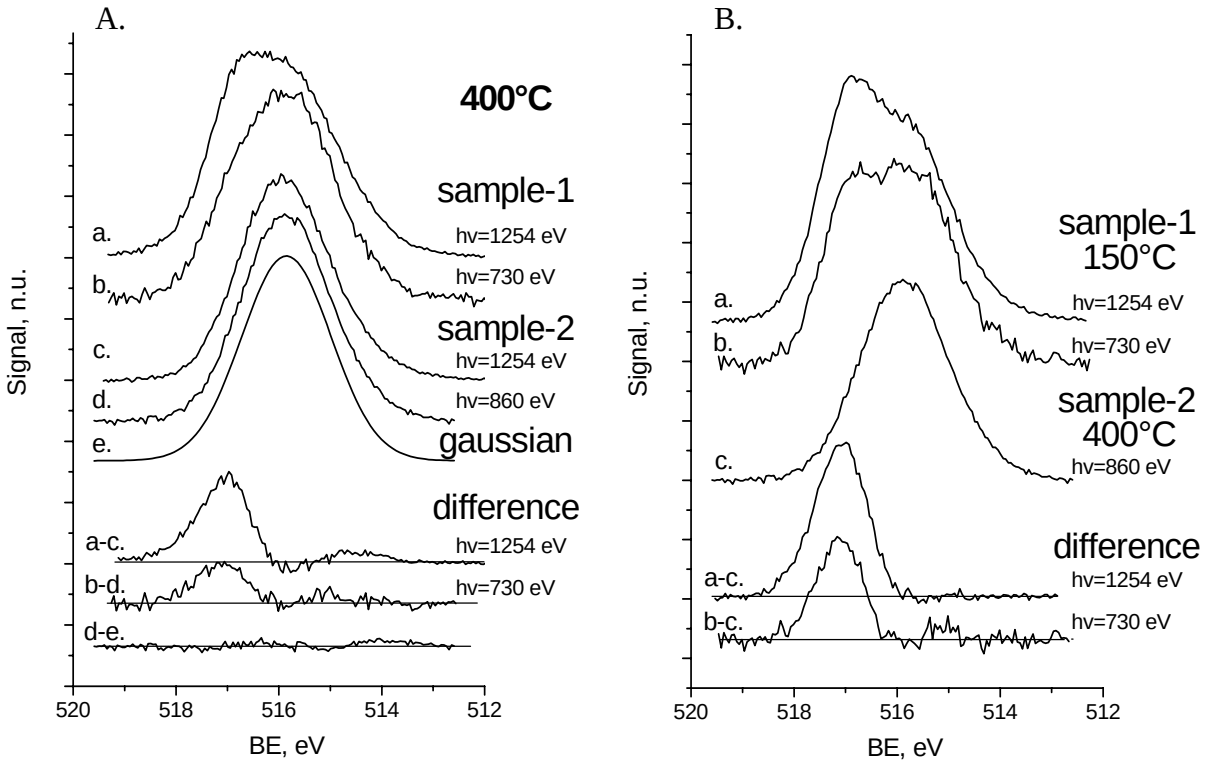

The shape of the surface V2p$_{3/2}$ peak of the sample-2 (spectrum d on Figure 4-23-A) under reaction conditions can be fit with a single gaussian with the maximum at 515.85 eV. This value falls into the BE region of the V^{4+} component (Table 4-3). To estimate a confidence interval for the determined oxidation state one should take into account an uncertainty in the calibration of BE scale in our experiment, which cannot be better than ±0.05, and scattering of the data in Table 4-3. The resulting uncertainty in position of the peak maximum in the spectrum d. relative to the true position of the V^{4+}-component should be estimated to be ca. 0.1 eV. The variation of an oxidation state estimated by the fit of a VPO spectrum by two gaussians with variation of a V^{4+}-component position was found to be 0.1 per 0.1 eV. This means that the oxidation state of the sample-2 at the reaction conditions is (4.0 ± 0.1) eV.

An excess of the V^{5+} in the bulk and on the surface of the sample-1 relative to the active surface of the sample-2 can be estimated from the difference spectra a-c. and b-d. on

Figure 4-23-A for 400°C and from the spectra a-c. and b-c. on Figure 4-23-B for 150°C. At 400°C ***the part of the V^{5+} component area ΔA in the whole peak area A is $a=\Delta A/A$***=(0.12 ± 0.04) in the surface sensitive mode and (0.19 ± 0.01) in the bulk sensitive mode. At 150°C this is (0.19 ± 0.01) and (0.32± 0.01) respectively. The error values correspond to the noise level in the difference spectra. From correlation of these data with information depth (Table 4-2) it is intuitively obvious that change of an oxidation state takes place in the near-surface region with thickness of one or several nm. Extrapolation of ***$a(\lambda)$*** for $\lambda \to 0$ will give $a(0) \approx 0$, which implies the identical oxidation state of the surface of the sample-1 and sample-2. Below this statement will be proven by use of some simple models of an oxidation state distribution.

Firstly the simple ***linear distribution of an oxidation state*** with depth can be suggested. If the ***oxidation state of the surface of the sample-2*** is denoted by ***x_{S2}***, than ***the part of vanadium atoms in the 5+ oxidation state $c=n_{5+}/n$*** in the sample-2 (assuming the presence of 5+ and 4+ only) will be:

$$c_{S2} = x_{S2} - 4 = (0.0 \pm 0.1) \qquad (4\text{-}1)$$

The same quantity for the sample-1 will depend on the ***depth z***:

$$c(z) = c_0 + \alpha \cdot z \qquad (4\text{-}2)$$

where $c_0=c(0)$ and ***α is a*** constant ***gradient of c***.

The ***relative contribution $C(\lambda)$ of vanadium atoms in the 5+ oxidation state into the $V2p_{3/2}$ XPS peak*** can be found as:

$$C(\lambda) = \int_0^\infty n_{5+}(z) \cdot e^{-z/\lambda} dz \Big/ \int_0^\infty n(z) \cdot e^{-z/\lambda} dz \qquad (4\text{-}3)$$

Here c(z) was convoluted with the probability of photoelectron escape $1/\lambda \cdot e^{-z/\lambda}$, which depends on the photoelectron inelastic mean free path λ and thus, on a photoelectron kinetic energy. Assuming the concentration of vanadium atoms n(z) to be uniform with depth and substituting $n_{5+}/n=c(z)$ from equation (4-2) we will get the equation for the ***difference $\Delta C(\lambda)$*** between the contribution $C(\lambda)$ of V^{5+} to the spectrum of the sample-1 and the analogous contribution C_{S2} to the spectrum of the sample-2:

$$\Delta C(\lambda) = C(\lambda) - C_{S2} = c_0 - c_{S2} + \alpha \cdot \lambda = \Delta c_0 + \alpha \cdot \lambda \qquad (4\text{-}4)$$

This quantity is also connected with ***$a=\Delta A/A$*** estimated from the difference spectrum:

$$\Delta C(\lambda) = (1 + c_{s2}) \cdot a \qquad (4\text{-}5)$$

Substituting this equation into (4-4) we obtain:

$$a \cdot (1 + c_{s2}) = \Delta c_0 + \alpha \cdot \lambda \qquad (4\text{-}6)$$

and consequently, Δc_0 and α will be found as

$$\Delta c_0 = (1 + c_{S2}) \cdot \frac{a(\lambda_1) - \frac{\lambda_1}{\lambda_2} \cdot a(\lambda_2)}{1 - \lambda_1/\lambda_2} \qquad (4\text{-}7)$$

$$\alpha = (1 + c_{S2}) \cdot \frac{a(\lambda_2) - a(\lambda_1)}{\lambda_2 - \lambda_1} \qquad (4\text{-}8)$$

The errors of these quantities can be estimated as:

$$error(\Delta c_0) = (1 + c_{S2}) \cdot \frac{error(a(\lambda_1)) + \frac{\lambda_1}{\lambda_2} \cdot error(a(\lambda_2))}{1 - \lambda_1/\lambda_2} \qquad (4\text{-}9)$$

$$error(\alpha) = (1 + c_{S2}) \cdot \frac{error(a(\lambda_2)) + error(a(\lambda_1))}{\lambda_2 - \lambda_1} \qquad (4\text{-}10)$$

The c_{S2} value is known from (4-1). Substituting into (4-7) - (4-10) the values of ***a*** obtained from Figure 4-23-A and -B and corresponding λ from Table 4-2 we will get $\Delta c_0^{150°C} = (0.06 \pm 0.01)$, $\alpha^{150°C} = (0.14 \pm 0.01)$ nm^{-1}, and $\Delta c_0^{400°C} = (0.03 \pm 0.09)$, $\alpha^{400°C} = (0.09 \pm 0.05)$ nm^{-1}. These values are nevertheless, overestimated because our model (Equation (4-2)) implies linearity of c(z) in the whole region $z \in (0,\infty)$, which makes no sense at high z, where c(z) calculated using this formula will be grater than unity. Thanks to the presence in the formulas (3-3)-(4-3) of $e^{-z/\lambda}$, which is decreasing much faster at $z \to \infty$ than $\alpha \cdot z$ is increasing, the product can be well integrated on this semi-infinite interval. The deviation δ from the real values can be estimated assuming that the linear model (4-2) is held perfectly true in the region $z \in (0,\lambda_2)$:

$$\delta\Delta c_0 = \alpha \cdot \frac{1 + c_{S2}}{1/\lambda_1 - 1/\lambda_2} \cdot \left(e^{-1} - e^{-\lambda_2/\lambda_1}\right) \qquad (4\text{-}11)$$

$$\frac{\delta\alpha}{\alpha} = \frac{1 + c_{S2}}{1 - \lambda_1/\lambda_2} \cdot \left(e^{-1} - \lambda_1/\lambda_2 \cdot e^{-\lambda_2/\lambda_1}\right) \qquad (4\text{-}12)$$

The deviations found by these formulas are: $\delta\Delta c_0^{150°C} = 0.06$, $\delta\alpha^{150°C} = 0.08$ nm^{-1}, and $\delta\Delta c_0^{400°C} = 0.04$, $\delta\alpha^{400°C} = 0.05$ nm^{-1}. These values are comparable with the experimental errors and therefore, the linear model can be referred to as having acceptable accuracy.

Although the linear model discussed above gives a reliable value of the surface oxidation state, it does not help to find the thickness of the surface layer there the changes take place. To estimate the value of this thickness one can use the step-like distribution model:

$$c(z) = \begin{cases} c_0 & , \quad z \le d \\ c_1 & , \quad z > d \end{cases} \qquad (4\text{-}13)$$

Taking into account that one deals with the well-equilibrated catalysts which were working for a long time, it is reasonable to assume that the catalyst bulk will not change its oxidation state coming from a low temperature to the reaction conditions and all changes will take place in a near-surface region. Therefore, the bulk concentration c_1 will be taken the same for both the low-temperature and the reaction temperature. The ***thickness d*** is supposed to change with temperature and will be respectively denoted $d^{400°C}$ and $d^{150°C}$. The surface concentration c_0 will be taken as the same for both temperatures to equalize a number of parameters with the number of equations. Although this assumption is not absolutely correct, from the linear model we know that a surface oxidation state should not be very different for these two temperatures and therefore, this simplification does not lead to a significant error. The relation between the quantity ***a*** and other parameters will be found by analogy with the linear model:

$$a \cdot (1 + c_{s2}) = \Delta c_0 + \Delta c_b \cdot e^{-d/\lambda} \qquad (4\text{-}14)$$

where $\Delta c_0 = c_0 - c_{S2}$ and $\Delta c_b = c_1 - c_0$. Substituting into this equation $a^{150°C}(\lambda_1)$, $a^{150°C}(\lambda_2)$, $a^{400°C}(\lambda_1)$ and $a^{400°C}(\lambda_2)$ we will get a system of four equations with the set of variables {Δc_0, Δc_b, $d^{150°C}$, $d^{400°C}$}. This system should be solved numerically and the solution is: $\Delta c_0 = (0.08 \pm 0.08)$, $\Delta c_b = (0.5\ ^{+\ 0.3})$, $d^{150°C} = (2 \pm 1)$ nm, $d^{400°C} = (3.5 \pm 2.0)$ nm, where the errors were obtained by variation of values of ***a*** within their errors. One should note that the obtained Δc_0 value is the same as for the linear model within the experimental error.

From the results of the calculations based on these two models one should conclude that both catalysts have the same oxidation state of the outmost surface molecular-layer at the reaction conditions within the experimental error. The thickness of the layer in which changes of oxidation state take place is several nanometers.

Stability of the active layer towards reducing conditions can be demonstrated by *in situ* XPS data for the samples in *n*-butane/He atmosphere. It is clearly visible on Figure 4-24 that the surface of the sample-1 responds much more dynamically to the reducing conditions comparing the sample-2. MA yield for the sample-1 also decreases much faster (see Figure

4-6 on page 70). There could be two reasons for the different response of these two samples to the change of conditions: either differences in properties of the active layer or different interaction with deeper layers (substrate). The second hypothesis is more probable since the oxidation state of the two surfaces was the same for both catalysts under reaction conditions, which suggests the same nature of the surface layer for both catalysts. This implies that the oxygen transport from the substrate to the surface is better for the sample-2 as compared to the sample-1. Obviously, this does not influence significantly the catalytic performance of the active layer in the co-feed of oxygen and n-butane, but apparently makes sample-2 more stable with respect to condition changes.

Figure 4-24. Changes of the surface V2p$_{3/2}$ spectra in *n*-butane at 400°C.

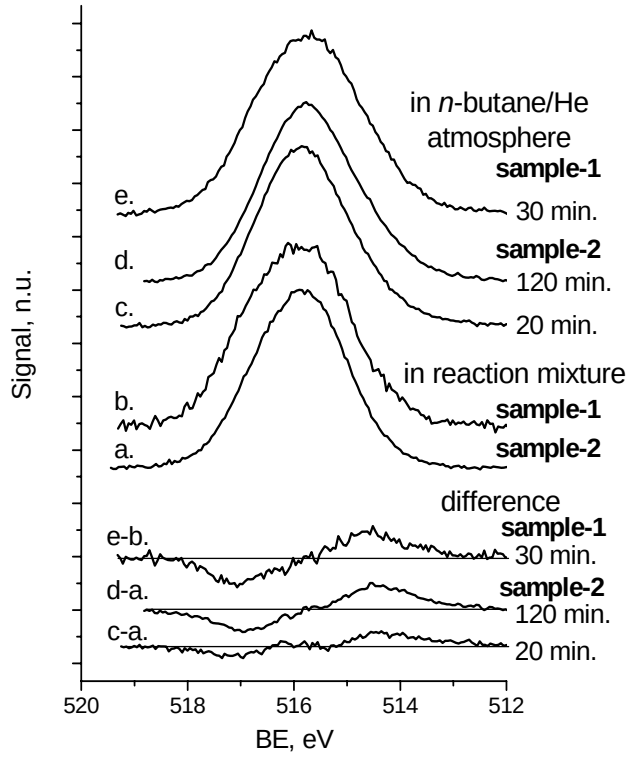

4.8 Stoichiometric ratios.

The possibility of estimation of a surface stoichiometry is one of the main strengths of the XPS technique. Nevertheless, the problem of sensitivity factors usually comes up during estimation of absolute values of stoichiometric ratios. Most estimations in literature are based on the theoretical cross-sections [23] and [95], which were shown to give a wrong result for some compounds [25]. G.W. Coulston with colleagues ([25]) have experimentally estimated a sensitivity factor for the P/V stoichiometric ratio by measurement of some organometallic compounds.

In the present work measurements of some reference compounds have been performed in order to estimate experimental sensitivity factors for O/V, P/V and C/V ratios. For this purpose XP spectra of V_2O_5 and α_{II}- , β-, γ-$VOPO_4$ (the structure of $VOPO_4$ compounds was checked by XRD) in O_2 atmosphere at room temperature were recorded. No contribution of oxygen gas phase is expected to an O/V stoichiometric ratio because the surface and the gas-phase O1s XPS peaks are well resolved. Additionally, CO_2 gas phase was used as a reference for estimation of a C/O ratio. The experimental sensitivity factors (Table 4-4) were estimated as a formal stoichiometry of a compound divided by the peak area ratio. Here and further calculation of a peak area implies preliminary normalization of an XPS signal to an electron current in the electron storage ring in order to take into account change of X-ray intensity with time. The theoretical cross-sections presented in the same table were calculated according equation (3-7) on page 16 as

$$S(A/B) = \frac{f_A^0 \cdot k_A}{f_B^0 \cdot k_B} \cdot \frac{\sigma_A}{\sigma_B} \qquad (4\text{-}15)$$

where $f_{A,B}^0$, $k_{A,B}$ and $\sigma_{A,B}$ are an X-ray flux before the X-ray window, a transmission of the X-ray window and a photoionization cross-sections at respective *hv*. The stoichiometric ratio thus, will be found as

$$\frac{n_A}{n_B} = \frac{I_A}{I_B} \Big/ S(A/B) \qquad (4\text{-}16)$$

One should note the big scattering of the data for calculation of O/V and P/V sensitivity factors in Table 4-4 and Figure 4-25.

Table 4-4. Sensitivity factors estimated from peak area ratios of some reference compounds and their comparison with calculations based on [23].

		KE=290 eV	KE=470 eV	KE=290 eV	KE=470 eV	Average
	O/V	O1s/V2p$_{3/2}$ area ratio		Sensitivity factor S(O/V)		
V_2O_5 in O_2	2.5	1.33	1.91	0.53	0.76	
α-, β-, γ-$VOPO_4$ in O_2	4	3.60	3.86	0.90	0.97	
	4	3.66	3.67	0.92	0.92	
	4	3.05	3.11	0.76	0.78	
Average				***0.78±0.18***	***0.86±0.10***	
Theoretically calculated				***0.39***	***0.39***	
Correction coefficient				**2.0±0.5**	**2.2±0.3**	**2.1±0.5**
	P/V	P2p/V2p$_{3/2}$ area ratio		Sensitivity factor S(P/V)		
α-, β-, γ-$VOPO_4$ in O_2	1	4.37	8.77	4.37	8.77	
	1	3.29	6.45	3.29	6.45	
	1	3.62	7.30	3.62	7.30	
Average				***3.8±0.6***	***7.5±1.2***	
Theoretically calculated				***1.9***	***3.4***	
Correction coefficient				**2.0±0.3**	**2.2±0.5**	**2.1±0.5**
	C/O	C1s/O1s area ratio		Sensitivity factor S(C/O)		
CO_2 gas	0.5	0.71	1.45	***1.43***	***2.90***	
Theoretically calculated				***1.83***	***3.54***	
Correction coefficient				**0.8**	**0.8**	

Figure 4-25. Dependence of O1s/V2p$_{3/2}$ peak area ratios of some reference compounds on the nominal O/V atomic ratios and its comparison with a calculation on base of [23]

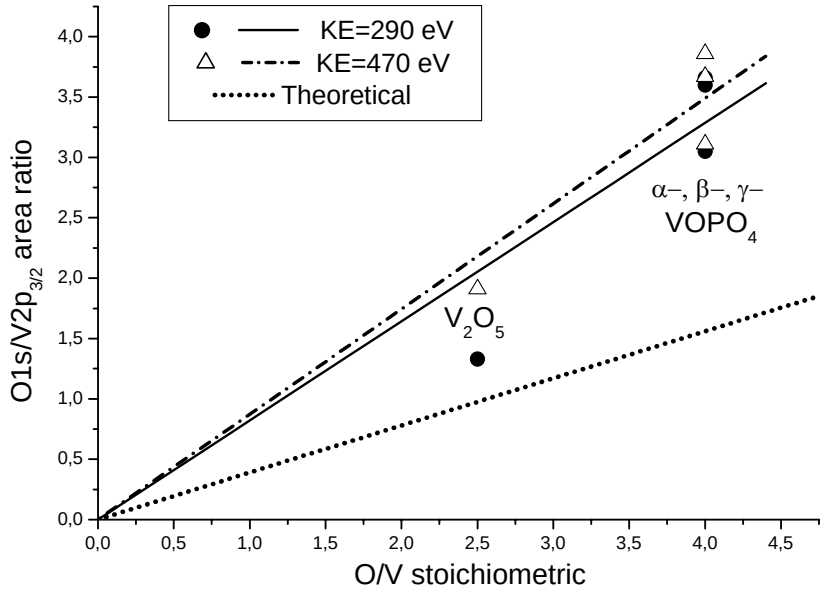

The error in the average sensitivity factor was estimated as a standard deviation of the data. Although reliable independent estimation of a real value of surface stoichiometry is practically not possible, this scattering clearly indicates that a surface stoichiometry is different from the formal stoichiometry of a compound and the calculations on base of this experimental sensitivity factors should be viewed as a rough estimation of the surface stoichiometry. Nevertheless, test measurements of a stoichiometry of a VPO compound with the nominal ratios O/V=4.5 and P/V=1 (Figure 4-26) shows that the estimation of a stoichiometry on the base of the experimentally corrected sensitivity factors is closer to the real value than the estimation on base of the theoretical sensitivity factors. For example, the theoretical value of stoichiometry O:P:C:V=9:2:2:1 over the topmost 1.5 nm would be quite doubtful because of the presence of an enormous amount of oxygen.

Figure 4-26. Estimated atomic ratios for a VPO compound with the nominal stoichiometry P/V=1, O/V=4.5.

The measurements were performed in the reaction mixture. Atomic ratios were calculated using the data from [23] and the experimentally estimated sensitivity factors (Table 4-4).

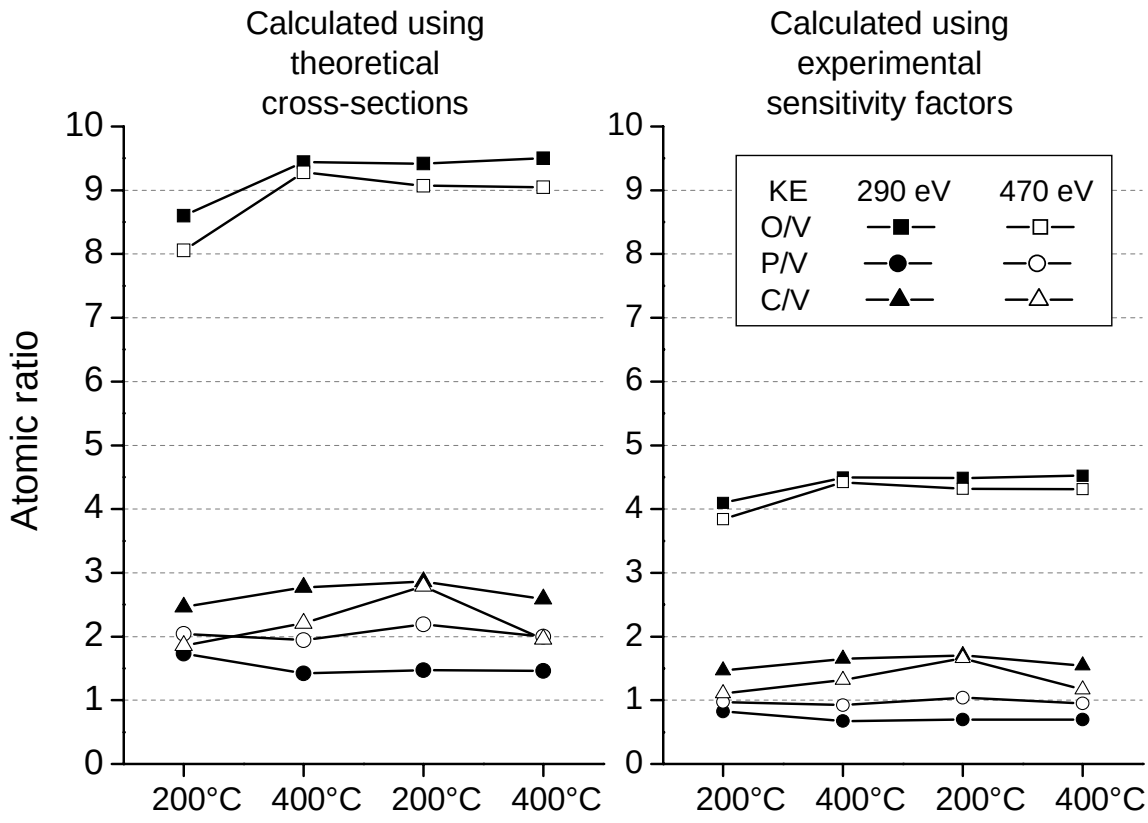

The estimation of a C/O sensitivity factor is very precise because the stoichiometry of the CO_2 gas molecules is well known and the error is dependent only on an uncertainty in the peak area, which usually does not exceed 10%. Would one use some gas reference compounds, which are not so stable as CO_2, mass-spectrometry will offer a possibility to estimate the average stoichiometry of the gas mixture. Therefore, high-pressure XPS on gas-phase reference compounds offers a solution of the general problem of precise estimation of a surface stoichiometry.

Correction coefficients were estimated as a ratio between the experimental and theoretical sensitivity factors. A stoichiometry of the VPO samples estimated with help of the theoretical cross-sections was corrected by division on these coefficients. The value of the correction coefficient for S(P/V) matches the value estimated in the literature (Figure 3 in [25]), where it was found to be equal 2. The error of the correction coefficients determined for the kinetic energies is greater than the difference between the values of the coefficients. Therefore, the average correction coefficient 2.1 was used for both S(O/V) and S(P/V) independently from KE to determine a stoichiometry of the VPO samples.

An X-ray flux normalized to a storage ring electron current, the transmission of the 100-nm-thick X-ray window and the theoretical cross-sections calculated by the approximation from [24] for the data [23] are presented in Table 4-5.

Table 4-5. Data for calculation of a stoichiometry of the sample-2.

hν, eV	Photon flux / synchrotron ring current, a.u. / mA	X-ray window transmission [37]	σ, Mb	
			O1s	$V2p_{3/2}$
730	3.70	0.83	0.25	0.64
860	3.25	0.89	0.17	0.43
1254	1.29	0.96	0.064	0.16
			P2p	
335	1.44	0.57	1.16	
465	2.80	0.57	0.50	
854	3.23	0.89	0.089	
			C1s	
485	2.93	0.60	0.29	
615	3.52	0.75	0.16	
1005	2.60	0.93	0.042	

Sensitivity factors calculated using this data were corrected by division of the average coefficients from Table 4-4. Relative changes in the stoichiometry of the sample-1 are presented in Table 4-6. The absolute numbers were not estimated for this catalyst because of technical problems, but the data for the sample-2 are enough to make a conclusion about stoichiometry of the active surface. Absolute values of the stoichiometry of the sample-2 are listed in Table 4-7. A random error of the stoichiometric data can be estimated to be 10%, which is coming from the uncertainty in a peak area. The error in the average O/V and P/V values represents a standard deviation of the data from the mean value.

Table 4-6. Change in a stoichiometry of the sample-1

T,°C	gas	Peak area ratio		
		O1s/V2p$_{3/2}$	P2p/V2p$_{3/2}$	C1s/V2p$_{3/2}$
KE=200 eV				
150	r. mixture	4.05	0.50	1.16
400	r. mixture	3.74	0.55	0.71
400	n-butane/He	3.72	0.53	0.66
400	n-butane/He	3.75	0.57	0.74
150	n-butane/He	3.86	0.51	0.96
KE=720 eV				
150	r. mixture	3.19	2.35	0.75
400	r. mixture	3.08	2.37	0.68
400	n-butane/He	3.12	2.38	0.51
400	n-butane/He	3.14	2.50	0.60
150	n-butane/He	3.19	2.42	0.72

Table 4-7. Change in a stoichiometry of the sample-2

T,°C	Gas	Area ratio			Corrected atomic ratio		
		O1s/V2p32	P2p/V2p32	C1s/V2p32	O/V	P/V	C/V
KE=330 eV							
200	r. mixture	4.00	1.56	1.71	4.86	1.17	3.05
400	r. mixture	3.78	1.70	1.07	4.60	1.28	1.92
200	r. mixture	3.79	1.53	1.02	4.60	1.15	1.81
KE=200 eV							
150	r. mixture	4.22	1.28	2.45	5.10	1.27	5.67
400	r. mixture	3.53	1.17	0.12	4.27	1.16	0.27
150	r. mixture	3.80	1.21	1.07	4.60	1.20	2.48
400	r. mixture	3.59	1.16	0.16	4.35	1.15	0.38
400	n-butane/He	3.69	1.07	0.23	4.46	1.05	0.53
400	n-butane/He	3.77	1.03	0.35	4.57	1.02	0.81
400	n-butane/He	3.89	1.04	0.52	4.71	1.03	1.20
Average					***4.6±0.2***	***1.1±0.1***	
KE=720 eV							
200	r. mixture	3.48	2.94	1.69	4.13	1.09	1.98
400	r. mixture	3.37	2.85	1.34	4.00	1.05	1.56
200	r. mixture	3.30	2.70	1.07	3.92	1.00	1.25
150	r. mixture	3.38	3.53	2.28	4.02	1.31	2.67
400	r. mixture	3.28	3.63	0.11	3.90	1.34	0.13
400	r. mixture	3.10	3.23	0.14	3.68	1.20	0.16
150	r. mixture	3.28	3.36	1.16	3.89	1.24	1.36
400	r. mixture	3.21	8.12	1.18	3.81	(3.00)	1.39
400	n-butane/He	3.24	3.22	0.54	3.85	1.19	0.63
Average					***3.9±0.1***	***1.2±0.1***	

The C/V ratio correlates well with conditions. The ratio is increasing with time in an *n*-butane/He atmosphere, after cooling down and after staying in air between the experiments and decreasing after the heating to 400°C. C/V values for the sample-2 in the points e'_{bulk} and e''_{bulk} on Figure 4-19, which were discussed in the part 4.6, have the values of 0.13 and 0.16. Therefore, no decreasing of the carbon content was observed for these two measurements.

The O/V ratio shows small variations with conditions, which correlate well with variations in the C/V ratio. Therefore, these deviations can be related to a change of amount of adsorbates. The mean value of 4.6 for a surface O/V ratio compared with O/V of 3.9 for the greater information depth also indicates the presence of adsorbates. The last value is smaller than the values of 4.5 for $(VO)_2P_2O_7$ and 5.0 for $VOPO_4$. These phases are expected for the bulk according to the sample characterization (part 4.3). The disagreement in O/V ratios is probably, because of the presence of adsorbates on the surface of reference samples, which would cause an overestimation of sensitivity factors and as a consequence, an underestimation

of an O/V ratio for the sample-2. This fact nevertheless, should not have any influence on P/V and C/V ratios.

Changes in P/V ratios of the sample-1 and sample-2 are shown on Figure 4-27 and Figure 4-28.

Figure 4-27. Change of a phosphor-vanadium stoichiometric ratio of the sample-1.

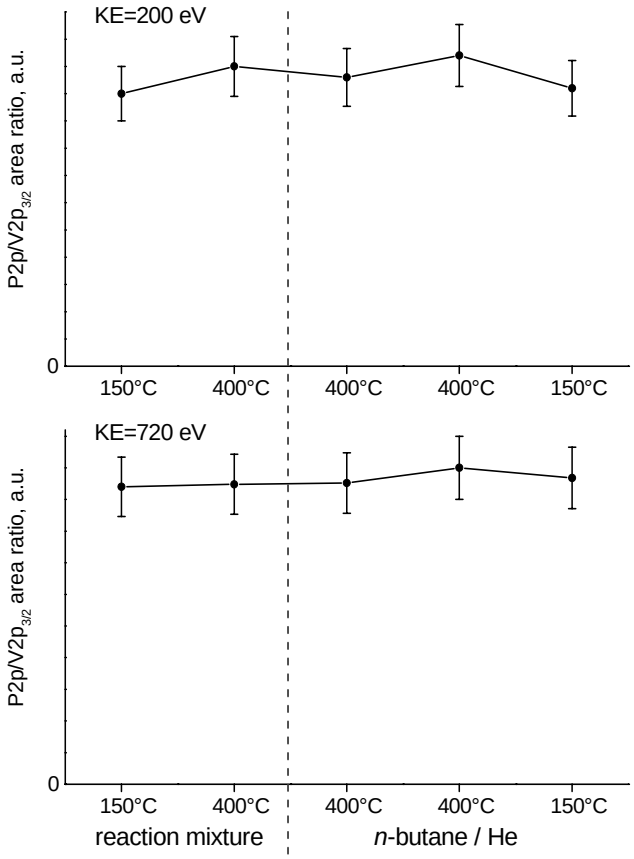

Figure 4-28. Change of a phosphor-vanadium stoichiometric ratio of the sample-2.

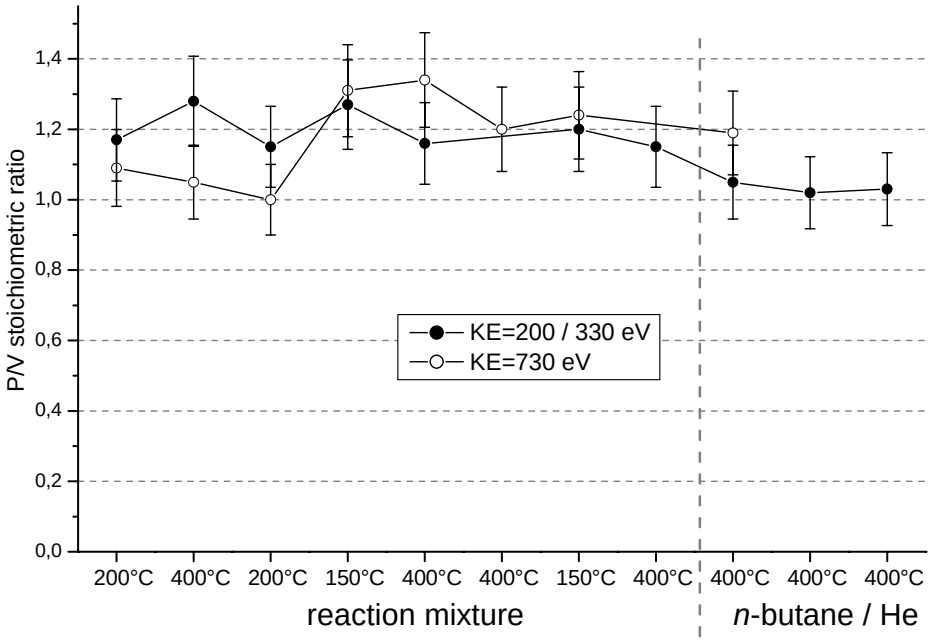

The points are randomly distributed within the error and do not show any correlation with conditions. No correlation can be also drawn between the P/V and O/V or C/V ratios in Table 4-6 and Table 4-7. The mean value of P/V ratio for the sample-2 is 1.1 for the surface and 1.2 for the bulk, which can be considered as the same within the experimental error. No strong conclusions can be drawn about enrichment or lack of phosphor on the surface as compared with the formal stoichiometric value of 1.05 because of the big uncertainty of the experimental sensitivity factors (Table 4-4). But it is obvious, that no great enrichment and gradient in the phosphor content was found near the surface in contrast to literature ([86], [88], [96] and others).

4.9 Discussion of the experimental results

Experimental data presented in this work are the result of the first XPS investigation of VPO catalysts under reaction conditions. Two investigated catalysts were found to be active towards MA under the low-pressure (2 mbar) reaction conditions. The ratio of the intrinsic activity of the sample-2 under the low-pressure conditions to that of the sample-1 was found to be (1.2±0.3). Therefore, the catalysts have nearly the same intrinsic activity and consequently, the same order of magnitude of a number of active species per surface area unity. Tracing of similarities and differences in the experimental data for these two catalysts would allow to move closer to clearing up the mystery of the nature of the active species responsible for the formation of MA on the VPO surface. The samples demonstrated a significantly different spectral behaviour during heating to the reaction temperature from a low temperature at which practically no MA was produced. The sample-2 showed no changes in vanadium oxidation state, while for the sample-1 changes in distribution of oxidation state with depth were observed. At the reaction conditions the surfaces of both catalysts were estimated to have the same value of a vanadium oxidation state, but a different gradient of oxidation state. A distribution of oxidation state with depth for the sample-2 was homogeneous, while the sample-1 demonstrated an increase with depth of the V^{5+} component in the $V2p_{3/2}$ peak. The thickness of the layer where the changes of oxidation state take place was estimated to be (3.5 ± 2.0) nm. One should note that the layer which directly participates the catalytic cycle should obviously be thinner as it follows from general considerations and from the literature data [78]. The existence of a surface layer of a composition which is different from the bulk composition was already more than ones suggested in literature [61, 76, 79, 80]. Our spectroscopic data are direct experimental proof of this fact. Therefore, one can conclude that deeper layers are a substrate for the active layer and their structure does not necessarily match the structure of the active layer. This easily explains the disagreements in the theories based on the not surface sensitive techniques discussed in the literature review part. The oxidation state of surface vanadium atoms found in this work is well consistent with the 4+ vanadium oxidation state of vanadyl pyrophosphate, which is usually found in the long-time operating catalyst. It is reasonable to assume that the diffusion process will equalize oxygen concentration over depth and thus, will equalize vanadium oxidation state. Nevertheless, the experimental error does not allow us to exclude the presence of some amount of V^{5+} or V^{3+} on the surface. Moreover, it is reasonable to assume the presence of such V atoms taking into account the polycrystalline nature of the catalyst, which should

contain various kinds of surface and bulk defects. Therefore, the results should be interpreted as most V atoms on the catalytically active surface have the 4+ oxidation state, but one cannot conclude from the data anything about a role in the catalytic process of a minor amount of V atoms in other oxidation states. Although the estimated oxidation state of the active material matches the oxidation state of vanadyl pyrophosphate crystalline phase, this data cannot be viewed as a confirmation of the fact that the active phase is vanadyl pyrophosphate. On the contrary, one can suggest that the vanadyl pyrophosphate structure is not the structure of the active surface. Literature data for reduction of VPO in H_2 and *n*-butane show formation of the $(VO)_2P_2O_7$ bulk phase and no V^{3+}-phase formation was reported [114, 115]. This means that the vanadium pyrophosphate phase has a high stability towards reducing conditions, while our investigation shows fast reduction of the active layer in *n*-butane atmosphere for both catalysts. Moreover, numerous *in situ* and *ex situ* studies revealed $(VO)_2P_2O_7$ as the main bulk phase of a well-equilibrated VPO catalyst, which means that the vanadium pyrophosphate phase is stable towards changing from reaction conditions to room temperature. At the same time, *in situ* XAS data [79, 81, 82] clearly show that the electronic structure of the VPO surface varies dynamically with conditions. The same observations would suggest none of the well-ordered crystalline structures as the active phase. Furthermore, several experimental studies reveal amorphous nature of the active surface [79-80]. The permanence within the experimental error of a P/V ratio during our experiments allow us to suggest rather the phosphate nature of the VPO active layer, but not a two-dimensional vanadium oxide, which was proposed recently [79]. The main role of phosphor in the operation of the catalyst is believed to be the setting of the correct relative position of vanadium active centers because the reaction of *n*-butane oxidation to MA was shown to take place also on supported vanadium oxides without presence of phosphor [116]. One can assume two factors. Firstly, it is insulation of oxygen domains, known as site insulation [89]. Secondly, phosphor could set a distance between two neighbor vanadium atoms so, that it fits the size of the *n*-butane molecule and consequently, the molecule can be easier accommodated [93].

As it was shown in this work, the composition of the surface layer can be different from the bulk that without a significant difference in the catalytic performance compared to the performance of a homogeneous VPO material. This fact clearly points to the development of supported vanadium oxides as a way of further improvement of a catalyst for the steady-state catalytic process. Several groups are involved in investigation of supported VPO [61, 62, 63]. Although a catalytic performance of produced samples is still far away from a bulk commercial catalyst, this field of activity looks very promising first of all, because of the

principal possibility to employ a cheap support material instead of complicated prepared bulk VPO and because of expected significant decrease of the catalyst activation period. Additionally, study of alumina supported vanadium oxides [116] shows a principal possibility to produce maleic anhydride from *n*-butane without use of phosphates, which would be another option for developing an improved catalyst for this reaction.

Another type of VPO catalyst is the catalyst for the unsteady-state DuPont process, i.e. the recirculating-solids process. A catalyst employed in this process should satisfy additional requirements comparing a catalyst for the steady-state process [117]. The material should readily supply bulk oxygen to the surface to make possible long-time catalyst operation under reducing conditions. Moreover, the material should be easily reoxidizable in the regeneration part of the operating cycle, which also implies good oxygen exchange between the gas phase, the surface and the bulk. *In situ* XPS is the unique technique, which provides a possibility to perform direct studies of lattice oxygen exchange in a near-surface region. Such studies were performed on bulk vanadium oxides [118] and can be readily performed on supported vanadium oxides [116]. The studies in the present work were performed in the reducing *n*-butane/He atmosphere. Change with time of a vanadium oxidation state of the samples correlates well with change of the MA yield. The sample having a better homogeneity with depth showed slower changes in oxidation state and in MA yield compared with the other sample. This implies better interaction of the active surface layer with the bulk in the sense of oxygen exchange, which immediately leads us to the conclusion about better suitability of a material of this catalyst towards condition changes in the unsteady-state process. These results show the power of *in situ* XPS method for the investigation of interaction phenomena of the active layer and a substrate, which would be extremely important for designing of supported catalysts for unsteady-state catalytic processes.

5 Conclusions and outlook

An experimental setup for *in situ* XPS investigations of the catalyst's surface was constructed. Physical principles of the system design were described in detail in part 3. *In situ* XPS technique was applied to a VPO catalyst, which is an important industrial catalyst for maleic anhydride production from *n*-butane. The results of the investigation were published in [119].

Two VPO catalysts with similar intrinsic catalytic activities towards maleic anhydride were investigated. In the reaction mixture one catalyst showed a high homogeneity of vanadium oxidation state with depth and another catalyst had a significant gradient of vanadium oxidation state. At the reaction conditions (2 mbar, reaction mixture, 400°C) both catalysts had the same surface oxidation state of (4.0±0.1), while the bulk oxidation state differed significantly. The experimental results suggest that the catalytically active species of a VPO catalyst are located in the topmost layer of thickness less than (3.5 ± 2.0) nm. The structure of this layer does not necessarily match the bulk structure and the bulk material is acting as a substrate only. The finding indicates that a bulk vanadium oxidation state in general, should not correlate with catalytic properties. The concept of an active layer with structure different from that of the bulk can play the central role in the strategy of improvement of a VPO catalyst. While the modern preparation methods are designed to get the $(VO)_2P_2O_7$ bulk phase, optimization of formation of the active surface layer could be more important. In this respect, development of a supported vanadium oxide catalyst looks very promising as a way to improve the catalyst and reduce its prices.

A P/V ratio, which is often referred as one of the main factors influencing the catalytic performance of the catalyst was not found to have any systematic changes during change of conditions. Scattering of the data points was within the experimental error. An absolute value of P/V ratio was calculated using experimental correction coefficients to theoretical sensitivity factors. The coefficients were estimated using XPS data of some solid reference compounds. An average P/V ratio of the VPO sample was found to be close to unity and did not change with depth. The uncertainty in the sensitivity factors does not allow formation of strong conclusions about the phosphor enrichment or depletion on the surface. More precise measurements can be done using gas-phase reference compounds, as was discussed in part 4.8.

The process of supplying the active layer with oxygen from the bulk under reducing conditions was investigated by leaving the sample in *n*-butane/He atmosphere in absence of

gas phase oxygen. Changes in the $V2p_{3/2}$ XPS peak correlate well with the decreasing MA yield. The sample which had a better homogeneity of vanadium oxidation state with depth showed slower changes in oxidation state and MA yield compared with the other sample. This means better supply of the catalytically active layer with bulk oxygen for this sample. This finding can be important for the catalyst design for the DuPont process, where a VPO catalyst operates under reducing conditions. The results show also the power of *in situ* XPS method for investigation of the phenomena of lattice oxygen exchange, which is important for design of catalysts for unsteady-state catalytic processes.

An accuracy of the XPS method could be significantly improved by obtaining additional theoretical knowledge about the photoelectron spectral-line shapes for material with various chemical composition and structure and about the photoionisation cross-sections. Nowadays one feels that there is a lack of such data in literature, but it is believed to be possible to obtain it in the near future.

The results of this work together with other publications ([33], [34]) demonstrates suitability and importance of the *in situ* XPS technique for characterization of the active surface of a solid-state catalyst including a real industrial catalyst.

References

[1] "Catalysis from A to Z. A concise encyclopedia.", ed. B. Cornils, W.A. Herrmann, R. Schlögl, C.-H. Wong, 1999, WILEY-VCH

[2] "In-situ spectroscopy of catalysts", ed. B.M. Weckhuysen, 2004, American Scientific Publishers

[3] M.P. Seah, Surf. Interface Anal. 9 (1986) 85-98

[4] E.D. Boyes, P.L. Gai, Ultramicroscopy 67 (1997) 219-232

[5] P.L. Gai, K. Kourtakis, Science 267 (1995) 661-663

[6] G.D. Danilatos, Advances in Electronics and Electron Physics 71 (1988) 109-250

[7] G.A. Somorjai, K.S. Hwang, J.S. Parker, Topics in Catalysis 26 (2003) 87-99

[8] J.R. Jenkin, R.C.G. Leckey, J. Liesegang, JESRP 12 (1977) 1-35

[9] H. Hertz, "On an effect of ultraviolet light upon electric discharge", Sitzungsber. d. Berl. Akad. d. Wiss. (1877)

[10] P.D. Innes, Proc. R. Soc. A 79 (1907) 442

[11] C. Nordling, E. Sokolowski, K. Siegbahn, Physical Review 105 (1957) 1676-1677

[12] E. Sokolowski, C. Nordling, K. Siegbahn, Physical Review, 110 (1958) 776-776

[13] A. Fahlman, K. Hamrin, J. Hedman, R. Nordberg, C. Nordling, K. Siegbahn, Nature 210 (1966) 4-8

[14] S. Hagstrom, C. Nordling, K. Siegbahn, Phys Lett 9 (1964) 235-236

[15] K. Siegbahn, Philosophical Transactions of the Royal Society of London Series A-Mathematical and Physical Sciences 268 (1970) 33

[16] "Practical surface analysis", ed. D. Briggs, M.P. Seah, vol.1, 1990, John Wiley & Sons Ltd.

[17] S. Hüfner, "Photoelectron spectroscopy: principles and applications", 2nd ed., 1996, Springer-Verlag

[18] K. Siegbahn, C. Nordling, G. Johansson, J. Hedman, P.F. Heden, K. Hamrin, U. Gelius, T. Bergmark, L.O. Werme, R. Manne, Y. Baer, "ESCA applied to free molecules", 1969, North-Holland Publishing Company

[19] D.A. Shirley, Phys. Rev. B 5 (1972) 4709-4724

[20] S. Tougard, B. Jørgensen, Surf.Sci. 143 (1984) 482-494

[21] S. Tougaard, J. Vac. Sci. Tech. A 8 (1990) 2197-2203

[22] Ed. J. Chastain, "Handbook of X-ray photoelectron spectroscopy", 1992, Perkin-Elmer Corporation

[23] J. Yeh., I. Lindau, At. Dat. Nucl. Dat. Tabl. 32 (1985) 1-155

[24] D.A. Verner, D.G. Yakovlev, Astr. Astroph. Suppl. Ser. 109 (1995) 125

[25] G.W. Coulston, E.A. Thompson, N. Herron, Journal of Catalysis 163 (1996) 122-129

[26] H. Siegbahn, K. Siegbahn, JESRP 2 (1973), 319-325

[27] H. Fellner-Feldegg, H. Siegbahn, L. Asplund, P. Kelfve, K. Siegbahn, JESRP 7 (1975) 421-428

[28] H. Siegbahn, S. Svensson, M. Lundholm, JESRP 24 (1981) 205-213

[29] R. Joyner, M. Roberts, Surf. Sci. 87 (1979), 501-509

[30] H.J Ruppender, M. Grunze, C.W. Kong, M. Wilmers, Surf. Interf. Anal. 15 (1990), 245-253

[31] D.F. Ogletree, talk at 8th international conference on electronic spectroscopy and structure, 08-12.08.2000, Clark Kerr Campus, University of California, Berkeley, California, USA

H. Bluhm, D.F. Ogletree, C.H.A. Huan, Ch. Fadley, Z. Hussain, M. Salmeron, posters at the same conference

[32] D.F. Ogletree, H. Bluhm, G. Lebedev, C.S. Fadley, Z. Hussain, M. Salemon, Rev. Sci. Instrum. 73 (2002) 3872-3877

[33] H. Bluhm, M. Hävecker, A. Knop-Gericke, E. Kleimenov, R. Schlögl, D. Teschner, V.I. Bukhtiyarov, D.F. Ogletree, M. Salmeron, J. Phys. Chem. B 108 (2004) 14340-14347

[34] D. Teschner, A. Pestryakov, E. Kleimenov, M. Hävecker, H. Bluhm, H. Sauer, A. Knop-Gericke, R. Schlögl, J. of Catalysis 230 (2005) 186-194 and 195-203

[35] H. Bluhm, D.F. Ogletree, C.S. Fadley, Z. Hussain, N. Salmeron, J. Phys.-Cond. Matter. 14 (2002) L227-L233

[36] M.A. Kelly, M.L. Shek, P. Pianetta, T.M. Gür, M.R. Beasley, J. Vac. Sci. Technol. A 19 (2001) 2127-2133

[37] The online service http://www-cxro.lbl.gov/ for the data calculation is provided by Center for X-Ray Optics (CXRO) of Lawrence Berkley National Laboratory on base of: B.L. Henke, E.M. Gullikson, J.C. Davis, Atomic Data and Nuclear Data Tables **54** (1993) 181-342

[38] K.R. Hoffman, M.S. Dababneh, Y.-F. Hsieh, W.E. Kauppila, V. Pol, J.H. Smart, T.S. Stein, Phys Rev. A 25 (1982) 1393-1403

[39] J.D. Anderson, "Modern compressible flow: with historical perspective", 3d edition, 2003, McGraw-Hill, New York

[40] D. Miller, in "Atomic and Molecular Beam Methods", ed. G. Scoles, 1988, Oxford University Press, New York

[41] Prisma QMS 200 M

[42] PTRMS instrument produced by IONICON Analytic GmbH, Innsbruck, Austria

[43] J. Picht, Ann. Phys, Lpz. 15 (1932) 926-964

[44] D.W.O. Heddle, "Electrostatic lens systems", 1991, IOP publishing Ltd.

[45] SIMION version 7.0. Author D.A. Dahl, Lockheed Idaho Technologies Company

[46] Phoibos 150 hemispherical analyzer, manufactured by Specs GmbH, Berlin

[47] M. Knoll, F. Ollendorff, R. Rompe, "Gasentladungstabellen", Springer-Verlag, 1935, Berlin, p. 84

[48] V.A. Lisovskiy, S.D. Yakovin, V.D. Yegorenkov, J. Phys. D: Appl. Phys. 33 (2000) 2722–2730, Figure 1

[49] J.S. Mirza, C.W. Smith, J.H. Calderwood, J. Phys. D: Appl. Phys. 4 (1971) 1126-1133

[50] S. Tougaard, A. Ignatiev, Surface Science 129 (1983) 355-365

[51] S. Tougaard, Surface Science 162 (1985) 875-885

[52] S. Tougaard, Surface Science 172 (1986) L503-L506

[53] S. Tougaard, J. Vac. Sci. Technol. A 5 (4) (1987) 1275-1278

[54] A.O. Nier, "Mass Spectroscopy" in Encyclopedia of Physics, ed. R.G. Lerner, G.L. Triggs, 2nd edition, 1991, VHC Publishers

[55] W. Lindinger, A. Hansel, A. Jordan, Chem. Soc. Rev. 27 (1998) 347-354

[56] R. Winckler, Ann. 4 (1832) 230

[57] J. Pelouze, Ann. 11 (1834) 263

[58] J.R. Skeen, Chem. Eng. News 26 (1948) 3684

[59] R.I. Bergman, N.W. Frisch, US Patent 3,293,268 (1966)

[60] T.R. Felthouse, J.C. Burnett, B. Horrell, M.J. Mummey, Y.-J. Kuo, "Maleic anhydride, maleic acid, and fumaric acid.", Kirk-Othmer encyclopedia of chemical technology, John Wiley and Sons, posted online 18.10.2001

[61] M. Ruitenbeek, A.J. van Dillen, A. Barbon, E.E. van Faassen, D.C. Koningsberger, J.W. Geus, Cat. Letters 55 (1998) 133-139

[62] R.A. Overbeek, "New aspects of the selective oxidation of n-butane to maleic anhydride: The development of a novel catalyst", Thesis, Utrecht University, 1994

[63] M.J. Ledoux, C. Crouzet, C. Pham-Huu, V. Turines, K. Kourtakis, P.L. Mills, J.J. Lerou, J. of Catalysis 203 (2001) 495-508

[64] J.A. Lopez-Sanchez, L. Griesel, J. Bartley, R. Wells, A. Liskowski, D. Su, R. Shlögl, J.-C. Volta, G. Hutchings, PCCP 5 (2003) 3525-3533

[65] "Vanadyl pyrophosphate catalysts", ed. G. Centi, Catalysis Today 16, n.1 (1993)

[66] J.-C. Volta, Chemistry 3 (2000) 717-723

[67] A. Delimitis, "Electron microscopy studies of doped vanadium phosphorus oxide catalysts", PhD thesis, University of Liverpool, 2002

[68] E. Borders, Catal. Today 1 (1987) 499-526

[69] E. Borders, Catal. Today 3 (1988) 163-174

[70] T. Shimoda, T. Okuhara, M. Misono, Bull. Chem. Soc. Jpn., 58 (1985) 2163-2171

[71] V.V. Guliants, J.B. Benziger, S. Sundaresan, I.E. Wachs, J.-M. Jehng, J.E. Roberts, Catalysis Today 28 (1996) 275-295

[72] V.V. Guliants, S.A. Holmes, J.B. Benziger, P. Heaney, D. Yates, I.E. Wachs, J.Mol.Cat. A 172 (2001) 265-276

[73] J.C. Volta, K. Bere, Y.J. Zhang, R. Oliver, ACS Symposium Series 523 (1993) 217-230

[74] J.-C. Volta, Catalysis Today 32 (1996) 29-36

[75] K. Aït-Lachgar, M Abon, J.C. Volta, Journal of Catalysis 171 (1997) 383-390

[76] G.J. Hutchings, C.J. Kiely, M.T. Sananes-Schulz, A. Burrows, J.C. Volta, Cat. Today 40 (1998) 273-286

[77] G.W. Coulston, S.R. Bare, H. Kung, K. Birkeland, G.K. Bethke, R. Harlow, N. Herron, P.L. Lee, Science 275 (1997) 191-193

[78] M. Abon, K.E. Bere, P. Delichere, Catalysis Today 33 (1997) 15-23

[79] H. Bluhm, M. Hävecker, E. Kleimenov, A. Knop-Gericke, A. Liskowski, R. Schlögl, D. S. Su, Topics in Catalysis 23 (2003) 99-107

[80] G.J. Hutchings, J.A. Lopez-Sanchez, J.K. Bartley, J.M. Webster, A. Burrows, C.J. Kiely, A.F. Carley, C. Rhodes, M. Havecker, A. Knop-Gericke, R.W. Mayer, R. Schlogl, J.C. Volta, M. Poliakoff, J.Catal. 208 (2002) 197-210

[81] M. Hävecker, R.W. Mayer, A. Knop-Gericke, H. Bluhm, E. Kleimenov, A. Liskowski, D. Su, R. Follath, F.G. Requejo, D.F. Ogletree, M. Salemon, J.A. Lopez-Sanchez, J.K. Bartley, G.J. Hutchings, R. Schlögl, J. Phys. Chem. B 107 (2003) 4587-4596

[82] M Hävecker, A. Knop-Gericke, H. Bluhm, E. Kleimenov, R.W. Mayer, M. Fait, R. Schlögl, Appl. Surf. Sci. 230 (2004) 272-282

[83] T. Okuhara, M. Misono, Catalysis Today 16 (1993) 61-67

[84] F. Garbassi, J.C.J. Bart, R. Tassinari, G. Vlaic, P. Lagarde, Journal of Catalysis 98 (1986) 317-325

[85] B.K. Hodnett, P. Permanne, B. Delmon, Applied Catalysis 6 (1983) 231-244

[86] J. Haas, C. Plog, W. Maunz, Proc. 9th Int. Congr. Cat. v.4 (1988) 1632-1639

[87] M. Abon, K.E. Bere, A. Tuel, P. Delichere, Journal of Catalysis 156 (1995) 28-36

[88] H. Batis, H. Batis, A. Ghorbel, J. Vedrine, J.C. Volta, Journal of Catalysis 128 (1991) 248-263

[89] P.A. Agaskar, L. De Caul, R.K. Grasselli, Catal. Letters 23 (1994) 339-351

[90] R.K. Grasselli, Topics in Catalysis 15 (2001) 93-101

[91] J.R. Ebner, M.R. Thompson, Catalysis Today 16 (1993) 51-60

[92] G. Centi, Catalysis Today 16 (1993) 5-26

[93] V. Zazhigalov, private communications

[94] P. Delichere, K.E. Bere, M. Abon, Applied Catalysis A: General (1998) 172, 295-309

[95] J. Scofield, JESRP 8 (1976) 129-137

[96] W.P.A. Jansen, M. Ruitenbeek, A.W.D. v.d. Gon, J.W. Geus, H.H. Brongersma, J. Catal. 196 (2000) 379-387

[97] F. Senf, F. Eggenstein, U. Flechsig, R. Follath, S. Hartlaub, H. Lammert, T. Noll, J.S. Schmidt, G. Reichardt, O. Schwarzkopf, M. Weiss, T. Zeschke and W. Gudat, Nucl. Instr. Meth. A 467-468 (2001) 474-478

[98] http://www.bessy.de/

[99] S. Geupel, K. Pilz, S. van Smaalen, Acta Crystallographica C 58 (2002) I9

[100] A. Thompson, D. Vaughan et al., "X-ray data booklet", Center for X-ray Optics and Advanced Light Source, Lawrence Berkeley National Laboratory, second edition, 2001

[101] L.M. Cornaglia, E.A. Lombardo, Applied Catalysis A 127 (1995) 125-138

[102] M. Havecker, A. Knop-Gericke, R.W. Mayer, M. Fait, H. Bluhm, R. Schlogl, J. Electr. Sp. Rel. Ph. 125 (2002) 79–87

[103] M. Witko, R. Tokarz, J. Haber, K. Hermann, J. Mol. Catal. A 166 (2001) 59-72

[104] D. Briggs, "Application of XPS in Polymer Technology", in "Practical surface analysis", ed. D. Briggs, M.P. Seah, vol.1, 1990, John Wiley & Sons Ltd

[105] G.A. Sawatzky, D. Post, Phys. Rev. B 20 (1979) 1546-1555

[106] M. Demeter, M. Neumann, W. Reichelt, Surf. Sci. 454-456 (2000) 41-44

[107] J. Mendialdua, R. Casanova, Y. Barbaux, J. Electr. Sp. Rel. Ph. 71 (1995) 249-261

[108] M. Heber, W. Grünert, J. Phys. Chem. B. 104 (2000) 5288-5297

[109] W. Yuqing, P.M.A. Sherwood, Surf. Sci. Spectra 9 (2002) 159-165

[110] L. Calliari, N. Laidani, G. Speranza, Surf. Interface Anal. 26 (1998) 565-568

[111] R. Zimmermann, R. Claessen, F. Reinert, P. Steiner, S. Huefner, J. Phys.: Cond. Matter 10 (1998) 5697-5716

[112] a) A. Proctor, P.M.A. Sherwood, Anal. Chem.54 (1982) 13-19

b) P.M.A. Sherwood, "Data analysis in X-ray Photoelectron Spectroscopy" in "Practical surface analysis", ed. D. Briggs, M.P. Seah, 1983, p. 445-475

[113] A. Carley, P. Chalker, J. Riviere, M. Roberts, J. Chem. SOC, Farad. Trans I 83 (1987) 351-370

[114] T.P. Moser, G.L. Schrader, Journal of Catalysis 104 (1987) 99-108

[115] G. Koyano, T. Okuhara, M. Misono, J. Am. Chem. Soc. 120 (1998) 767-774

[116] D. Teschner, A. Pestryakov, E. Kleimenov, M. Hävecker, H. Bluhm, A. Knop-Gericke, R. Schlögl, "In-situ XPS and XAS investigation on the redox and catalytic properties of VOx/Al_2O_3", preparing for publication

[117] X.-F. Huang, C.-Y. Li, B.-H. Chen, P. L. Silveston, AIChE Journal 48 (2002) 846-855

[118] E. Kleimenov, H. Bluhm, M. Hävecker, A. Knop-Gericke, A. Pestryakov, D. Teschner, R. Schlögl, "In Situ XPS and NEXAFS Investigations of Lattice Oxygen Exchange in V_2O_5 by Reduction in Low-Pressure Oxygen Atmosphere", 4th International Symposium on Chemistry and Biological Chemistry of Vanadium, 03-05.09.2004, Szeged, Hungary

[119] E. Kleimenov, H. Bluhm, M. Hävecker, A. Knop-Gericke, A. Pestryakov, D. Teschner, J. A. Lopez-Sanchez, J. K. Bartley, G.J. Hutchings, R. Schlögl, Surface Science 575 (2005) 181-188

Acknowledgement

I would like to thank all people who contributed this work.

I am saying "thank you" to:

- my colleagues from FHI for interest to my work and fruitful discussions
- my second scientific adviser Prof. Dr. Mario Dähne for interest to my work and its reviewing
- BESSY staff for the full and continuous technical support of the experiments
- my former teachers and colleagues. Especially to my advisers M.Sc. Alexander B. Fedotov, Dr. Nikolaj A. Krjukov, Prof. Dr. Valerij S. Ivanov, Dr. Sergej V. Potapov
- my family and girlfriend Anja for care and patience
- the members of Lawrence Berkeley Laboratory Dr. D. Frank Ogletree, Dr. Eleonore L. Hebenstreit and Dr. Miquel Salmerond for collaboration in the theoretical design of the XPS system
- SPECS company (Berlin, Germany) and personally Dr. Sven Mächl for collaboration in modifying the spectrometer
- M.Sc. Andrzej Liskowski for production the $VOPO_4$ reference compounds
- Dipl. Ing. Ute Wild for XPS data of some vanadium compounds measured at ESCA spectrometer
- the members of Cardiff University Dr. Jose A. Lopez-Sanchez, Dr. Jonathan K. Bartley and Prof. Dr. Graham J. Hutchings for the VPO samples
- Dr. Elaine Vass for the language correction
- Dr. Detre Teschner and Prof. Dr. Alexej Pestryakov for participation the experimental work and discussions of the experimental results
- Dipl. Ing. Klaus Ihmann for the engineering design of our XPS system and for care about a part production process
- my senior colleagues Dr. Axel Knop-Gericke, Dr. Michael Hävecker and Dr. Hendrik Bluhm, from every of those I have got the overall support at all stages of my PhD work including work with literature, gaining skills of working with the equipment, planning the experiments, experimental work, data analysis, publishing the results, presenting them at conferences and writing the PhD thesis
- my scientific adviser Prof. Dr. Robert Schlögl for statement of the scientific problem, for providing the financial support of the PhD work and for scientific ideas thanks to those this work was fulfilled